การสังเคราะห์ฟิสเชอร์-ทรอปช์บนโคบอลต์รองรับด้วยเส้นใยซิลิกาโดยอิเล็กโทรสปินนิง

นางสาวกัญฐณา คล้ายแก้ว

วิทยานิพนธ์นี้เป็นส่วนหนึ่งของการศึกษาตามหลักสูตรปริญญาวิทยาศาสตรดุษฎีบัณฑิต
สาขาวิชาเคมีเทคนิค ภาควิชาเคมีเทคนิค
คณะวิทยาศาสตร์ จุฬาลงกรณ์มหาวิทยาลัย
ปีการศึกษา 2557

FISCHER-

TROPSCH SYNTHESIS OVER COBALT SUPPORTED ON ELECTROSPUN SILICA FIBERS

Miss Kanthana Klaigaew

A Dissertation Submitted in Partial Fulfillment of the Requirements

for the Degree of Doctor of Philosophy Program in Chemical Technology

Department of Chemical Technology

Faculty of Science

Chulalongkorn University

Academic Year 2014

Thesis Title	FISCHER-TROPSCH SYNTHESIS OVER COBALT SUPPORTED ON ELECTROSPUN SILICA FIBERS
By	Miss Kanthana Klaigaew
Field of Study	Chemical Technology
Thesis Advisor	Assistant Professor Prasert Reubroycharoen, D.Eng.
Thesis Co-Advisor	Professor Noritatsu Tsubaki, Ph.D.

Accepted by the Faculty of Science, Chulalongkorn University in Partial Fulfillment of the Requirements for the Doctoral Degree

.....Dean of the Faculty of Science
(Professor Supot Hannongbua, Dr.rer.nat.)

THESIS COMMITTEE

.....Chairman
(Associate Professor Kejvalee Pruksathorn, Dr.de L'INPT)

.....Thesis Advisor
(Assistant Professor Prasert Reubroycharoen, D.Eng.)

.....Thesis Co-Advisor
(Professor Noritatsu Tsubaki, Ph.D.)

.....Examiner
(Assistant Professor Chawalit Ngamcharussrivichai, Ph.D.)

.....Examiner
(Assistant Professor Napida Hinchiranan, Ph.D.)

.....External Examiner
(Assistant Professor Chanatip Samart, D.Eng.)

กัญฐณา คล้ายแก้ว : การสังเคราะห์ฟิสเชอร์-ทรอปช์บนโคบอลต์รองรับด้วยเส้นใยซิลิกาโดยอิเล็กโทรสปินนิง (FISCHER-TROPSCH SYNTHESIS OVER COBALT SUPPORTED ON ELECTROSPUN SILICA FIBERS) อ.ที่ปรึกษาวิทยานิพนธ์หลัก: ผศ. ดร. ประเสริฐ เรียบร้อยเจริญ, อ.ที่ปรึกษาวิทยานิพนธ์ร่วม: ศ. ดร. โนริทัทซึ ซึบากิ, 108 หน้า.

งานวิจัยนี้ศึกษาการเตรียมเส้นใยซิลิกาด้วยวิธีอิเล็กโทรสปินนิง และใช้เป็นตัวรองรับโคบอลต์ เพื่อใช้ในการเร่งปฏิกิริยาการสังเคราะห์ฟิสเชอร์-ทรอปช์ โดยภาวะที่เหมาะสมในการเตรียมเส้นใยซิลิกา คือ ขนาดเข็มฉีดเท่ากับ 0.25 มิลลิเมตร ที่ระยะห่างระหว่างเข็มกับวัสดุรองรับเส้นใยเท่ากับ 15 เซนติเมตร และความต่างศักย์ไฟฟ้าเท่ากับ 15 กิโลโวลต์ ซึ่งเส้นใยที่ได้มีขนาดเส้นผ่านศูนย์กลางเฉลี่ยเท่ากับ 0.83ไมโครเมตร จากนั้นนำเส้นใยซิลิกาที่เตรียมได้มาเคลือบด้วยซีโอไลต์ ZSM-5 โดยวิธีไฮโดรเทอร์มอล ที่อุณหภูมิ 170 องศาเซลเซียส เป็นเวลา 24 ชั่วโมง พบว่าการเคลือบเส้นใยซิลิกาด้วย ZSM-5 ช่วยเพิ่มพื้นที่ผิวให้กับตัวรองรับ เมื่อนำไปเคลือบด้วยโลหะโคบอลต์และใช้ในการเร่งปฏิกิริยาการสังเคราะห์ฟิสเชอร์-ทรอปช์ พบว่าให้ค่าร้อยละการเปลี่ยนคาร์บอนมอนนอกไซด์สูงมากกว่าร้อยละ 80 และให้ค่าการเลือกเกิดเป็นสารประกอบไฮโดรคาร์บอนที่มีจำนวนอะตอมคาร์บอนเท่ากัน 5-11 ที่สูง นอกจากนี้ยังได้ศึกษาวิธีการเคลือบโลหะโคบอลต์ลงบนเส้นใยซิลิกา ด้วยวิธีการต่างๆ ดังนี้ วิธีการเปียกชุ่ม (impregnation, IM), การดูดซับด้วยแรงทางไฟฟ้าสถิต (strong electrostatic adsorption, SEA), การตกตะกอน (deposition precipitation, DP) ด้วยโซเดียมไฮดรอกไซด์ (DPNa) หรือ แอมโมเนีย (DPNH) และวิธีการสังเคราะห์แบบไฮโดรเทอร์มอล (hydrothermal synthesis, HT) พบว่าวิธีการเคลือบโลหะโคบอลต์ลงบนเส้นใยซิลิกามีผลต่อประสิทธิภาพของตัวเร่งปฏิกิริยา โดยตัวเร่งปฏิกิริยาที่ให้ค่าร้อยละการเปลี่ยนคาร์บอนมอนนอกไซด์จากสูงไปต่ำ คือ SEA > DPNH = DPNa > IM >> HT ขนาดของโคบอลต์ที่เตรียมด้วยวิธีต่างๆ อยู่ในช่วง 4 ถึง 30 นาโนเมตร โดยตัวเร่งปฏิกิริยาที่เตรียมด้วยวิธีการดูดซับด้วยแรงทางไฟฟ้าสถิตให้ประสิทธิภาพในการเร่งปฏิกิริยาที่สูงที่สุด เนื่องจากอนุภาคโคบอลต์ที่มีขนาดเล็ก และมีการกระจายตัวที่ดี

ภาควิชา เคมีเทคนิค ลายมือชื่อนิสิต .....

สาขาวิชา เคมีเทคนิค ลายมือชื่อ อ.ที่ปรึกษาหลัก .....

ปีการศึกษา 2557 ลายมือชื่อ อ.ที่ปรึกษาร่วม .....

5273801023 : MAJOR CHEMICAL TECHNOLOGY
KEYWORDS: FISCHER-TROPSCH SYNTHESIS / ELECTROSPINNING / SILICA FIBERS / COBALT / ZSM-5

KANTHANA KLAIGAEW: FISCHER-TROPSCH SYNTHESIS OVER COBALT SUPPORTED ON ELECTROSPUN SILICA FIBERS. ADVISOR: ASST. PROF. PRASERT REUBROYCHAROEN, D.Eng., CO-ADVISOR: PROF. NORITATSU TSUBAKI, Ph.D., 108 pp.

This research aimed to study the preparation of electrospun silica fibers (SF) and using as catalyst support. SF were synthesized from TEOS by a facile combination of sol-gel and electrospinning methods and then used as supports for cobalt catalysts in the Fischer-Tropsch synthesis (FTS) reaction. The optimized condition for SF preparation was a 15 cm TCD and 15 kV applied voltage to produce continuous SF with a submicron diameter of 0.83 μm. Then, SF were modified by *in situ* hydrothermal synthesis of the zeolite ZSM-5 on the SF (ZSM-5/SF) at 170°C for 24 h. ZSM-5/SF support was used to prepare supported cobalt FTS catalysts. Their catalytic performance in the FTS was tested. The FTS using the ZSM-5 modified SF supported Co catalysts showed a high selectivity to C5–C11 hydrocarbons with a high CO conversion level. Moreover, different SF supported cobalt catalysts were prepared by impregnation (IM), strong electrostatic adsorption (SEA), deposition precipitation (DP) from either sodium hydroxide (DPNa) or ammonia solution (DPNH), and hydrothermal synthesis (HT). The preparation methods significantly affected the catalytic activity of the obtained catalysts, with their catalytic activity in the FTS reaction being ranked (highest to lowest) in the order of SEA > DPNH = DPNa > IM >> HT. The size of the Co_3O_4 particles in the cobalt supported on SF catalysts ranged from 4 nm to 30 nm of diameter. The excellent catalytic activity of the Co/SF-SEA catalyst could be attributed to the smaller size of the cobalt particles and their higher dispersion level.

Department:	Chemical Technology	Student's Signature .....
Field of Study:	Chemical Technology	Advisor's Signature .....
Academic Year:	2014	Co-Advisor's Signature .....

ACKNOWLEDGEMENTS

I would never have been able to finish my dissertation without the guidance of my committee members, help from friends, and support from my family.

I would like to express my deepest gratitude to my advisor, Asst. Prof. Prasert Reubroycharoen, for his excellent guidance, caring, patience, and guiding my research for the past several years. I would like to thank my co-advisor, Prof. Noritatsu Tsubaki, and Prof. Yoshiharu Yoneyama who let me experience the research of Fischer-Tropsch synthesis at Toyama University, patiently corrected my writing and financially supported my research. I would also like to thank Assoc. Prof. Kejvalee Pruksathorn, Asst. Prof. Chawalit Ngamcharussrivichai, Asst. Prof. Napida Hinchiranan and Asst. Prof. Chanatip Samart, who was willing to participate in my final defense committee at the last moment.

I would like to acknowledge the financial support of The Royal Golden Jubilee Ph.D. Program, the Thailand Research Fund, in collaboration with Petroleum Authority of Thailand (PTT) and Overseas Academic Presentation Scholarship for Graduate Students, Graduate School, Chulalongkorn University.

I would like to thank every laboratory worker of Asst. Prof. Prasert and Prof. Tsubaki for helping and teaching me how to use laboratory equipments. My research would not have been possible without their helps.

I would also like to thank my parents. They were always supporting me and encouraging me with their best wishes.

CONTENTS

Page

Page

Page

Page

LIST OF TABLES

LIST OF FIGURES

LIST OF ABBREVIATION

Co	cobalt
SiO_2	silicon dioxide
CO	carbon monoxide
mm	millimeter (s)
wt%	weight percent
kV	kilovoltage (s)
cm	centimeter (s)
^oC	degree Celsius
nm	nanometer
SEM	Scanning electron microscope
EDS	Energy dispersive spectroscopy
TEM	Transmission electron microscopy
XRD	X-ray Diffraction
TPR	Temperature-programmed reduction
FTS	Fischer-Tropsch synthesis
atm	atmosphere
mL	milliliter
min	minute (s)
g	gram (s)
et. al	and others
DC	direct current
$ohm^{-1}W^{-1}$	ratio of electric conductivity per ohm and watt
h	hour (s)
FESEM	Field Emission Scanning Electron Microscopy
^oF	degree Fahrenheit
mol	mole
TEOS	tetraethyl orthosilicate
TGA	thermogravimetric Analysis
P	pressure
MPa	megapascal
T	temperature
V	volume
cat	catalyst

GC	Gas Chromatograph
HCl	hydrochloric acid
TCD	tip to collector distance
He	helium
TCD	thermal conduct detector
PVP	polyvinylpyrrolidone
μm	micron
MW	molecular weight
EtOH	ethanol
cm^3	cubic centimete

CHAPTER I
INTRODUCTION

1.1 Statement of problem

The Fischer-Tropsch synthesis (FTS) reaction is an industrialized process for the production of hydrocarbon fuels and chemicals from syngas via polymerization reaction. A lot of products are generated by this process, such as paraffins, olefins, alcohols and aldehydes. The most suitable catalysts in the FTS reaction for a higher hydrocarbon production level have been found to be cobalt based catalysts [1-3], but the performance of catalysts is influenced by the procedure of catalyst preparation, such as the structure of support material, the method of deposition, the type of catalyst's promoter and the thermal treatment process [4, 5]. The catalysts reactivity in the FTS reaction is correlated to the number of Co^0 particles exposed to the syngas molecules, which in turn depends on the cobalt loading and dispersion levels and the reducibility of the initial cobalt species to Co^0. Hence, an ideal supported cobalt catalyst would have uniformly distributed cobalt species that undergo to complete reduction, forming Co^0 nanoparticles of 6~8 nm diameter [6]. Commonly used supports include silica (SiO_2), alumina (Al_2O_3), titanium dioxide (TiO_2) and zeolites [3]. The type and texture of the support play significant role in the dispersion, particle size, reducibility, and the activity for catalysts. A several researchers have been reported about the application of carbon as a support for cobalt catalyst. Tavasoli et al. [7] investigated the FTS reaction over cobalt catalysts supported on carbon nanotubes (CNT) and γ–Al_2O_3 with different loading of cobalt. The results showed that average Co_3O_4 crystallite size in Co/CNT catalyst was only 4.92 nm due to a higher surface area of CNT support. The catalysts enhanced the CO conversion, FTS and water-gas shift (WGS) reaction rates. Martínez et al. [8] reported results for cobalt supported on nanofibrous γ-Al_2O_3 catalysts. The catalyst that used an alumina nanofiber as catalyst support showed a slightly decrease in the cobalt-time-yield at the initial stages. They suggested that the enhancement of CO diffusion to the active metal was accelerated by the wide porous structure of the alumina nanofiber resulting in an increase activity of catalyst.

However, a porous catalyst working under FTS conditions has pore filling with liquid products and this introduce to limit diffusion of syngas and products which decrease catalyst performance. Inorganic nanofibers have very large surface area to

volume ratio and good mechanical properties. The preparations of inorganic nanostructure such as fibers, rods, and tubes have received great interest because of their potential applications such as sensors and catalysts. Inorganic nanofibers can be prepared by electrospinning technique with a several type of inorganic precursor. The inorganic materials that have been transformed to nanofiber morphology are titanium dioxide (TiO_2), silicon dioxide (SiO_2), zirconium dioxide (ZrO_2), aluminum oxide (Al_2O_3) and so on.

The nanofibrous catalyst displays the highest specific activity and productivity to diesel products. Silica, as a common support used for catalysts in the FTS reaction, presents a higher surface area, porosity and stability and a weaker metal-support interaction than aluminum [9]. Silica fibers (SF) have many advantages, such as resistance to acids or bases and a good stability at high temperatures in inert or reducing atmospheres, which allows the catalyst properties to be tailored for specific needs. However, the weak interaction between cobalt and silica in silica-supported catalysts favors the reduction of the cobalt precursor and promotes agglomeration of the supported cobalt particles that leads a reduced dispersion level of the supported cobalt and the number of active sites.

This work aims to investigate the effect of the SF support on the physicochemical properties of the obtained SF supported cobalt oxide catalyst. SF were synthesized by electrospinning and used as the support for cobalt catalysts. The effect of the SF-supported cobalt (Co/SF) catalyst preparation method on the physicochemical properties of the obtained SF-supported cobalt oxide (unreduced catalyst) was studied, and its catalytic performance following reduction was tested in the FTS reaction. Moreover, the modification of SF with ZSM-5 via an in situ hydrothermal synthesis on the SF was investigated. The zeolite crystals were made to grow onto the structured SF supports in the synthesis mixture. Then, the ZSM-5 modified SF were used as the support for the Co catalysts for the FTS reaction and the influence of supporting the ZSM-5 on the SF surface on its catalytic performance during the FTS reactions was studied.

1.2 Studies of the thesis

The research procedures were carried out as follows:

1. Literature review.
2. Study of Fischer-Tropsch synthesis apparatus in laboratory scale, and preparation of the chemicals and raw materials for the experiment.

3. Study of the preparation of silica fibers by electrospinning technique and characterization.
4. Study the effect of cobalt supported on silica fibers modified by ZSM-5 zeolite catalyst on the catalytic performance in the Fischer-Tropsch synthesis.
5. Study the effect of catalyst preparation methods on physical-chemical properties of catalyst and the catalytic performance in the Fischer-Tropsch synthesis.

1.3 Objectives

- To prepare silica fiber support by the electrospinning technique.
- To prepare Co supported on SF (Co/SF) catalyst by several methods.
- To prepare SF modified by ZSM-5 and use as the catalyst support
- To study the catalytic activity of Co/SF prepared by different methods and composite cobalt catalyst for FTS reaction.

CHAPTER II

THEORY AND LITERATURE REVIEWS

2.1 The Fischer-Tropsch Synthesis (FTS)

2.1.1 Introduction

The Fischer-Tropsch synthesis (FTS) is a reaction which converts synthesis gas or syngas, a mixture of CO and H_2, into hydrocarbon compounds [1, 3, 10]. This synthesis was firstly published by Han Fischer and Franz Tropsch. The FTS reaction generally includes the following equations [1],

$$nCO + (2n+1)H_2 \longrightarrow C_nH_{2n+2} + nH_2O \quad (2.1)$$

$$nCO + 2nH_2 \longrightarrow C_nH_{2n} + nH_2O \quad (2.2)$$

Both reactions are exothermic reaction ($\Delta H = -165–204$ kJ). Equation (2.1) and (2.2) relates to the production of paraffins and olefins, respectively. Moreover, organic oxygenates may be formed [Equation (2.3)] under FTS condition.

$$2nH_2 + nCO \longrightarrow C_nH_{2n+2}O + (n-1)H_2O \quad (2.3)$$

Alcoholic products can also be formed either as by-products or as main product depending on the catalytically active metal and the pressure. A whole range of products with different lengths of the carbon chain can be obtained. Names and compositions of fuels from crude oil refinery processes are listed in Table 1.

Table 1 Names and composition of fuel oils [10]

Name	Carbon number
Fuel gas	1-2
LPG	3-4
Gasoline	5-12
Naphtha	8-12
Kerosene	11-13
Diesel	13-17
Middle distillates	10-20
Soft wax	19-23
Medium wax	24-35
Hard wax	35+

The hydrocarbon products of FTS can be sulfur- and nitrogen-free high-quality fuels such as diesel fuels, which have been proven to be more environmentally benign than the petroleum-based fuels [1] and thus may easily meet the increasingly stringent environmental regulations (e.g., low residual sulfur content). Moreover, chemicals such as α-alkenes or C_2–C_4 lower alkenes may also be directly produced from syngas if a highly selective FTS catalyst can be developed. Therefore, FTS is a crucial step for the transformation of non-petroleum resources into super-clean fuels or valuable chemicals from syngas.

Moreover, the water–gas shift (WGS) reaction [Equation (2.4)] and the Boudouard reaction [Equation (2.5)], also occurs over most FTS catalysts. The WGS reaction describes the reaction of carbon monoxide with water, which is formed during the reaction [Equation (2.1) and (2.2)], to hydrogen and carbon dioxide [11].

$$CO + H_2O \longrightarrow CO_2 + H_2 \qquad (2.4)$$

$$2CO \longrightarrow CO_2 + C \qquad (2.5)$$

The Boudouard reaction [Equation (2.5)] is the reaction of two carbon monoxides to produce carbon dioxide and carbon [12]. This reaction can be observed on active metal site under high temperature. The carbon product of this reaction deposit on pore structure of catalyst and block the active sites resulting in the deactivation of catalyst.

2.1.2 Catalysts for Fischer-Tropsch synthesis

2.1.2.1 Supported metal oxide catalysts

The most common active metals in the hydrogenation of CO to hydrocarbons are Ni, Fe, Co and Ru [1, 3, 10]. Different transition metals will exhibit some differences in catalytic behavior. From these metals, ruthenium is the most active catalyst, but the high price of ruthenium limited its application on an industrial application. Nickel catalyst is not suitable for the FTS reaction because under practical conditions this catalyst's product contains mainly methane. Cobalt and iron catalysts are the first catalysts for syngas conversion and have been employed commercially for hydrocarbon synthesis. Cobalt catalysts are more expensive than iron catalysts, but they have demonstrated high activity, high selectivity to linear paraffins, high resistance toward deactivation, and low WGS activity. Iron catalysts are an active FTS catalyst and also for WGS reaction and is therefore ideal for converting syngas which has low H_2/CO ratio derived from coal. Iron catalysts usually produce more olefins.

Metal nanoparticles supported on oxide materials of heterogeneous catalysts which completely reduce at high temperature is influence by strong metal–support interactions (SMSI) [13, 14]. Therefore, the interaction of active metal and support is very important for catalytic activity of heterogeneous catalyst. If the metal–support interaction too weak, the agglomerated active metal can be obtained. On the other hand, if the metal–support interaction too strong, the metal oxides is hardly reduce to active phase. Moreover, catalyst support help the system to release heat from exothermic reaction and decrease temperature gradient in fixed bed reactors. The catalytic activity are effected by pore structure of the support because the pore structure has influence with the particle size of metal, the reducibility of catalyst and the diffusion of reactants or products [5, 15].

Supports are normally used for Co and Ru catalysts, which are more expensive than Fe catalysts. Oxide materials, particularly SiO_2, Al_2O_3, and TiO_2, are probably the most extensively investigated supports for Co catalysts [16-18]. The effects of these supports on catalytic properties of supported Co catalysts have been studied.

Silica-Supported Catalysts: The common support of the heterogeneous catalysts are silica because silica shows several advantageous properties, such as high chemical and thermal stability, high surface area, and high porosity [13, 19]. Furthermore, the silica supported cobalt catalyst shows high reducibility due to the weak interaction between silica support and cobalt metal. However, silica-supported catalysts display a low cobalt dispersion Thus, high cobalt dispersion have to design of silica-based FTS catalysts. The catalytic activity in FTS increased with the specific surface area of catalyst, and the selectivity for long chain hydrocarbons was found in the catalyst with support pore diameter larger than 4 nm [20]. The catalyst supported by silica with an average pore diameter of 10 nm was most active and selective for hydrocarbons [21]. CO conversion and C_{5+} selectivity increased at first and then decreased with increasing catalyst pore diameter. The catalysts with a pore size of 6-10 nm displayed higher Fischer-Tropsch activity and higher C_{5+} selectivity [5]

Alumina-Supported Catalysts: Al_2O_3 has been also used as supports for cobalt FTS catalysts. The interaction of cobalt and alumina support is very strong resulting in forming small cobalt crystallites. These small cobalt crystallites can be react and diffuse to alumina and then form nonstoichiometric cobalt aluminate spinels which cannot be completely reduce. Cobalt reducibility is one of the most important problems of alumina-supported cobalt FTS catalysts [3, 22]. The reducibility of cobalt supported on alumina catalyst can be enhance by the promotion with noble metals.

Titania-Supported Catalysts: TiO_2 is important support in heterogeneous catalysis due to the size and nature of the interaction of a metal nanoparticle with TiO_2 support [23]. The metal–support interactions of Co species and titania support are lower than that of alumina-supported cobalt catalysts but higher than that of alumina support [9, 18, 22-24]. The activity of Co/TiO_2 catalysts largely depended on the TiO_2 crystal phase. TiO_2 samples containing rutile phase were more suitable as the support TiO_2 material than those containing only anatase phase [18]. The catalytic activity of CO hydrogenation decreased in the order of Co/TiO_2 > Co/SiO_2 > Co/Al_2O_3. The catalytic activity was determined by the amount of metal loading and the dispersion of cobalt which can be improved by using the certain support [29]. Besides SiO_2, Al_2O_3, and TiO_2, other oxides materials have also been used as supports for FTS catalysts such as ZrO_2 [25] and $AlPO_4$ [26, 27].

2.1.2.2 Zeolite-supported catalysts

Zeolites have molecular sieving properties that do not allow the formation of products, intermediates, or transition states larger than the size of the cavities or channels of the zeolites [28]. The production of heavy hydrocarbon is limit by these properties and the light hydrocarbons are the major product over this catalyst. On the other hand, long-chain hydrocarbons can be enhanced by the limitation in a nanovoid which may increase the re-adsorption and the secondary reactions of α-olefins. Then, long-chain hydrocarbons may be catalyzed the cracking, isomerization, and aromatization reactions by the acidic site of zeolites, contributing to changing of the product distributions [29-31].

The hydrogenation of CO over zeolite-supported mono- or bimetallic catalysts has been reported in several reviews [32, 33]. Faujasite zeolites (X and Y) are large pore zeolite and have been found to be the most efficient support of FTS catalyst. Ru/NaY catalyst was reported to be high active for FTS reaction under the conditions of T = 229 °C, P = 2.1 MPa, and H_2/CO = 2 [34]. The faujasite-confined Co nanoparticles were prepared by ion-exchange of Co^{2+} into the zeolite [32, 35]. A lower C_{5+} selectivity and higher CH_4 selectivity were found in FTS reaction over the catalyst with small cobalt crystallite size [32]. Cobalt nanoparticles could be prepared by the reduction of the Co^{2+}-exchanged zeolite with $NaBH_4$ aqueous solution [35]. The cobalt supported on faujasite catalyst prepared by this method showed lower C_{21+} selectivity and higher C_5–C_{20} selectivity than that of Co/SiO_2 catalyst. It can be explained that the supercage structure of zeolite can cut heavier hydrocarbons. MCM-22 is a high-silica zeolite which shows high external surface area and low fraction of micropores and was also

employed as a support for FTS catalysts [36]. The selectivity Co supported on MCM-22 catalyst depended on the Si/Al ratio and the degree of H^+ exchange. The increasing Si/Al ratio increased C_{5+} selectivity but decreased CH_4 selectivity. Under the conditions of T = 280 °C, P = 1.25 MPa, and H_2/CO = 2, the Co/Na-MCM-22 (Si/Al = 200) showed a lower CH_4 selectivity and a higher C_{5+} selectivity than Co/SiO_2 [36].

2.1.2.3 Hybrid and core-shell catalysts

A fundamental concept on direct production of isoparaffins over physical mixture of a FTS catalyst and a zeolite component were carried out both in one reactor and a consecutive dual reactor system [37-39]. Furthermore, there have been three broad types of method that have been developed for the combination of the FT synthesis catalyst and zeolite. These are the (i) zeolite supported metal-based catalysts [40, 41], (ii) physical mixing of the metal-based catalyst and zeolite [42-46] and (iii) coating zeolite on the supported metal catalyst [8, 47-49].

A physical mixture of Co/SiO_2+Pd/SiO_2+ZSM-5 catalyst was reported [42]. The modification of Co/SiO_2 by adding ZSM-5 suppressed the formation of heavy hydrocarbon product and increased gasoline product; however, this catalyst was deactivated slowly from about 10 h time-on-stream. The addition of Pd/SiO_2 to Co/SiO_2+ZSM-5 catalyst decreased olefin content and increased catalysts lift time because Pd stabilized the acidic sites of zeolite via spillover effect of hydrogen.

The contact between the FTS catalyst and zeolite was developed by Tsubaki and co-workers [47, 49-51]. The pellets of FTS catalyst, such as Co/SiO_2 or Co/Al_2O_3, were coated with zeolite membrane by a hydrothermal synthesis method. The thickness of zeolite membrane was controlled by crystallization time of zeolite. In the production of isoparaffin over these zeolite capsule or core–shell catalysts, syngas arrived to the FTS catalyst through the zeolite layer, and then the primary product from FTS catalyst diffused through zeolite and these product were isomerized and cracked by zeolite, as shown in Figure 1 [50, 51]. As a result, light isoparaffin was synthesized by one step only and all heavy hydrocarbons were eliminated.

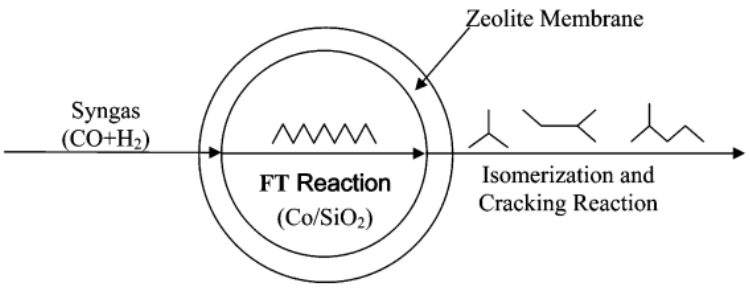

Figure 1 A schematic of the production of isoparaffin over capsule catalyst [51]

2.1.3 Synthesis of Cobalt Fischer–Tropsch Catalysts

The performance of the cobalt catalyst in FTS reaction is greatly influenced by the catalyst preparation method and it is correlated to the number of active metals [52, 53]. FTS catalysts have been prepared by several methods such as impregnation [5, 8, 9, 18, 22, 40], precipitation [54-56], colloidal method [57-59], strong electrostatic adsorption [52, 60], and microemulsion method [2, 61, 62].

2.1.3.1 Impregnation

The incipient wetness impregnation method is a commonly technique for preparing supported metal catalysts. The impregnation method consists of three steps of preparation. Firstly, the required amount of the precursor salt i.e. cobalt(II) nitrate hexahydrate is dissolved in deionized water and added dropwise to the support under constant stirring. Then, the sample is dried in an oven at 120 ℃ overnight. Finally, the catalyst is calcined at the proper temperature and time [63]. There are several parameters can affect the properties of the obtained catalyst such as type of precursor, rate of the increasing temperature, and temperature of calcination. The slurry (wet) impregnation method is also used to prepare supported cobalt catalyst. For this type of impregnation, the volume of impregnation solution is higher than the total pore volume of support. Impregnation method can prepare small particles of metal but difficult to obtain narrow particle size distribution, as depicted in Figure 2.

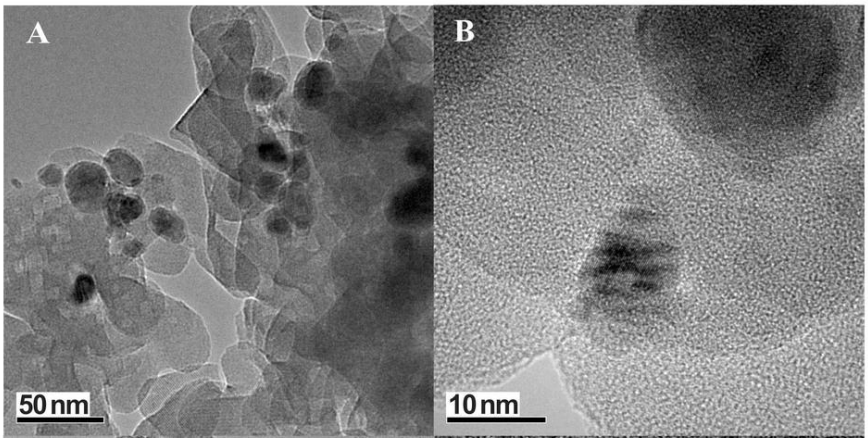

Figure 2 TEM images of the Co/H-ZSM-5 catalysts prepared by impregnation method [64]

2.1.3.2 Precipitation

The precipitation is a common method for iron catalyst preparation. However, the cobalt-based catalysts has been prepared by this method. Khassin et al. [64, 65] studied to prepare cobalt-alumina catalysts by either coprecipitation of Co^{2+} and Al^{3+} ions or Co^{2+} ion onto Mg-Al or Zn-Al hydrotalcite. They reported that, the decomposition of cobalt oxide phase deposited on hydrotalcite by inverted spinel-like structure at moderate temperatures. The obtained Co-Al catalysts exhibited low reducibility; however, cobalt reduction could be up to 100% after Co-Al catalysts were promoted by Mg^{2+} or Zn^{2+} and promoted catalyst displayed high distribution of cobalt metal phase.

2.1.3.3 Colloidal method

Colloidal synthesis is a preparation method that can synthesis nanosized catalyst by using stabilizer in order to control particle size and composition of catalyst. Typically, catalyst are added into solution which contains a solvent with dielectric constant of 5.01, then a colloid forms in solution. The catalyst particles are absorbed by the ionomer colloid and then ionomers link continuous network resulting in catalyst layers formation. The polyol process are applied produce nanosized catalyst and modified coordination capture as same as colloidal method. For example, the monodispersed iron nanoparticles were prepared by the alcohol reduction of iron(III) acetylacetonate at high temperature [66]. In the colloidal method, the surfactant-stabilized colloids is essential to disperse and stabilize nanoparticles in the solvent

[67, 68]. The colloidal method had prepared high dispersion of iron nanoparticles with average size of 10 nm, as depicted in Figure 3.

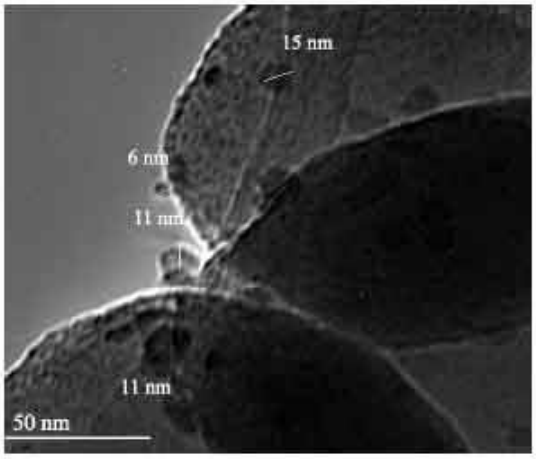

Figure 3 TEM image of 6 wt% Fe/SiO_2 prepared by colloidal method [70]

2.1.3.4 Strong electrostatic adsorption method

Strong electrostatic adsorption (SEA) is a catalyst preparation method which is based on basic concept of electrostatic attraction of oppositely charged particles [60, 69]. Silica and other metal oxides contain hydroxyl groups on its surface. Point of zero charge (PZC) is the pH value of a medium where the hydroxyl groups on the surface of the support remain neutral. In a pH<PZC medium, the hydroxyl groups will be protonated and become positively charged and thus attracting anions. When pH>PZC, the hydroxyl groups will deprotonate and became negatively charged and attracting cations. In other words, pH value plays an important role in the deposition of metal precursor. The SEA method was able to produce nanocatalyst of spherical-shaped Co nanoparticles on SiO_2 support, shown in Figure 4, with Co average size of 3 nm [52].

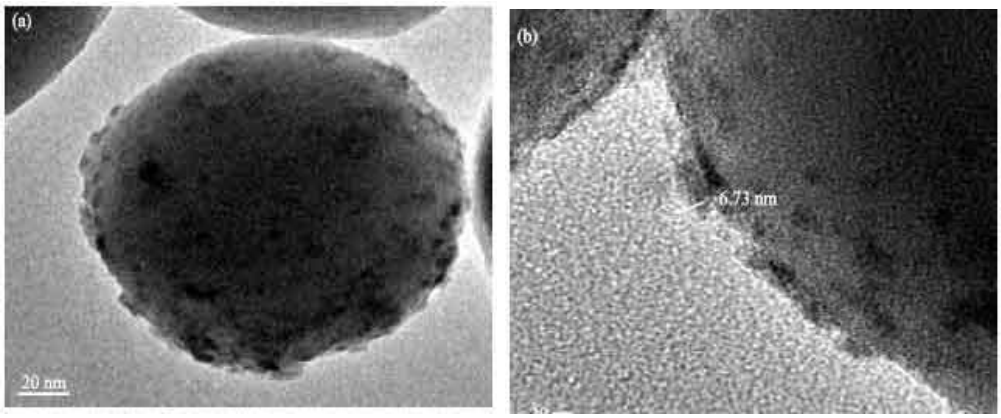

Figure 4 TEM image of 5 wt% Co/SiO_2 prepared by SEA method [52]

2.1.3.5 Microemulsion Method

This method usually involves microemulsion stabilizer. A stabilizer (emulsifier) is a molecule that possesses both polar and nonpolar moieties. In diluted water (or oil) solution, emulsifier dissolves and presents in the form of monomer. When the concentration of emulsifier exceeds the critical micelle concentration, the molecules of emulsifier associate spontaneously to form aggregates-micelles. Formation of oil-in-water (o/w) or water-in-oil (w/o) reverse micelles could be driven by hydrophobic or hydrophilic interactions of the hydrophobic tail or hydrophilic polar group, respectively. A particle size in the range of 5-50 nm depends on the size of microemulsion droplets and can be controlled by adjusting the water to surfactant ratio or concentration of reagents. These small microemulsion droplets can be viewed as nanoreactors [70]. The metal particles produced by this method usually have a spherical shape, as shown in Figure 2.4. Modification of the synthesis procedure, however, could result in rods or rings [71].

2.2 Zeolite ZSM-5

ZSM-5, first made by Argauer and Landolt in 1972 [72, 73], is a medium pore (~6 Å) zeolite with three-dimensional channels. The MFI framework contains a characteristic [5^8] unit with *D2d* symmetry. These units are linked via edge sharing to form a pentasil chain parallel to the *c* axis. These pentasil chains related by a mirror plane are connected via oxygen bridges to form corrugated sheets with 10-ring holes. The sheet parallel to the (100) plane is shown in Figure 5a. Adjacent sheets that are related by an inversion center are linked by oxygen bridges to the next, forming a 3-dimensional framework. This produces an intersecting channel system with straight 10-

ring channels (5.3 × 5.6 Å) parallel to corrugation (along *y*), and sinusoidal 10-ring channels (5.5 × 5.1 Å) perpendicular to the sheets (along *x*) with an angle of 150° (Figure 5b).

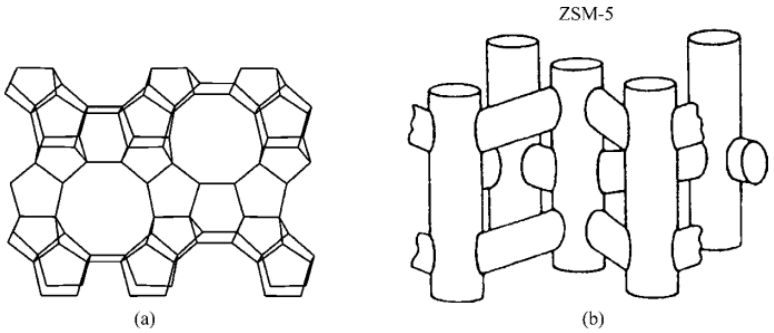

Figure 5 (a) Porous sheet parallel to the (100) plane in ZSM-5; (b) the channel structure in ZSM-5

2.2.1 Hydrothermal Synthesis

Most of the microporous materials such as zeolites, metal phosphates, microporous aluminophosphates, oxides, and sulfides have been synthesized via hydrothermal synthetic reactions [74]. Hydrothermal synthesis is the synthetic reactions conducted at appropriate temperature (100 ~ 1000 °C) and pressure (1 ~ 100 MPa) in aqueous or organic solvents in high-pressure autoclave. The studies on hydrothermal synthesis have mainly focused on the reactivity of raw materials, regularities of synthetic reactions and conditions, and their relationship with the structures and properties of products.

2.2.2 Properties of Reaction Media

The conventional hydrothermal synthesis process is steered in a certain range by using structure-directing agents (templates) to obtain zeolites with the desired channel system and structure type. The physicochemical properties of ZSM-5 zeolite is influenced by chemical composition and nature of the reagents, alkalinity, template, temperature, time of crystallization, water contents and other factors such as ageing and stirring [75, 76].

2.2.2.1 Water

Under high temperature and pressure of hydrothermal conditions, the properties of water will be significantly changed. These conditions can speed the rate of a reaction among the complex ions, intensify the hydrolysation reaction, and significantly change the redox potential of the reactants. The reactions of organic compounds with polar bonds usually have some characteristics of ionic reactions. Therefore, when the medium is water and the system is heated above its boiling point in a sealed container, the ionic reaction rate will be certainly accelerated. In general, an overall dilution of the synthetic mixture causes large crystal can be produced.

2.2.2.2 Organic Solvents

Several types of organic solvents which have different properties were added into reaction media. Alcohols are also used as solvent in hydrothermal synthesis. The added solvent is a media of system and dissolves reactant to form complex of solvent and reactant, so the chemical reaction rate can de change. Furthermore, the reaction process can be modified by the concentration of reactant which is also effected from solvent. The classification of organic solvent is usually based on the macroscopic and microscopic molecular parameters such as molecular weight (MW), density (*d*), melting point (*mp*), boiling point (*bp*), molecular volume, heat of evaporation, dielectric constant (ε), dipole moment (μ), and solvent polarity.

2.2.2.3 Si and Al sources

The physical and chemical properties of the reactants have an important effect on the crystallization of zeolite. Fumed silica, tetramethylorthosilicate (TMOS), and tetraethylorthosilicate (TEOS) are commonly used as Si sources in zeolite synthesis. Silica with high surface areas is more easily dissolved in basic medium than that with low surface area. This property leads to a higher supersaturation and a faster nucleation; therefore, small crystals are produced. The Al sources commonly used in zeolite synthesis are sodium aluminate, pseudo-boehmite, aluminium hydroxide, aluminium nitrate, aluminium sulfate, and aluminium metal. Using different Al precursor can produce different type of zeolite under exactly the same conditions.

2.2.2.4 Si/Al ratio

The Si/Al ratio has effect in determining the structure and composition of the crystallized zeolite [77]. Normally, zeolites with low Si/Al ratio (Si/Al ≤ 5) are prepared from strong alkalinity mixtures with a low Si/Al ratio, while high silica zeolite (Si/Al ≥ 5), such as zeolite beta (BEA), ZSM-5 (MEL), and ZSM-5 (MFI), are prepared from weak alkalinity mixtures with a high Si/Al ratio. Therefore, the Si/Al ratio in zeolite product is controlled by Si/Al ratio in reaction mixture.

2.2.2.5 Alkalinity

Zeolites are commonly produced in basic mixture system. A higher alkalinity increases the solubility of the Si and Al sources and the polymerization of the polysilicate and aluminate anions. Thus, the increase of alkalinity will shorten the induction and nucleation periods and accelerate the crystallization of zeolite.

2.2.2.6 Organic template

The structure directing agent (SDA) or template is usually added to the synthesis mixture in at least stoichiometric amounts in order to ensure complete crystallisation and maximum void filling of the product. At lower levels of addition, the most usual result in single-phase systems is a reduced yield of fully SDA-loaded product, rather than any significant reduction in the degree of void filling. However, in reactions where several product phases can crystallize, other notable effects may be observed at low template concentrations, in some cases showing a major influence on the product formed. ZSM-5 zeolites with similar Si/Al ratio were synthesized using various templates (n-butylamine, ethylamine, isopropylamine, ethylenediamine, ethanol, ethanol–ammonium and no template) under hydrothermal conditions. The obtained ZSM-5 with different templates had different morphology and particle size [72].

2.3 Electrospinning

Electrospinning is a simple and versatile method for producing nanofibers from a rich variety of materials that include polymers, composites and ceramics [78, 79]. This method involves the use of a high voltage electrostatic field to charge the surface of a polymer solution, sol-gel, droplet and thus to induce the ejection of a liquid jet through a spinneret (Figure 6). In a typical process, an electrical potential is applied

between a droplet of a solution contact at the end of a capillary tube and a collecter. When the applied electric field applies, a charged jet of solution is ejected.

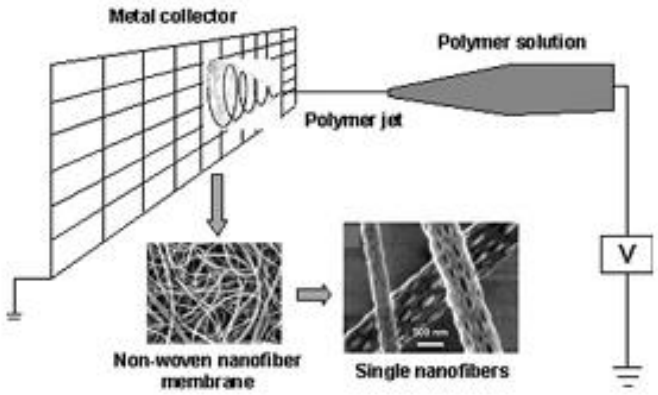

Figure 6 Schematic of polymer nanofibers production by electrospinning [94]

2.3.1 Parameters of the Electrospinning Process

The following parameters and processing variables affect the electrospinning process [80-82]: (a) The polymer solution properties, such as viscosity, elasticity, conductivity, and surface tension; (b) The process parameters, such as the gap distance between the capillary tip and the collector, applied voltage, and hydrostatic pressure in the solution container; and (c) The environmental effects, such as temperature, humidity, and air flow.

2.3.2 Solution property

In order to carry out electrospinning, the polymer or precursor must first be in a liquid form. The property of the solution plays a significant role in the electrospinning process and the electrospun fiber morphology.

2.3.2.1 Surface tension

Surface tension plays a critical role in the electrospinning process and by reducing the surface tension of a nanofiber solution; fibers can be obtained without beads. Different solvents may contribute different surface tensions. Generally, the high surface tension of a solution inhibits the electrospinning process because of instability of the jets and the generation of sprayed droplets [83]. Yang et al. [84] investigated the influence of surface tensions on the morphologies of electrospun products with

poly(vinyl pyrrolidone) (PVP) as model with ethanol, *N*,*N*-dimethylformamide (DMF), and dichloromethane (MC) as solvents (Figure 7). They found that different solvents may contribute different surface tensions. With the concentration fixed, reducing the surface tension of the solution, beaded fibers can be converted into smooth fibers.

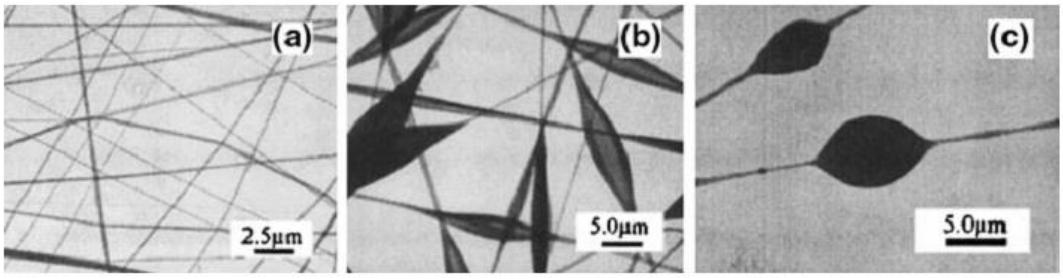

Figure 7 TEM images of the PVP nanofibers prepared from ethanol (a), MC (b), and DMF (c), respectively [86].

2.3.2.2 Viscosity

The viscosity of the solution has a profound effect on electrospinning and the resultant fiber morphology. Generally, the viscosity of the solution is related to the extent of polymer molecule chains entanglement within the solution. At slightly higher viscosities, a combination of small droplets and smooth fibers was obtained [85]. Further increasing the solution viscosity resulted in a reduced number of beads and increased fiber diameters. At high enough solution viscosities, only smooth fibers were present. At lower viscosity where generally the polymer chain entanglements are lower, there is a higher likelihood that beaded fibers are obtained instead of smooth fibers. Additionally, the diameters of the obtained fibers were found to increase with increasing solution viscosities.

2.3.2.3 Volatility (evaporation)

During the electrospinning process, the solvent will evaporate as the electrospinning jet accelerates towards the collector. When most of the solvents have evaporated when the jet reaches the collector, individual fibers are formed. However, if the rate of evaporation of the solvent is too low such that the solution has not evaporated sufficiently when the electrospinning jet reaches the collector, fibers may not be formed at all and a thin film of polymer solution are deposited on the collector. Bognitzki et al. [86] used highly volatile solvents to produce poly-l-lactide (PLLA) fibers

and obtained electrospun fibers with pore sizes of 100 nm in width and 250 nm in length along the fiber axis. Lee et al. [87] studied the effect of volume ratio of the solvent on the fiber diameter and morphology of poly(vinyl chloride) (PVC) fibers. They found that as the amount of DMF in the tetrahydrofuran (THF)/DMF mixed solvent increased, the average fiber diameter decreased.

2.3.2.4 Conductivity

For electrospinning process to be initiated, the solution must gain sufficient charges such that the repulsive forces within the solution are able to overcome the surface tension of the solution. Subsequent stretching or drawing of the electrospinning jet is also dependent on the ability of the solution to carry charges. The presence of acids, bases, salts and dissolved carbon dioxide may increase the conductivity of the solvent. Substances that can be added to the solvent to increase its conductivity includes mineral salts, mineral acids, carboxylic acids, some complexes of acids with amines, stannous chloride and some tetraalkylammonium salts. For organic acid solvents, the addition of a small amount of water will also greatly increase its conductivity due to ionization of the solvent molecules. Zong et al. [88] reported that with 1 wt% salt addition in biodegradable poly-l-lactic acid polymer solution, the resulting nanofibers were bead-free, with relatively smaller diameters in the range of 200-1000 nm.

2.3.3 Process conditions

Another important parameter that affects the electrospinning process is the various external factors exerting on the electrospinning jet [89-91]. This includes the voltage supplied, the feedrate, temperature of the solution, type of collector, diameter of needle and distance between the needle tip and collector. These parameters have a certain influence in the fiber morphology although they are less significant than the solution parameters.

2.3.3.1 Voltage

The applied voltage is an important parameter to induce charges on the solution for initiating the electrospinning process. When the electrostatic force in the solution higher than the surface tension of the solution, the solution will be ejected from the needle tip. Generally, both high negative or positive voltage of more than 6 kV can produce the solution drop at the needle tip and stretch jet of solution [92]. If

the applied voltage is higher, the greater amount of charges are occurred. As a result, the solution jet is highly accelerated, amount of solution drawn from the needle tip is increased and then the diameter of the fibers decrease. At a lower voltage, the formation of finer fibers are produce because the reduction of acceleration of the jet and the weaker electric field result in an increase the flight time of the electrospinning jet. If the applied voltage is too high, the beads density are increased and a larger fibers are produced due to instability of the jet. For the polyethylene oxide-water system, it was observed that the fiber morphology changed from a finer fiber at voltage of 5.5 kV to a highly beaded structure at 9.0 kV [93]. Megelski et al. [94] determined the dependence of the fiber diameter of polystyrene fibers on voltage, and showed that the fiber size decreased more or less from 20 μm to 10 μm without a dramatic change in the pore size distribution when the voltage was increased from 5 kV to 12 kV.

2.3.3.2 Feed rate

The feed rate will determine the amount of solution available for electrospinning. For a given voltage, there is a corresponding feed rate if a stable Taylor cone is to be maintained [95]. When the feed rate is increased, there is a corresponding increase in the fiber diameter or beads size as shown in Figure 8 [96]. This is apparent as there is a greater volume of solution that is drawn away from the needle tip However, there is a limit to the increase in the diameter of the fiber due to higher federate. If the feed rate is at the same rate which the solution is carried away by the electrospinning jet, there must be a corresponding increase in charges when the feed rate is increased [97]. Thus there is a corresponding increase in the stretching of the solution which counters the increased diameter due to increased volume.

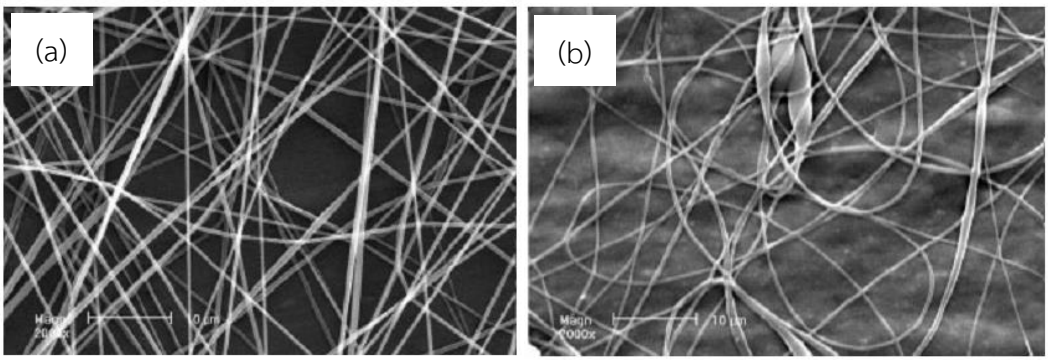

Figure 8 SEM images of the ultrafine PSF fibers electrospun: flow rate = 0.40 ml h^{-1} (a) and 0.66 ml h^{-1} (b) [98]

Due to a higher volume of solution drawn from the needle tip, the jet will takes a longer time to dry. As a result, the solvents in the deposited fibers may not have enough time to evaporate given the same flight time. The residual solvents may cause the fibers to fuse together where they make contact forming webs. A lower feedrate is more desirable as the solvent will have more time for evaporation.

2.3.3.3 Temperature

The temperature of the solution has both the effect of the evaporation rate and the viscosity of the polymer solution. When polyamide is electrospun at a higher temperature, the produced fibers have a more uniform diameter as shown in Figure 9 [85]. At higher temperature, the viscosity of the solution is decreased but solubility of the polymer is increased resulting in more stretching of the solution. At a lower viscosity, a smaller fibers are produced as a result of an increase the stretching force on the solution by columbic forces.

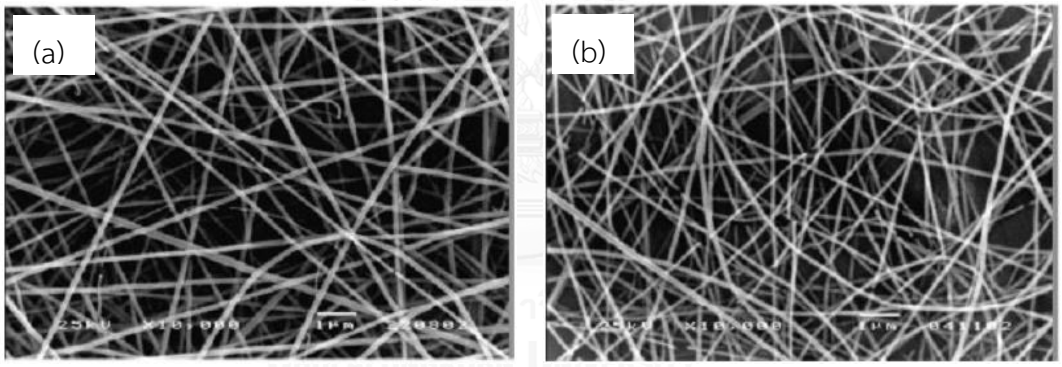

Figure 9 SEM images of electrospun polyamide fibers obtained from solution temperatures of (a) 30 and (b) 60 ℃ [87]

2.3.3.4 Diameter of needle

The inner diameter of needle has an effect on the elecstrospun fiber morphology. Using small inner diameter was found that the clogging at the tip of needle and the formation of beads on fiber decreased. The clogging of solution was reduced because the solution slightly contacted with atmosphere during electrospinning. A small inner diameter also decreased the diameter of the electrospun fibers due to the decreasing of the size of the droplet at the tip. At the same voltage supplied, a smaller diameter required a high columbic force to eject solution from the tip. As a result, the solution had enough time to stretch and elongate

before it arrived to collector. However, if the diameter of needle is too small, the solution is hardly extruded from the needle tip.

2.3.3.5 Tip to collector distrance (TCD)

The tip to collector distrance (TCD) has a direct influence in both the flight time and the electric field strength. The electrospinning jet which was ejected from the needle tip have to require time for evaporating of solvent [98]. At a short of TCD, the jets have a smaller distance to arrive the collector and the electric field strength increase lead to the increasing of the acceleration of the jet. When the distance is too low, the fiber can be merge and intra layer bonding are occurred because the solvent cannot completely evaporate. Furthermore, the increasing of electric field strength at a shorter of TCD may increase the formation of beads [99]. At a longer of TCD, a larger fiber diameters are observed because the electrostatic field strength decrease resulting in less stretching of the fibers [100].

2.3.4 Environment parameters

Environmental parameters such as temperature and humidity may effect on the electrospun fiber morphology. The formation of pores on the surface of the fibers can be occurred under high humidity [103], because the rate of evaporation of the solvent is decreased at high humidity. At a low humidity, the evaporation of the solvent may be faster than the ejection of the solution from the needle to collector which leads to the clogging of the needle tip by reactant.

2.4 Literature review

Cheng et al. [101] prepared polyimide/silica hybrid nonwoven nanofiberous fabrics by combining the electrospinning technique and the in situ sol–gel process. The nanofiberous fabrics were prepared by electrospinning of the solution of tetraethoxysilane (TEOS) and polyamic acid (PAA). They found that the TEOS hydrolysis and silanol condensation process were controlled by acid and water content. The thermal stability was greatly enhanced by increasing the silica content in the materials. The ultimate tensile strength was also significantly increased in certain range of silica content, compared to the pure polymer.

Lee et al. [102] studied the direct formation of silica/titania, $(1\text{-}x)SiO_2/(x)TiO_2$ composite fibers using the sol–gel method and electrospinning technique. The SEM results showed that the diameter of fiber varied from hundreds

of nanofibers to 5 μm. It is also seen that the average diameter of the as-spun the fibers increases with increasing titania content. The limitation in the titania content in a composite sol for suitable fiber spinning is about 50 mol% (x = 0.5). They found the surface morphology of fiber are influenced by calcinations temperature and titania content.

Jiao et al. [60] prepared a series of silica-supported noble and base metal catalysts prepared by strong electrostatic adsorption (SEA) method. Metal ammine complexes were adsorbed onto amorphous silica at various pHs. The results showed that the SEA method can be applied for many ammine complexes to synthesize well-dispersed metals over amorphous silica.

Zhu et al. [103] prepared Co_3O_4 supported on ZSM-5 catalysts by impregnation (IM), deposition precipitation (DP), and hydrothermal (HT) methods. The catalyst prepared by the HT method showed the highest catalytic activity for propane oxidation, and their catalytic activities are varied in the order of HT > DP > IM. The excellent catalytic activity of HT catalyst may be attributed to the better reducibility of Co^{3+}, higher Co^{3+} content, higher surface concentration, and fast migration of the lattice oxygen of Co_3O_4 on this catalyst. Furthermore, catalyst prepared by the HT method exhibits a high stability after being used at 500 °C for 40 h.

Jacobs et al. [22] focused on FTS over Co-based catalyst which different supports (e.g. Al_2O_3, TiO_2, SiO_2, and ZrO_2 modified SiO_2 or Al_2O_3) and a variety of promoters. The results showed that significant support interactions on the reduction of cobalt oxide species were observed in the order Al_2O_3 > TiO_2 > SiO_2. Ru and Pt promoters decrease the reduction temperature of cobalt oxide species, while Re enhances the reduction of Co species interacting with the support. On the other hand, non-reducible metal oxides promoter such as B, La, Zr, and K decreased the reduction temperature of Co species. Addition of Zr decreased the cobalt cluster size and decrease in reducibility may be caused by greater surface interactions between the smaller Co species and the support. The catalysts were evaluated by FTS reaction testing in the CSTR. They found that noble metal promoter addition with cobalt-supported catalyst increased activity of FTS reaction due to increasing the number of active sites.

Martínez et al. [33] prepared Co catalyst supported on nanofibrous γ-Al_2O_3 and commercial alumina and studied catalytic properties of catalysts for FTS. The nanofibrous alumina have the highest specific surface area (321 m^2/g), macropore volume (0.26 cm^3/g) and total pore volume (1.29 cm^3/g) and an intermediate pore size of 16.1 nm. Then, RuCo/ γ-Al_2O_3 catalysts were obtained by impregnation of the

alumina supports. The nanofibrous alumina showed high Co dispersion due to large support surface area. The catalysts evaluated in term of activity and selectivity during initial stages until at time-on-stream (TOS) above 7-8 h. The decrease in cobalt-time-yield at initial stage is observed for cobalt catalyst prepared from the smaller pore commercial alumina. On the other hand, the catalyst based on the nanofibrous alumina displays a low relative decrease in the cobalt-time-yield during the initial stages. They suggested that the very open porous structure of the nanofibrous alumina provides an enhanced CO diffusion to the active sites resulting in a relatively low activity loss during the transitory period. The nanofibrous catalyst displays the highest specific activity and productivity to diesel products.

Tavasoli et al. [104] investigated the FTS on carbon nanotubes (CNT) and γ–Al_2O_3 supported cobalt catalysts with different amounts of cobalt (15, 25, 35, and 40 wt.% cobalt). X-ray diffraction (XRD) indicated that average Co_3O_4 crystallite size in 15Co/CNT catalyst is smaller than 15Co/γ-Al_2O_3 catalyst. Higher surface area of CNT support in 15Co/CNT catalyst will lead to better distribution of particles, which in turn leads to lower cobalt cluster sizes. The temperature programmed reduction (TPR) shows that, using CNT, as cobalt catalyst support enhances the reducibility of catalyst. They reported that using CNT as cobalt catalyst support enhances the CO conversion, FTS and WGS reaction rates. The FTS rate and CO conversion are strongly dependent and proportional to the number of surface reduced active cobalt sites. The methane selectivity and C_2–C_4 light gases selectivity increases and the selectivity of liquid C_{5+} products decreases by using CNT as cobalt catalyst support. In FTS the larger cobalt particles are more selective to higher molecular weight hydrocarbons and the smaller particles are selective for methane and light gases.

Martínez et al. [45] studied the influence of the zeolite pore geometry and acidity in physical mixing of Co/SiO_2 and zeolite (50:50 wt/wt) catalysts in FTS performance. The zeolite cracked the long-chain n-paraffins formed on the Co catalyst to mainly gasoline-range products. The yield of light hydrocarbon products decreased with TOS due to the accumulation of carbonaceous deposits (coke) on the zeolite. The total amount of coke deposited increased with increasing pore dimensions of the zeolite in the order HZSM-5 < HMOR < HBeta < USYs. Moreover, the aromatic compound was mainly composition of coke in the large-pore zeolites. Aromatic coke is likely occurred from light olefins produced in the FTS through consecutive oligomerization, cyclization, and dehydrogenation reactions.

Kang et al. [40] compared the catalytic behaviors of Co catalysts supported on the ZSM-5 possessing a four different Si/Al ratio and found that ZSM-5 having a low

Si/Al ratio of 15 provided a better C_5–C_9 selectivity. The number of weak acid sites is higher on Co/ZSM-5 catalyst having a Si/Al ratio of 15, in the first desorption temperature region. Additionally, the total number of acid sites varies in the order of Si/Al = 15 > 25 > 140 > 250. At low Si/Al ratio, the presence of weak acid sites, large pore size, and small cobalt particle size are mainly responsible for showing a high catalytic performance due to the high reducibility of cobalt particles.

He et al. [51] prepared capsule catalyst by coating H-ZSM-5 zeolite on the surface of the Co/SiO_2 pellet and investigated their potential as catalyst for FTS reaction. The conventional Co/SiO_2 catalyst was prepared by incipient wetness impregnation method. Then, H-ZSM-5 membrane was synthesized in the solution of deionized water and ethanol, with TPAOH (tetrapropylammonium hydroxide) as template, $Al(NO_3)_3{\cdot}9H_2O$ and TEOS (tetraethyl orthosilicate) as Al and Si sources, respectively, with a SiO_2/Al_2O_3 ratio of 80:1. They found that the capsule catalyst had a core-shell structure. C_{10+} hydrocarbons were suppressed completely on this catalyst, and the selectivity of middle isoparaffins was considerably improved. Additionally, the zeolite membrane thickness increased by increasing a crystallization time of zeolite. Although the CO conversion on these capsule catalysts was slightly lower, they exhibited a better selectivity for light hydrocarbon synthesis.

CHAPTER III

EXPERIMENTAL

3.1 Materials and reagents

The starting materials used in this experiment were listed in Table 2.

Table 2 List of chemicals and sources

Chemicals	**Source**
Tetraethyl orthosilicate (TEOS; $Si(OC_2H_5)_4$, 95 % A.R. Grade)	Kanto Chemical
Hydrochloric acid 37.0%	CARLO ERBA
Alumimium nitrate nanohydrate ($Al(NO_3)_3{\cdot}9H_2O$, 99.9 % A.R. Grade)	Wako Pure Chemical
Tetrapropylammoniumhydroxide (TPAOH; $C_{12}H_{29}NO$, 10% A.R. Grade)	Kanto Chemical
Dehydrated ethanol (C_2H_5OH, 99.5 wt% A.R. Grade)	Kanto Chemical
Nitric acid (HNO_3, 69 wt% A.R. Grade)	Kanto Chemical
Ammonia solution (27%, A.R. Grade)	Wako Pure Chemical
Cobalt nitrate hexahydrate ($Co(NO_3)_2{\cdot}6H_2O$)	Wako Pure Chemical
Silica (Cariact Q-10)	Fuji Silysia Chemical
ZSM-5	Süd-Chemie catalyst
Nitrogen gas (99.99% purity)	Praxair
Hydrogen gas (99.99% purity)	Praxair
Carbon monoxide gas/Hydrogen gas (CO/H_2) 1:2	BOC Scientific
Helium gas (99.99% purity)	Praxair
Standard synthesis gas 20% of CO 20% of CH_4 and 20% H_2 bal He	BOC Scientific
Standard synthesis gas 100% of CO_2	Praxair

3.2 Catalysts preparation

3.2.1 Silica fibers (SF) preparation

Preparation of the silica sol solution: Based on conventional sol-gel process, tetraethyl orthosilicate (TEOS), ethanol, deionized water (DW) and 1 M hydrochloric

acid (HCl) at a molar ratio of 1:2:2:0.01, respectively, was used as the starting material. First, TEOS was mixed with DW and stirred for 5 min. Then, HCl and ethanol were added with continuous stirring for another 5 min. The precursor solution was heated to 55 ºC and stirred at this temperature for 30 min before being cooled to room temperature.

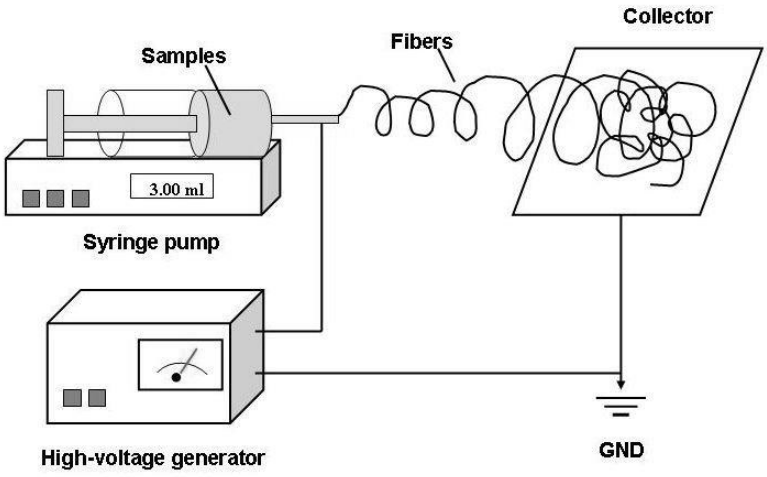

Figure 10 Schematic of the electrospinning process setup

Electrospinning process: All electrospinning experiments were performed at room temperature in air. A high voltage DC power supply was used to generate the required apply electrical potential difference (10, 15 and 20 kV). The electrospinning setup is shown in Figure 10. The silica sol solution was fed from a syringe through a needle (spinneret with a hole diameter of 0.25 mm) and the flow rate was controlled using a syringe pump (KDS 100, KD Scientific, Co.) at the achievable flow rate of 10 mL/h. A clamp connected with high voltage power supplier was attached to the syringe. For the grounded collector, a piece of aluminum foil was placed at a tip to collector distance (TCD) of 10, 15 or 20 cm from the needle tip. The electrospun SF were collected, then dried at 110 ºC overnight and then calcined at 600 °C for 4 h.

3.2.2 Preparation of the ZSM-5 modified SF (ZSM-5/SF)

The solution was prepared by adding TEOS dropwise into an aqueous solution containing 10 wt% tetrapropylammonium hydroxide (TPAOH) and the required amount of aluminium nitrate nonahydrate ($Al(NO_3)_3 \cdot 9H_2O$). All reagents were mixed at room temperature with 6 h of stirring. Then, the pH was adjusted with 1 M nitric acid (HNO_3) for reducing the silica fibers dissolution. The SF, which had a diameter of 650 nm and a surface area of 20 m^2/g, were placed in a Teflon-lined stainless steel autoclave (110

mL). The gel containing the support was put in an oven and the temperature was raised to 170 °C. The synthesis then took place during 24 h under autogenous pressure. After cooling, the sample was sonicated for 15 min to remove any residual gel and washed several times with DW. The solid was then dried at 120 °C overnight and subsequently calcined at 550 °C for 5 h. The final composition of the gel in molar ratios was shown in Table 2.

Table 3 Chemical compositions (molar ratio) of mixture for ZSM-5/SF

Samples	SiO_2	TPAOH	EtOH	H_2O	Al_2O_3	HNO_3
ZSM-5/SF-1	1	0.24	0	25	0.025	0.120
ZSM-5/SF-2	1	0.24	0	25	0.025	0.038
ZSM-5/SF-3	1	0.24	0	25	0.025	0
ZSM-5/SF-4	1	0.24	0	25	0.010	0.038
ZSM-5/SF-5	1	0.24	0	40	0.010	0.038
ZSM-5/SF-6	1	0.24	4	25	0.010	0.038
ZSM-5/SF-7	1	0.24	8	25	0.010	0.038
ZSM-5/SF-8	0.8	0.24	0	25	0.010	0.038
ZSM-5/SF-9	0.6	0.24	0	25	0.010	0.038
ZSM-5/SF-10	1	0.24	0	25	0.006	0.038
ZSM-5/SF-11*	1	0.24	0	25	0.010	0.038

*SF are soaked in a 2M HNO_3 solution before placed in synthesis mixture.

3.2.3 Preparation of supported cobalt catalysts

The ZSM-5 (H-MFI-90, 362.3 $m^2\ g^{-1}$, SiO_2/Al_2O_3 = 83.7 in molar ratio) and SF (S_{BET} of 20 m^2/g) were impregnated with the $Co(NO_3)_2{\cdot}6H_2O$ (10 wt%) to yield the Co/ZSM-5/SF, Co/ZSM-5 and Co/SF catalysts, respectively.

The Co/SF catalysts were prepared by wetness impregnation (IM), strong electrostatic adsorption (SEA), deposition precipitation (DP) with sodium hydroxide (DPNa) or ammonia (DPNH) solution and hydrothermal (HT), and were designated as Co/SF-X, where X stands for the preparation method. Silica (SiO_2) pellets (Fuji Silysia Chemical Ltd., Cariact Q-10, specific surface area 300 m^2/g) was compared porous to fiber support, and Co/SiO_2 catalyst was prepared by IM method. A theoretical 10 wt%. loading level of Co was used in all cases.

For the Co-SF-SEA catalyst, SF were added to DW (0.05 g/ mL) and the pH was adjusted to 12 by ammonia solution (28 wt.%). The required final concentration of

$Co(NO_3)_2$ solution was added, mixed and the solid was obtained by filtration and washed with DW until the eluate attained a constant pH 7. For the Co/SF-DP catalysts, $Co(NO_3)_2$ was dissolved in DW and then NaOH (1 M) or ammonia (28 wt%) solution (for the preparation of the Co/SF-DPNa and Co/SF-DPNH catalysts, respectively) was added slowly until the pH to 9. The SF were then added (0.01 g/ mL) and aged at room temperature for 12 h. The formed solid was filtered and washed with DW until the eluate attained a constant pH 7. The Co/SF-HT catalyst was synthesized with the same synthesis solution as for the Co/SF-DPNH catalyst, but was hydrothermally treated at 140 °C for 24 h in a Teflon-lined autoclave. All catalysts were dried at 120 °C for 12 h and calcined at 400 °C for 3 h under static air.

3.2.4 Preparation of composite ZSM-5 and Co/SF catalysts

The ZSM-5 deposited on the Co/SF sample was synthesized with the same synthesis method and solution described in 3.2.2 and the obtained sample was denoted as ZSM-5/Co/SF. For the physically mixed Co/SF and synthesized ZSM-5 catalyst (Co/SF+ZSM-5), ZSM-5 zeolite powder was mixed well with the Co/SF at a 1:1 weight composition ratio. Synthesized ZSM-5 was directly synthesized by the same method except without the inclusion of SF.

3.3 Catalyst characterization

3.3.1 Scanning electron microscopy (SEM)

The overall morphologies and diameters of samples and quantity of elements were obtained using a JEOL JSM-5410LV scanning electron microscope (Figure 11). The SEM was operated at 20 kV. After the SEM micrographs were taken, SEM with energy dispersive X-ray spectroscopy (SEM/EDS) was performed to determine the quantity of elemental in the catalyst granules.

Figure 11 Scanning electron microscopy (SEM: JEOL, JSM-6360LV)

3.3.2 X-ray diffraction (XRD)

X-ray diffraction patterns were acquired at room temperature in a Rigaku RINT 2000 instrument (Figure 12a) using monochromatized Cu-Kα radiation and scanned from 2° to 80° at 0.02° steps. The average particle size of Co_3O_4 in calcined catalysts was estimated from the Scherrer's equation applied to the most intense (311) diffraction (2θ = 36.9°).

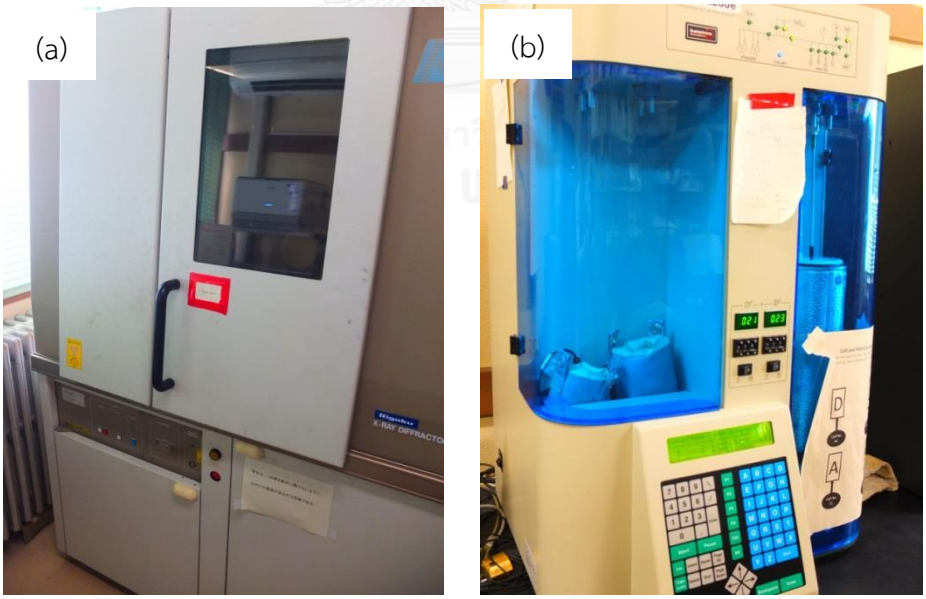

Figure 12 (a) X-ray diffractometer (XRD: RINT 2400, Rigaku. Co.), (b) BET surface area (Quantachrome NOVA 2200e)

3.3.3 N_2 physisorption

The Brunauer-Emmett-Teller (BET) surface area of samples were measured by N_2 physisorption at -196 °C on a Quantachrome NOVA 2200e instrument (Figure 12b). The samples (ca. 30 mg) were degassed at 200 °C for 2 h prior to analysis. Specific surface areas were estimated by using the BET approach. Average pore size and pore size distributions were obtained by applying the Barrett-Joyner-Halenda (BJH) analysis.

3.3.4 Transmission electron microscopy (TEM)

The cobalt oxide particle size and the dispersion of cobalt on SF with different preparation methods were observed using a TECNAI 20 TWIN transmission electron microscope operated at 120 kV.

3.3.5 Temperature-programmed reduction of H_2 (TPR)

The reduction behavior of the supported metal oxide phases was studied by hydrogen temperature-programmed reduction (H_2-TPR) in a BELCAT-B-TT instrument. About 30 mg of sample were initially flushed with a Ar flow at 180 °C for 60 min. The sample was then cooled down to 50 °C and flushed with Ar for 30 minutes. After that, the gas was switched to 10 vol% H_2 in Ar and the temperature increased up to 800 °C at a heating rate of 5 °C/min. Schematic of temperature-program for TPR measurement are showed in Figure 13. The H_2 consumption rate was monitored in a thermal conductivity detector (TCD).

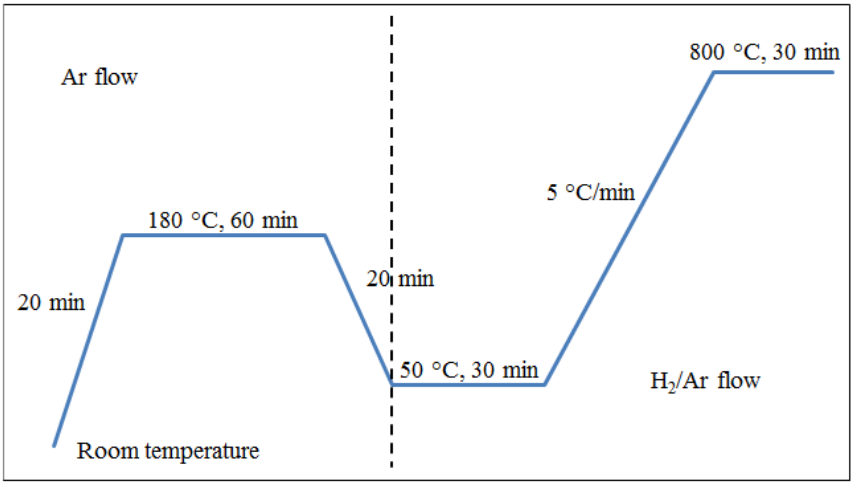

Figure 13 Schematic of temperature-program of TPR

3.3.6 Temperature-programmed desorption of NH_3 (TPD)

For determining the quantity and strength of the acid sites of the catalysts was studied by temperature programmed desorption of NH_3 in a BELCAT-B-TT instrument. About 30 mg of sample were firstly pretreated in flowing He at 150 °C for 60 min. After cooling down to 80 °C in He, each sample was then kept in ammonia flow for 30 min until the saturated ammonia adsorption was attained. The TPD was performed by ramping the sample temperature at 5 °C /min from 80 to 800 °C. Schematic of temperature program for TPD measurement are shown in Figure 14. The state of desorption was monitored in a thermal conductivity detector (TCD).

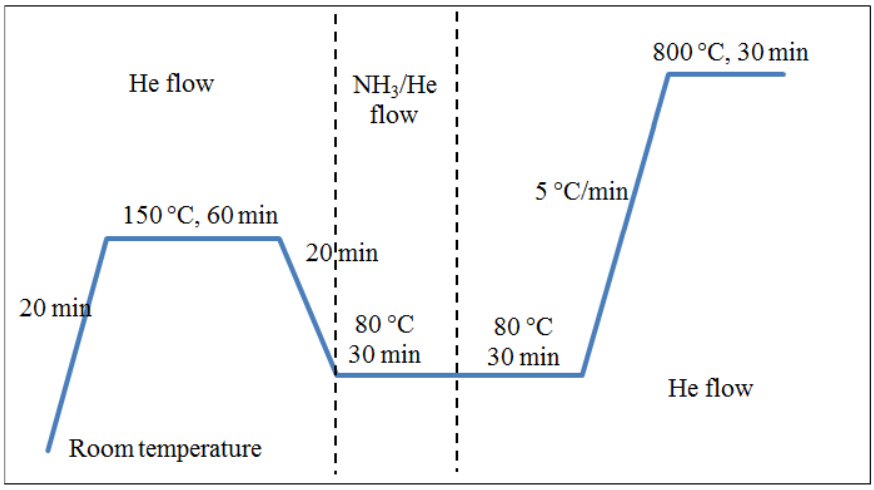

Figure 14 Schematic of temperature-program of TPD

3.3.7 Hydrogen chemisorption

The active metal surface of the Co/SF catalyst prepared by different methods was measured by H_2-chemisorption experiments carried out in a static volumetric glass high-vacuum system (Quantacharome Autosorb-IQC). The chemisorbed H_2 was measured at 100 °C using the method as described by Shi et al. [105]. Prior to adsorption, the samples were pretreated in flowing H_2 at 400 °C for 12 h. Thereafter, the samples were degassed at 1.3 Pa, and the temperature lowered to 100 °C. Average crystallite diameters in nanometers were calculated from *D*% assuming spherical metal crystallites of uniform diameter *d* with a site density of 14.6 at/nm^2. Thus, $d = 96/D$, where *D*% was the percentage dispersion.

3.3.8 Energy dispersive X-ray analysis (EDX)

The determination of the amount of metal in each catalyst was performed using energy dispersive X-ray analysis (EDX) on a Rayny EDX-700 instrument.

3.4 FTS reaction performance

The reaction performance of the catalysts in FTS process was evaluated in a tubular fixed-bed reactor (Figure 15) with a catalyst loading level of 0.5 g. Before the reaction, the catalyst was reduced at 400 °C for 12 h in H_2 flow (99.99%) of 80 mL·min^{-1}. After reduction, the synthesis gas, which had a H_2/CO molar ratio of 2, was fed into the reactor and the reaction was performed at 1.0 MPa, 240 °C, and a catalyst weight/feed flow ratio (W/F) of 10 g_{cat}·h mol^{-1}. The effluent gas from the reactor was analyzed by two online gas chromatographs. In the first, the CO, CO_2 and CH_4 levels were analyzed by a thermal conductivity detector and an active charcoal column, whilst in the second the C_1–C_5 light hydrocarbons were analyzed by a flame ionization detector (FID) with a Porapak-Q column. Liquid products were collected in a ice-bath cold trap and then were off-line analyzed on a Shimadzu GC-2014 gas chromatograph (Inertcap 5 capillary with dimensions of 0.4 mm thick, 0.25 ID and 30 m length) with FID.

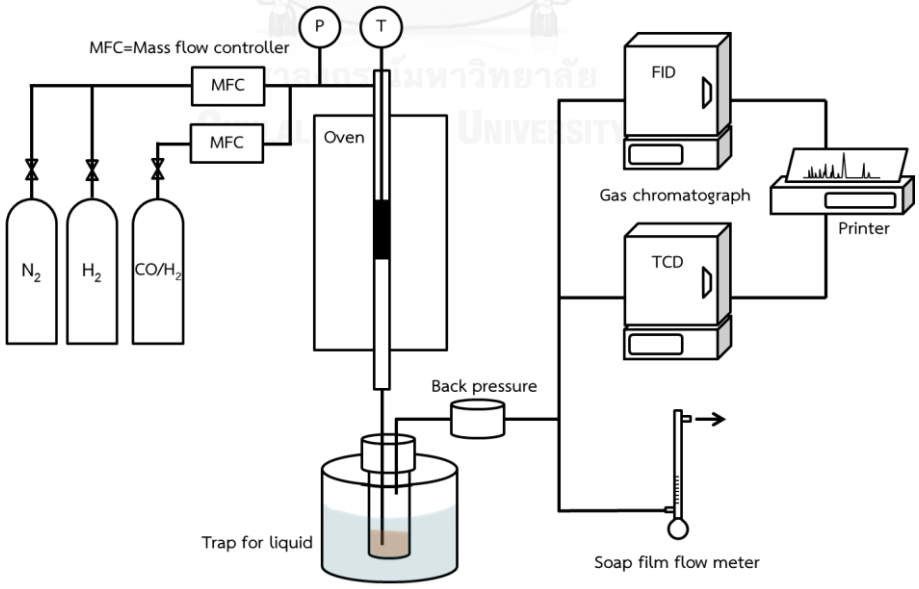

Figure 15 Reactor system for Fischer-Tropsch synthesis

CHAPTER IV
RESULTS AND DISCUSSION

4.1 Structural and textural properties of the SF

4.1.1 Effect of needle size

The effect of needle size on electrospun fiber was investigated by fixing the TCD and voltage at 15 cm and 15 kV, respectively. The electrospun fibers were shown in Figure 16. The SEM results showed that the average diameter of electrospun fiber was depended on the needle size. The increasing needle size resulted in an increase in the diameter of fibers because of a larger droplet at the tip of the needle. The large droplet decreased surface tension to require a higher columbic force for producing the jet initiation [83, 84]. As a result, the acceleration of the jet increased and this allowed less time for the solution to be stretched and elongated before it is collected which results in increased fiber diameters.

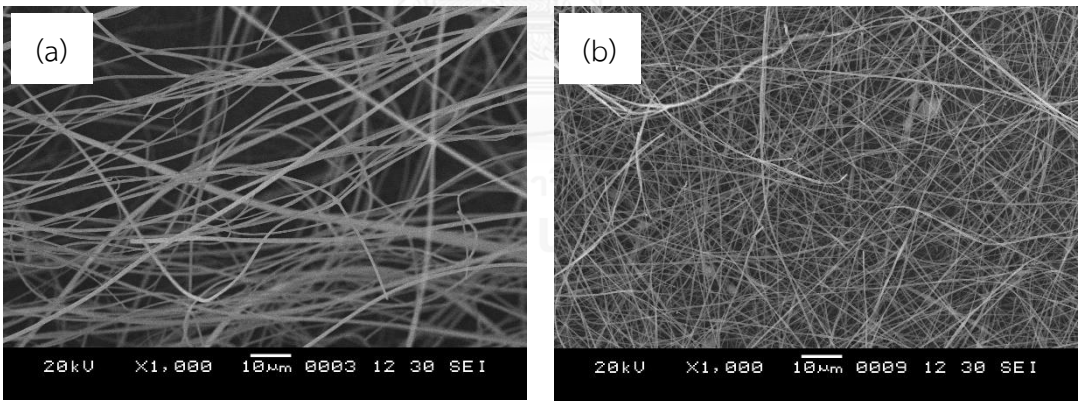

Figure 16 SEM images of electrospun fibers under different needle size, (a) 0.25 mm and (b) 0.10 mm at TCD = 15 cm and voltage = 15 kV.

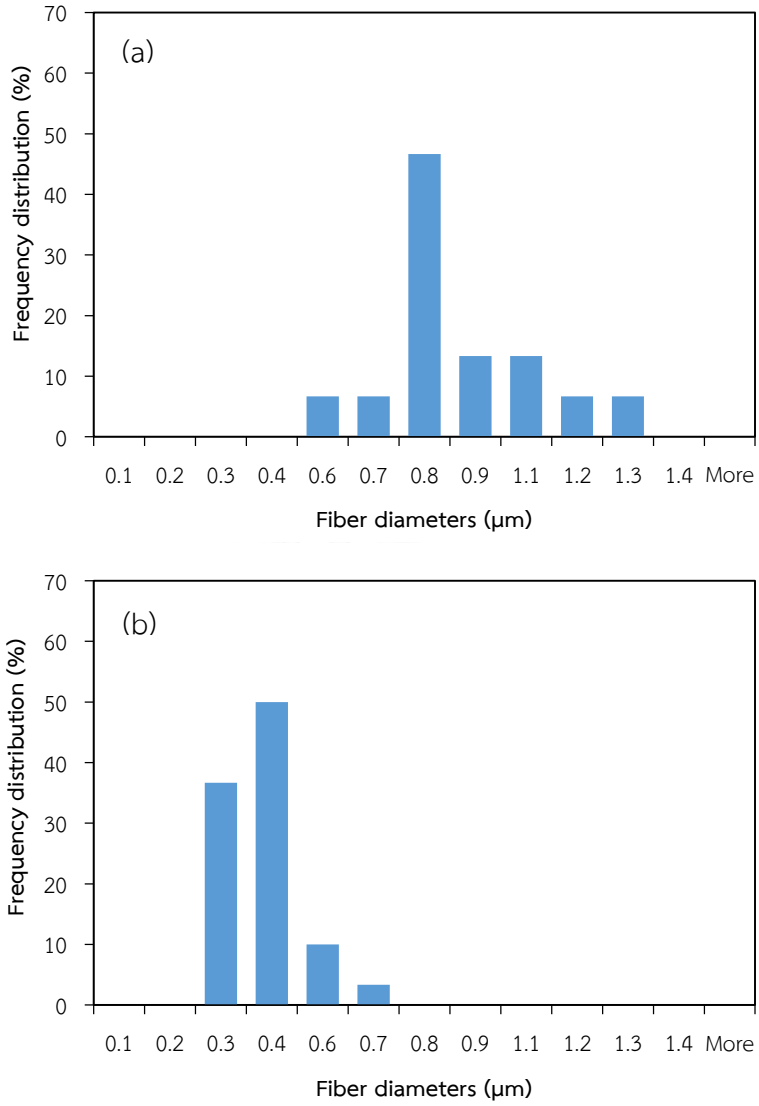

Figure 17 Diameter distribution of SF using different needle size: (a) 0.25 mm and (b) 0.10 mm. The tip to collector distance was 15 cm and voltage was 15 kV.

Figure 17 shows diameter distribution of SF which were prepared by needle size 0.25 mm (Figure 17a) and 0.10 mm (Figure 17b). As shown in Figure 17a, an electrospinning fiber with 0.25 mm of needle size results in the large average diameter (0.83 µm) and wide distribution. By decreasing the diameter of needle to 0.10 mm, the distribution of the fiber diameter becomes lower. These results clearly indicate that needle size can control the distribution of fiber diameter by the stretching process.

Table 4 The average diameter and morphology of the SF obtained after electropinning with different needle size, TCDs or applied voltages.

Parameter	Needle size (mm)	TCD (cm)	Voltage (kV)	Average diameter of fiber (μm)	Fiber Morphology
Needle size (mm)	0.25	15	15	0.83	Uniform, continuous fibers
	0.10	15	15	0.34	Uniform, continuous fibers with beads
TCD (cm)	0.25	10	15	1.09	Broken, discontinuous fibers with high numbers of beads
	0.25	15	15	0.83	Uniform, continuous fibers
	0.25	20	15	1.07	Uniform, continuous fibers
Voltage (kV)	0.25	15	10	0.51	Non-uniform, discontinuous fibers with beads
	0.25	15	15	0.83	Uniform continuous fibers
	0.25	15	20	1.64	Uniform continuous fibers

Features of the electrospun fibers with different processing parameters are summarized in Table 4. Beads were formed in the silica fibers with a needle size of 0.01 mm and clogging also occurred at the tip of needle. However, a bigger needle size led to bead free fibers as well as no clogging at the needle tip. The beads might be formed due to instability of the jet initiation which was correlated to solution property (viscosity and surface tension) as well as a force to pull polymer jet due to electric field and the boundary condition such as a needle size. Therefore, bead free fibers may be able to be electrospun from the thick needle tip with appropriate concentration solution [80]. A needle with a diameter of 0.25 mm was chosen for the following sections of this research in order to have uniform electrospun fiber and give high yield of fiber.

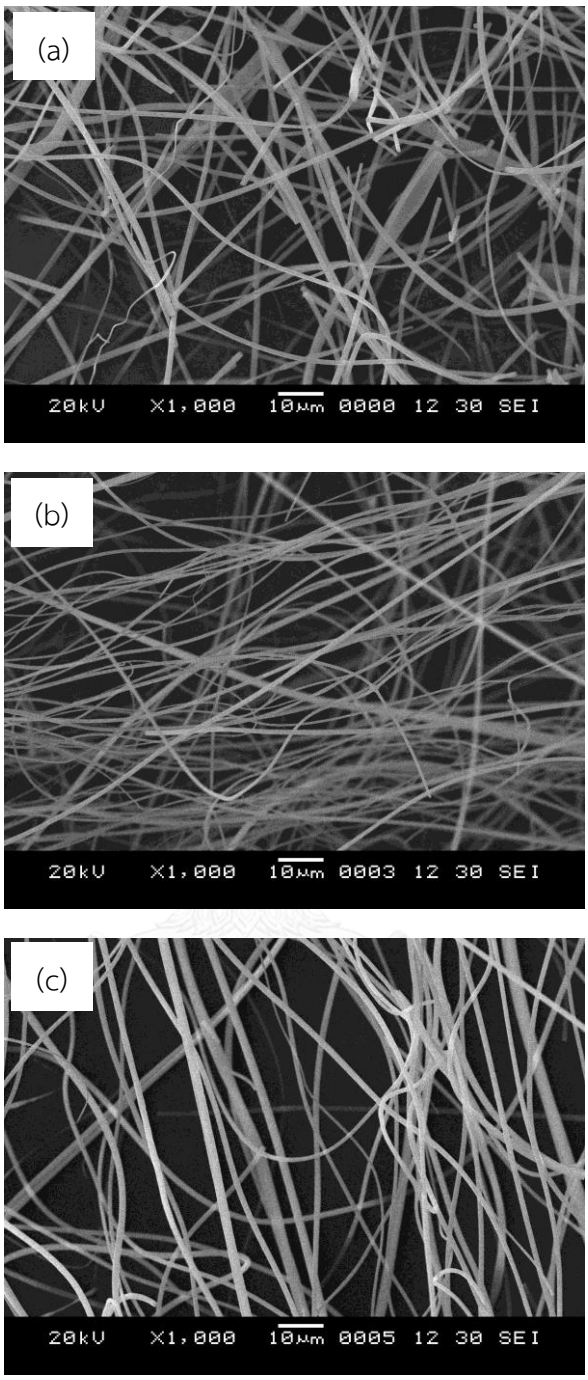

Figure 18 SEM images of the electrospun SF obtained with a TCD of (a) 10 cm, (b) 15 cm and (c) 20 cm. The needle size and applied voltage were fixed at 0.25 cm and 15 kV, respectively.

4.1.2 Effect of tip to collector distance (TCD)

The effect of the TCD and applied voltage on the obtained electrospun SF was investigated in a sequential univariate approach. For the effect of the TCD, the applied

voltage and needle size were fixed at 15 kV and 0.25 mm, respectively, and the TCD was varied at 10, 15 and 20 cm. The morphology of the obtained SF is shown in Figure 18, and their diameter is summarized in Table 4. Increasing the TCD from 10 to 15 cm decreased the average SF diameter to 0.83 μm, and the non-uniform SF morphology with beads and dumbbell-like jet fibers found at a TCD of 10 cm was changed to a bead free, uniform and continuous morphology at a TCD of 15 cm. The TCD distance likely influenced the flight time and the electric field strength, resulting in the smaller SF diameter [99] and smooth morphology [89]. The jet flight time and electric field strength were changed by to adjust tip to collector distance. The decreasing of TCD decreased flight times and solvent evaporation time, and increases the electric field strength resulting in bead formation [90]. Further increasing the TCD to 20 cm resulted a larger diameter, but presented a uniform and continuous morphology. Therefore, decreasing the distance between the needle and the collector can change morphology of fiber. Increasing of TCD decreases the bead density, regardless of the concentration of the solution [91].

The increased SF diameter with the increased TCD from 15 to 20 cm reflects the decreased electrostatic field strength and acceleration of the jet to the collector [81]. Figure 19 shows diameter distribution of silica fibers electrospun with TCD of 10 cm, 15 cm and 20 cm. The TCD of 10 and 20 cm appeared non-uniform size of SF. Thus, the most suitable TCD for electrospinning was selected as 15 cm to obtain small diameter SF with a high degree of continuity and uniformity.

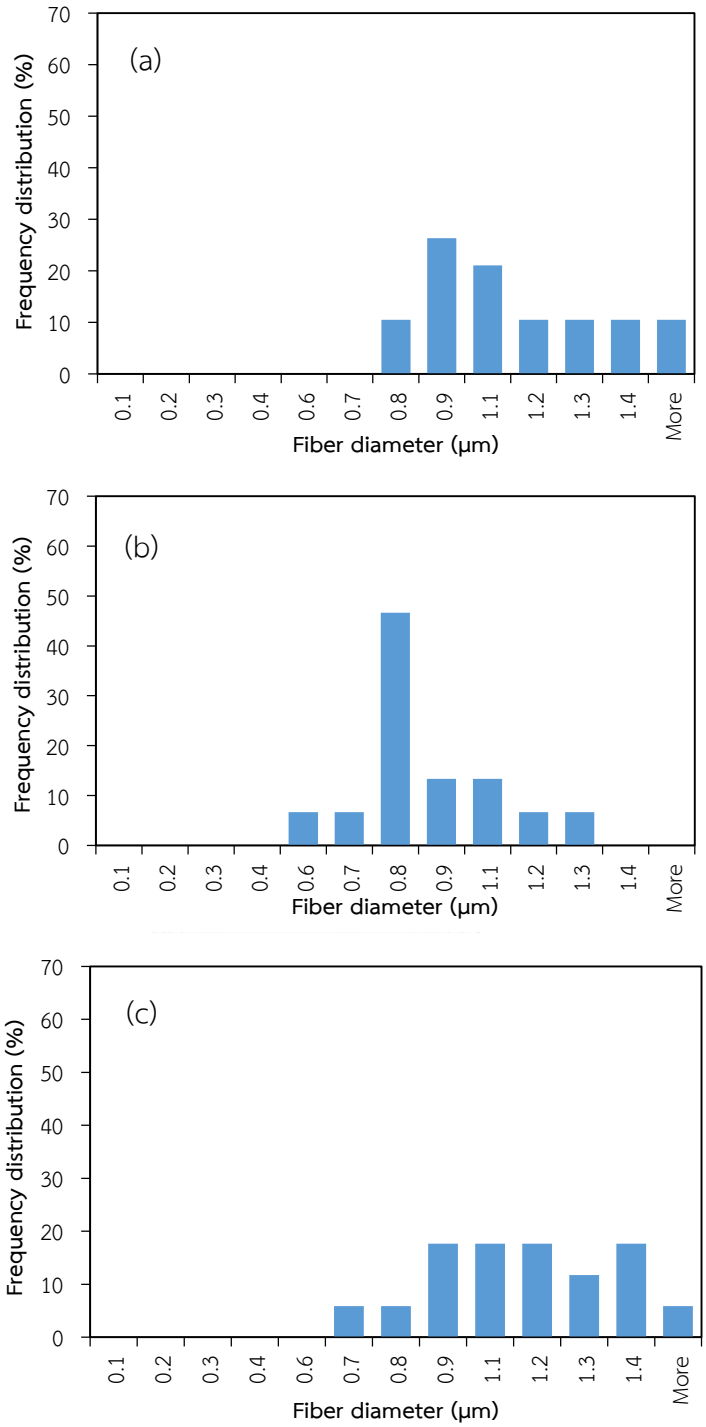

Figure 19 Diameter distribution of SF using different TCD: (a) 10 cm, (b) 15 cm and (c) 20 cm. The needle size and applied voltage were fixed at 0.25 cm and 15 kV, respectively.

4.1.3 Effect of applied voltage

The effect of the applied voltage on the electrospun SF was then evaluated at 10, 15 and 20 kV with a fixed TCD (15 cm) and needle size (0.25 mm). The SF diameters were obtained in the submicron range but increased with increasing applied voltage from 10 to 20 kV, exceeding 1 μm at 20 kV (Table 4). That average diameter of the electrospun SF increased with an increasing applied voltage reflects the effect of the increased charge increasing the columbic repulsive force in the jet and so leading an increased acceleration of the solution to the collection plate that exceeded the supply from the source. Thus, the Taylor cone recedes into the needle resulting in a smaller and less stable jet [88, 93]. However, despite their smallest size, the morphology of the SF formed from an applied voltage of 10 kV were discontinuous and non-uniform with beads, in contrast to the continuous and uniform SF produced at 15 and 20 kV (Figure 20). The decrease of the applied voltage causes decrease of the columbic repulsive force in the jet, which may decrease the draw rate in conventional fiber spinning results in bead formation [92]. Figure 21 shows a histogram of the diameter distribution of silica fibers electrospun from applied voltage of 10 kV, 15 kV and 20 kV. The result shows that fibers with applied voltage of 20 kV appeared non-uniform distribution of diameter. Accordingly, the most appropriated applied voltage to produce uniform, continuous and small diameter SF was 15 kV, giving the optimized condition of a 15 cm TCD and 15 kV applied voltage to produce continuous SF with a submicron diameter of 0.83 μm. Note that this simple and preliminary univariate approach ignores any possible interaction between these two variables and so the production of more optimal SF cannot be excluded.

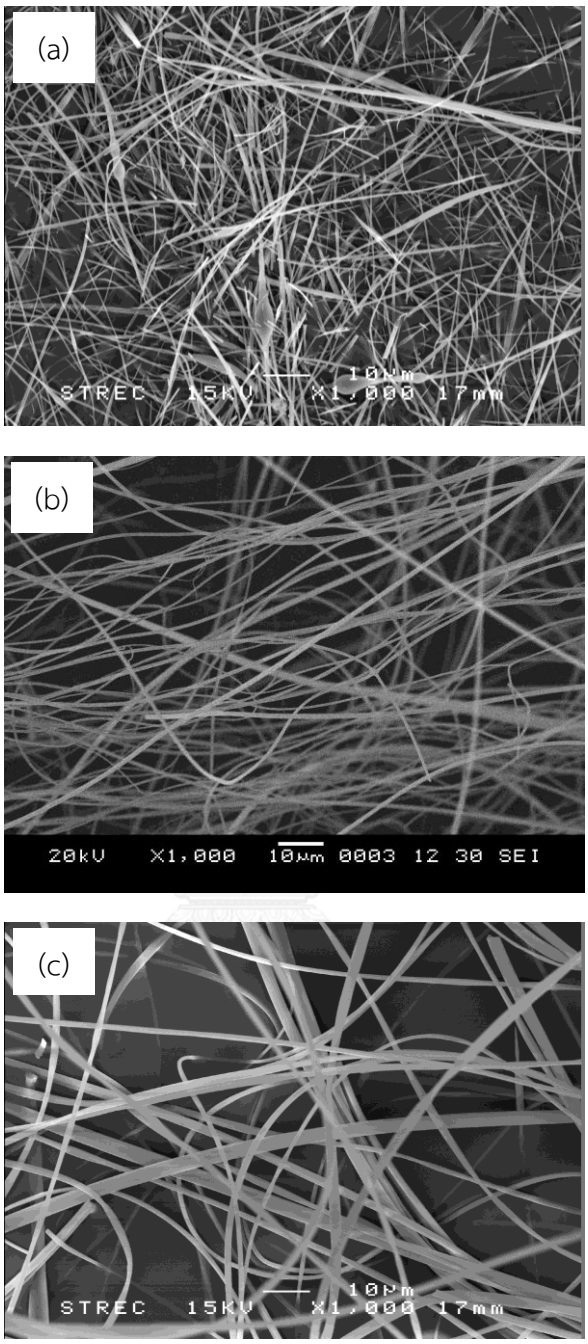

Figure 20 SEM images of the electrospun SF obtained with an applied voltage of (a) 10 kV, (b) 15 kV and (c) 20 kV at needle size = 0.25 cm and TCD = 15 cm.

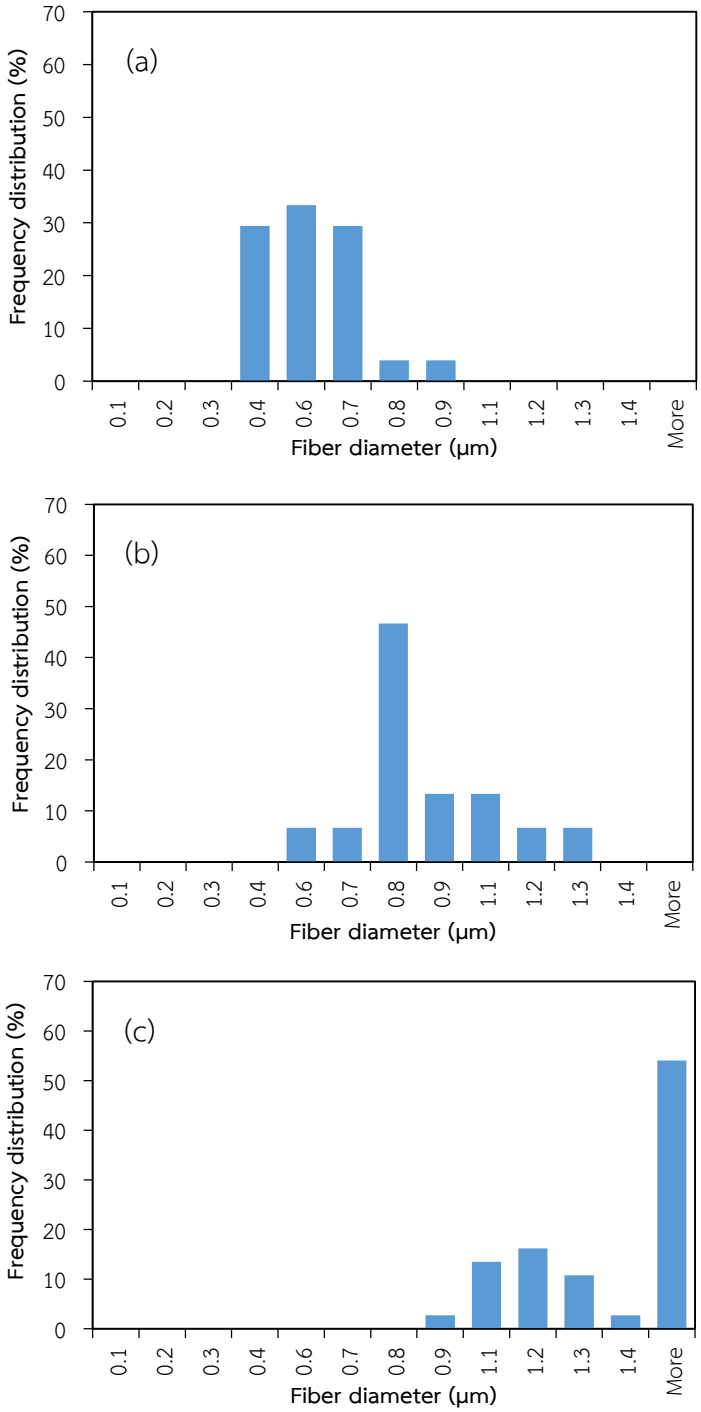

Figure 21 Diameter distribution of SF using different applied voltage: (a) 10 kV, (b) 15 kV and (c) 20 kV. The needle size and TCD were fixed at 0.25 cm and 15 cm, respectively.

4.2 Characterization of the ZSM-5/SF support

The SEM analysis revealed that the diameter of the SF ranged between 700 and 800 nm (Figure 22a). When modified by the *in situ* synthesis of ZSM-5, the SF did not significantly change in diameter (650 nm) but zeolite crystals were deposited along the surface of the SF (Figure 22b–d).

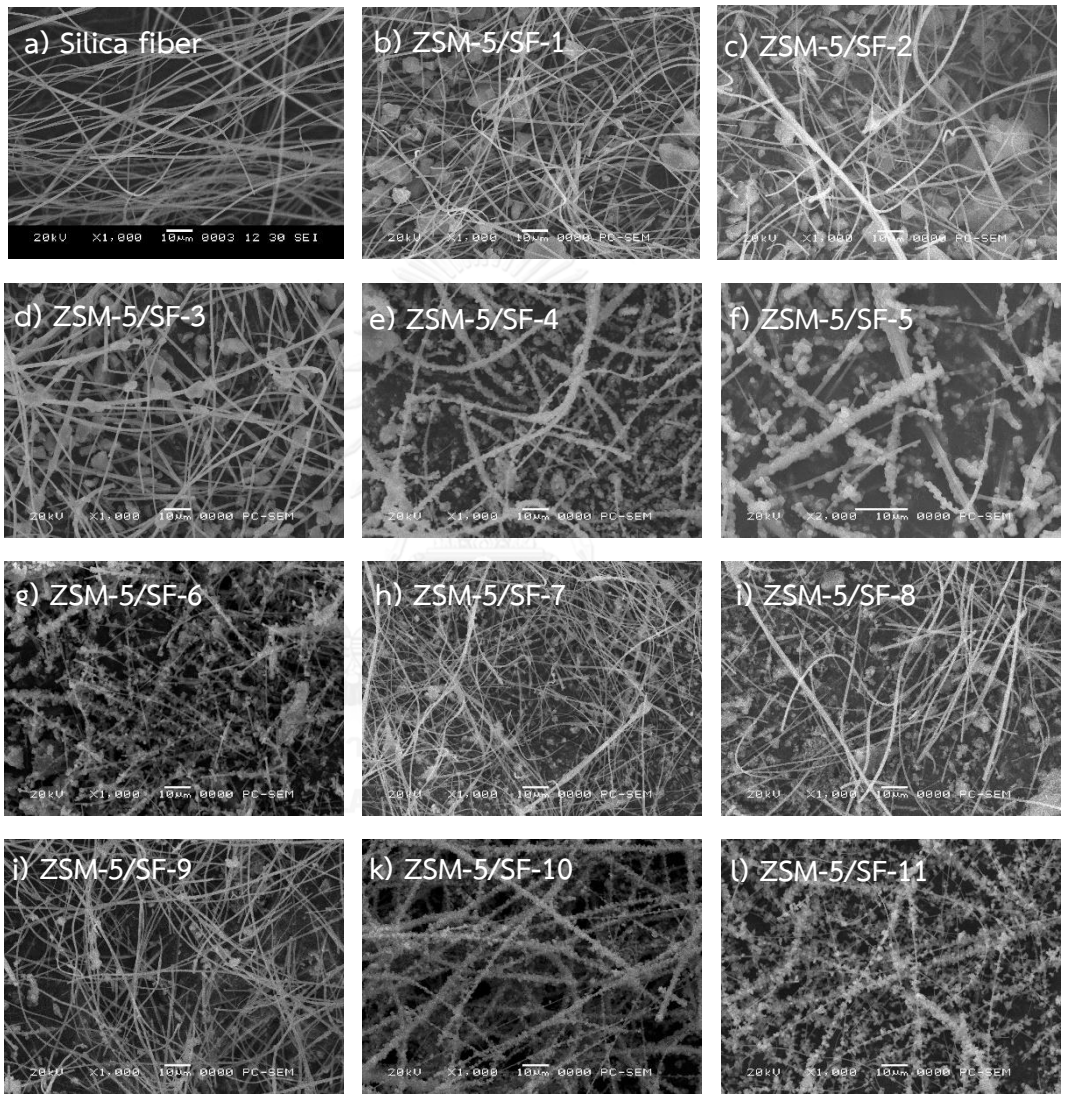

Figure 22 SEM images (1,000 x magnification) of the ZSM-5/SF obtained by the difference between their chemical compositions.

Table 5 Chemical compositions (molar ratio) and pH of reaction mixture for ZSM-5/SF

Samples	SiO_2	TPAOH	EtOH	H_2O	Al_2O_3	HNO_3	pH
ZSM-5/SF-1	1	0.24	0	25	0.025	0.120	7
ZSM-5/SF-2	1	0.24	0	25	0.025	0.038	8
ZSM-5/SF-3	1	0.24	0	25	0.025	0	9
ZSM-5/SF-4	1	0.24	0	25	0.010	0.038	10
ZSM-5/SF-5	1	0.24	0	40	0.010	0.038	10
ZSM-5/SF-6	1	0.24	4	25	0.010	0.038	10
ZSM-5/SF-7	1	0.24	8	25	0.010	0.038	10
ZSM-5/SF-8	0.8	0.24	0	25	0.010	0.038	10
ZSM-5/SF-9	0.6	0.24	0	25	0.010	0.038	10
ZSM-5/SF-10	1	0.24	0	25	0.006	0.038	10
ZSM-5/SF-11*	1	0.24	0	25	0.010	0.038	10

*SF are soaked in a 2M HNO_3 solution before placed in synthesis mixture.

The gel compositions and crystallization conditions for ZSM-5/SF synthesis are listed in Table 5. After hydrothermal treatment in zeolite synthesis solution at 170 °C for 24 h, ZSM-5/SF-1, 2 and 3 containing Al_2O_3 of 0.025 molar ratio and different HNO_3 contents did not presence of zeolite crystal growth on the silica fiber but the irregular shape particle appeared and separated from the fibers as show in the Figure 22 (ZSM-5/SF-1–3). The XRD patterns of ZSM-5/SF-1 and 3 (Figure 23) show a very low intensity peak and diffraction peaks are not present in XRD patterns of ZSM-5/SF-2 sample. Because zeolite was commonly synthesized in a highly basic medium in order to facilitate the dissolution of silicon precursors [73]. The synthesis mixtures of ZSM-5/SF-1–3 were consisted of high concentration of aluminium nitrate nonahydrate and pH values lower than 10 (Table 5). In acidic medium (pH $\leq$ 7), silica sources (TEOS) were hydrolyzed in cation form which did not stabilized by surface adsorbed TPA cations in the mixture [73]. Therefore, it could not build up MFI framework. The zeolite crystal was discovered at the pH of mixture larger than 10 (ZSM-5/SF-4–11 samples).

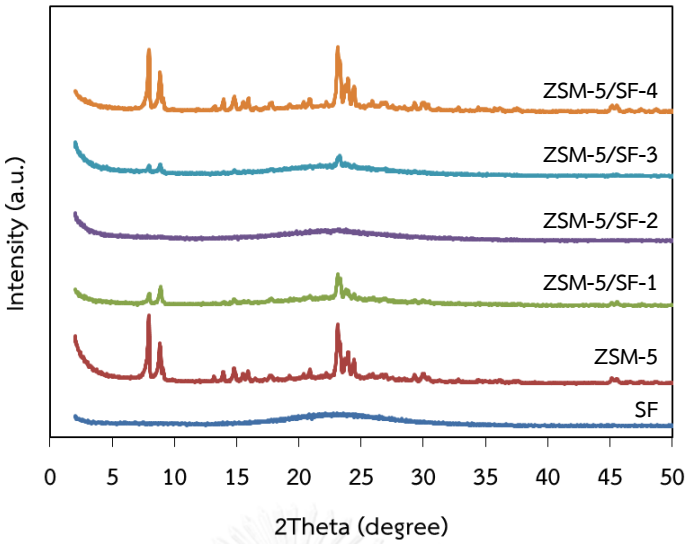

Figure 23 XRD pattern of silica fiber, ZSM-5 and ZSM-5/SF samples in different molar ratios of HNO_3

The influence of the ethanol addition was investigated for the molar ratio of $EtOH/SiO_2$ = 0, 4 and 8 (for ZSM-5/SF-4, 6 and 7, respectively). The results shows that when concentration of ethanol increased up to 8 molar ratio (ZSM-5/SF-7), the ZSM-5 particle do not deposited on the surface of SF. The XRD pattern of ZSM-5/SF samples prepared with $EtOH/SiO_2$ = 0, 4 and 8 (Figure 24a) show diffraction peaks of MFI zeolite. The nucleation and crystal growth steps were encouraged by ethanol in the gel composition.

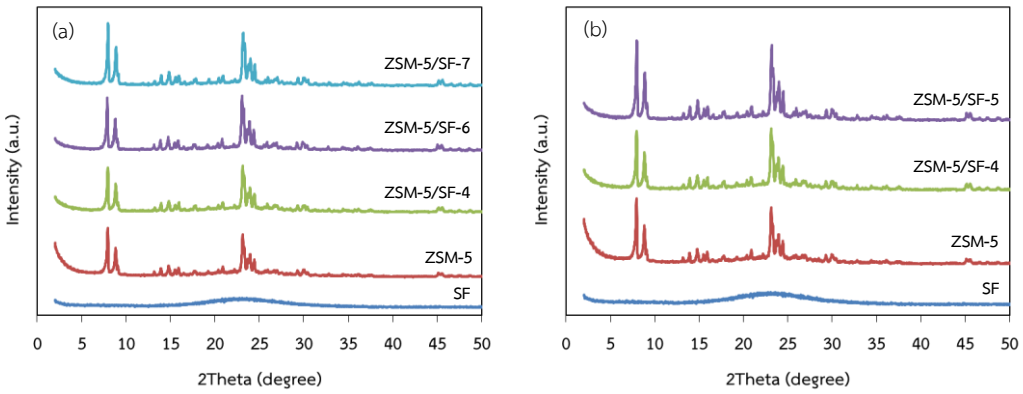

Figure 24 XRD pattern of silica fiber, ZSM-5 and ZSM-5/SF samples in different molar ratios of (a) EtOH and (b) water

For a low concentration of ethanol, the amount of ethanol is not enough to link together all the SiO_4 and AlO_4^- tetrahedra, the crystallization process being very slow. The sample prepared with EtOH/SiO_2 ratio of 8 presents intensity of XRD peak higher than those of the sample (Figure 24a). The intensity of XRD peaks of the product increase with the ethanol concentration. The excess of ethanol favors the intergrowth of the crystals to build large aggregates, increasing the average particle size.

The zeolite crystals deposited along the silica fiber for ZSM-5/SF-4 and 5 as show in Figure 22. The XRD pattern of these samples shows sharp and high-intensity peaks (Figure 24b). The higher pH induced significant increase in the crystal size probably due to the decrease in the incorporation of the Al at high pH and the role of these Al species in the nucleation process. The ZSM-5/SF-4 which was obtained at lower water content presented that more zeolite crystal deposited on silica fiber than higher water content (ZSM-5/SF-5) as show in Figure 26a and b. The higher water content induced faster hydrolysis rate to hinder zeolite crystal growth on the silica fiber. Water led higher induction times for nucleation and decreased the crystal growth rate. Iwasaki et al. [76] measured the growth rates at 150 °C of the (0 0 1), (1 0 0) and (0 1 0) crystal faces for values of H_2O/SiO_2 from 75 to 300 at final crystal lengths of 40 μm. The H_2O/SiO_2 ratio increased, rates progressively and the apparent activation energies in all directions decreased.

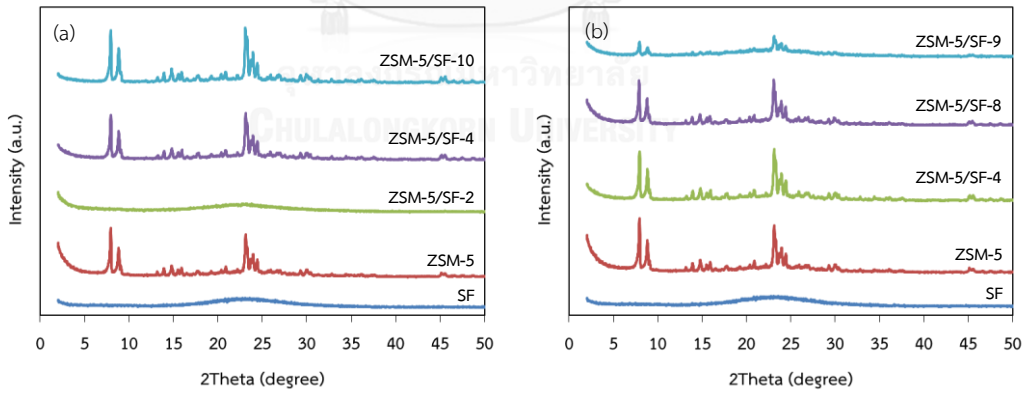

Figure 25 XRD pattern of silica fiber, ZSM-5 and ZSM-5/SF samples in different molar ratios of (a) Al_2O_3 and (b) SiO_2

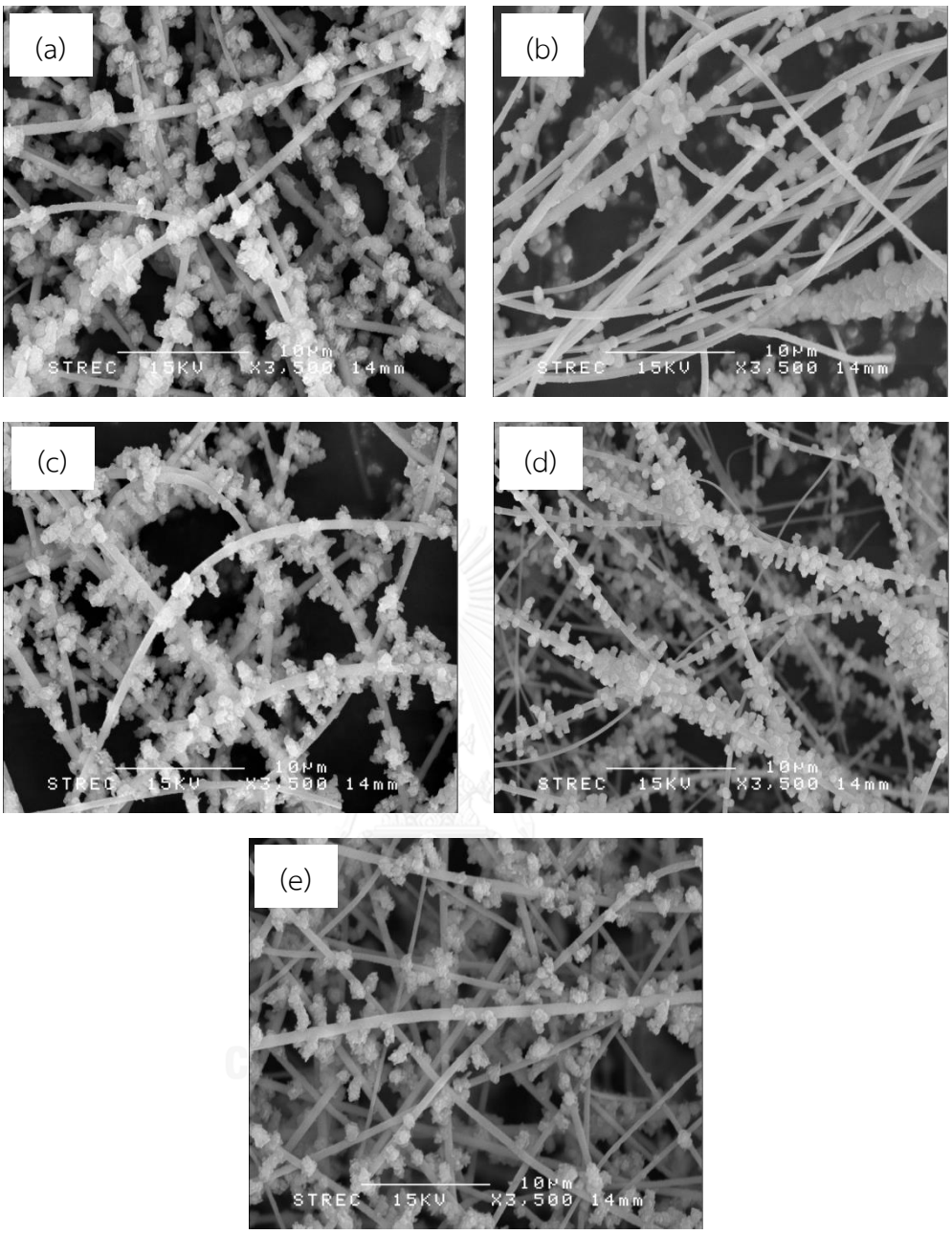

Figure 26 SEM images (3500 x magnification) of the ZSM-5/SF obtained by the difference between their chemical compositions: ZSM-5/SF-4 (a), ZSM-5/SF-5 (b), ZSM-5/SF-6 (c), ZSM-5/SF-10 (d) and ZSM-5/SF-11 (e).

The variation of the aluminum content presented an interesting effect on the crystallization of ZSM-5/SF samples. The XRD patterns of the samples prepared with Al_2O_3/SiO_2 ratio of 0.025, 0.010 and 0.006 are presented in Figure 25a. The intensity of MFI zeolite peaks increased with the decreasing Al_2O_3 content. A higher proportion of aluminum leads to longer induction times but accelerates the crystal growth rate. The

presence of aluminum seems to inhibit the formation of heteronuclei at the beginning of the crystallization. ZSM-5 particles deposited on surface of SF at Al_2O_3/SiO_2 ratio of 0.010 and 0.006, whereas the deposition of zeolite on SF surface does not occur at Al_2O_3/SiO_2 ratio of 0.025 (Figure 22). The SiO_2 contents were varied at 1, 0.8 and 0.6. When the silica content decreased to 0.8 and 0.6, the ZSM-5 particle do not deposited on the surface of SF, as shown in Figure 22i and j. The intensity of MFI zeolite peaks decreased with the decreasing SiO_2 content (Figure 25b).

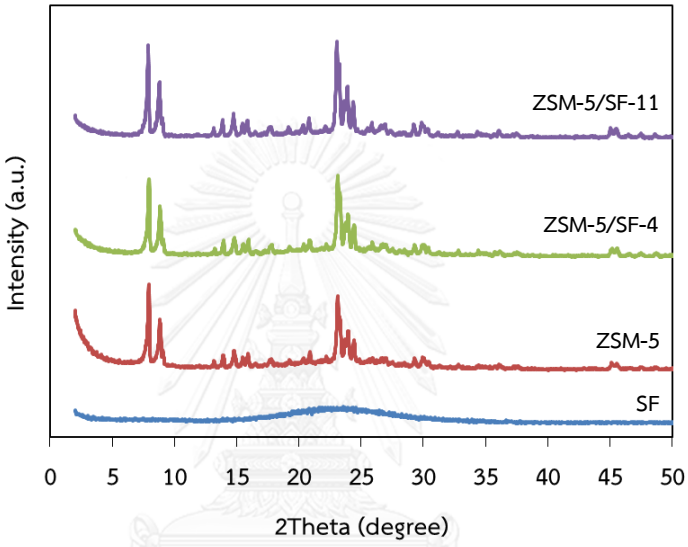

Figure 27 XRD pattern of silica fiber, ZSM-5, ZSM-5/SF-4 and ZSM-5/SF-11 samples

The ZSM-5/SF-11 sample, SF were pre-treatment by nitric acid solution before hydrothermal step, presented well crystalline peak of zeolite with MFI type and deposited ZSM-5 particle on surface of SF. From XRD (Figure 27) and SEM result, ZSM-5/SF-4, 5, 6, 10 and 11 showed that zeolite crystals were synthesized and deposited on some areas of the surface of the SF.

The representative SEM image of synthesis ZSM-5/SF-4, 5, 6, 10 and 11 at 3500x showed difference in the size and shape of the crystal depending on the composition of starting gel (Figure 26). The ZSM-5/SF-4, 6, and 11 led to non-uniform particles agglomerates and the grain size of ZSM-5 zeolite is in the range of 0.9–1.5 μm. The rough surface and the oval morphology of ZSM-5 are typical features of all samples crystallized in H_2O/SiO_2 = 25. The SEM image of ZSM-5/SF-4 was prepared with H_2O/SiO_2 = 40 is shown in Figure 23d. The single crystals are formed which exhibit smooth faces and cubic like structure and particles size of ZSM-5 are 0.82 μm. The water in ZSM-5/SF-5 decreased the size of ZSM-5 crystal. The H_2O/SiO_2 influences the rate and

crystallization mechanism in crystallization processes of zeolite. ZSM-5/SF-4 and 6 have similar shape of grain of ZSM-5, surface area and pore size distribution curve. Adding of ethanol to the synthesis mixture (ZSM-5/SF-6) presented good distribution of zeolite crystal along the silica fiber because ethanol reduced hydrolysis rate which the crystal can be generated on the surface of silica fiber (Figure 22e and f). Generally in sol–gel synthesis, solvents are added in order to facilitate mixing and to produce a more homogeneous sol. However solvents can also play a role in hydrolysis and condensation. Solvents may be polar (protic) or nonpolar (aprotic). The polarity of the solvent can influence the hydrolysis rate by increasing or decreasing catalytic activity. Solvents can also reduce reaction rates by simply diluting the sol, hence reducing the concentration of precursor.

Table 6 Specific surface area (S_{BET}), average pore diameter (dp_{av}) and pore volume (V_p) of the SF, ZSM-5, and ZSM-5/SF samples

Samples	S_{BET} (m^2/g)	dp_{av} (nm)	V_p (cm^3/g)
SF	20	-	-
ZSM-5	499	7.0	0.40
ZSM-5/SF-4	324	10.4	0.32
ZSM-5/SF-5	376	4.0	0.27
ZSM-5/SF-6	332	4.0	0.20
ZSM-5/SF-10	249	3.2	0.62
ZSM-5/SF-11	374	7.1	0.39

The treated of silica fiber by nitric acid presented the larger amount of zeolite crystal on silica fiber because the treatment of silica fiber with acid generate defect on the surface to enhance the crystal growth of zeolite (Figure 22i and j). For the samples prepared with a 0.006 mole ratio of Al_2O_3 (ZSM-5/SF-10), the particles exhibited a smooth surface with a cylindrical morphology. This reflects that the H_2O/SiO_2 ratio influences the rate and mechanism of the zeolite crystallization processes [31].

The textural properties, including the BET surface area, pore volume and average pore diameter of the samples are summarized in Table 6. The specific surface area of the ZSM-5 deposited on the SF (249–376 m^2/g) were much higher than that of the SF (20 m^2/g), whilst the surface area of the ZSM-5/SF-4–6, 10 and 11 were much lower than that of the ZSM-5, which reflects the dilution effect caused by the increasing proportion of the very low surface area SF. Nitrogen sorption isotherms of

SF, ZSM-5 and ZSM-5/SF samples were presented in Figure 28. ZSM-5 zeolite exhibits type IV adsorption isotherm, and a hysteresis is observed at a relative pressure range of 0.45 to 0.9 to refer the characteristic of meso-porosity. Whereas SF exhibited type III adsorption isotherm without hysteresis loops as characteristic of non-porous structure. ZSM-5/SF-4, 5, 6 and 11 show type II isotherm which was the combination between meso- and non-porous structures. The presence of a hysteresis loop at P/P_0 > 0.5 reveals the existence of mesopores of ZSM-5. ZSM-5/SF-10 exhibits type III adsorption isotherm whit hysteresis is observed at P/P_0 > 0.4.

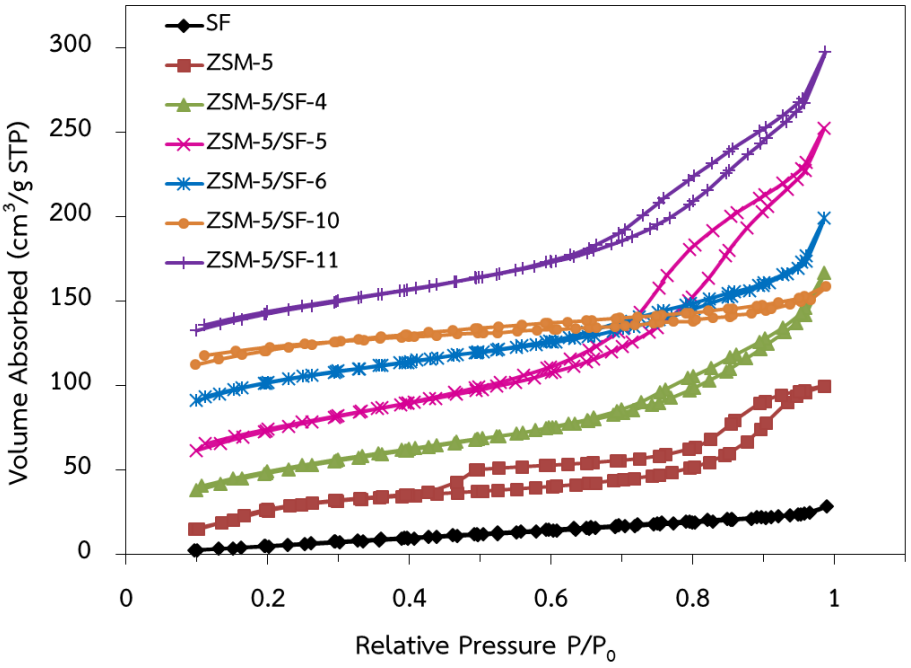

Figure 28 N_2 adsorption and desorption isotherms of silica fiber, ZSM-5 and ZSM-5/SF samples

The pore size distribution curves, as calculated using the BJH method, of ZSM-5 and the ZSM-5/SF-4–6, 10 and 11 reveal the narrower pore size distribution in the ZSM-5 than in the ZSM-5/SF samples (Figure 29). The ZSM-5/SF samples show a broadening pore size distribution and average pore diameter (from 6 to 10 nm). Thus, the dilution effect caused by increasing the proportion of the very low surface area SF also reduced the pore volume. The ZSM-5/SF-5 (40 mole ratio of H_2O) showed a sharper concentrated pore size distribution graph than that of the ZSM-5 modified SF, with the dominate pore size in the mesopore range occurring at ca. 8.8 nm (Figure 29). This may result from the fact that in hydrothermal systems, the high solvent power of

water promotes the mixing and transport of materials and facilitates the nucleation and growth of the crystals [31, 82]. Water stabilizes the zeolite structures by filling the cavities and forming a type of solid solution that results in a more uniform pore size and high surface area (376 m^2/g) of the sample. These results revealed that ZSM-5 can deposit on the surface of the SF and improve their total surface area.

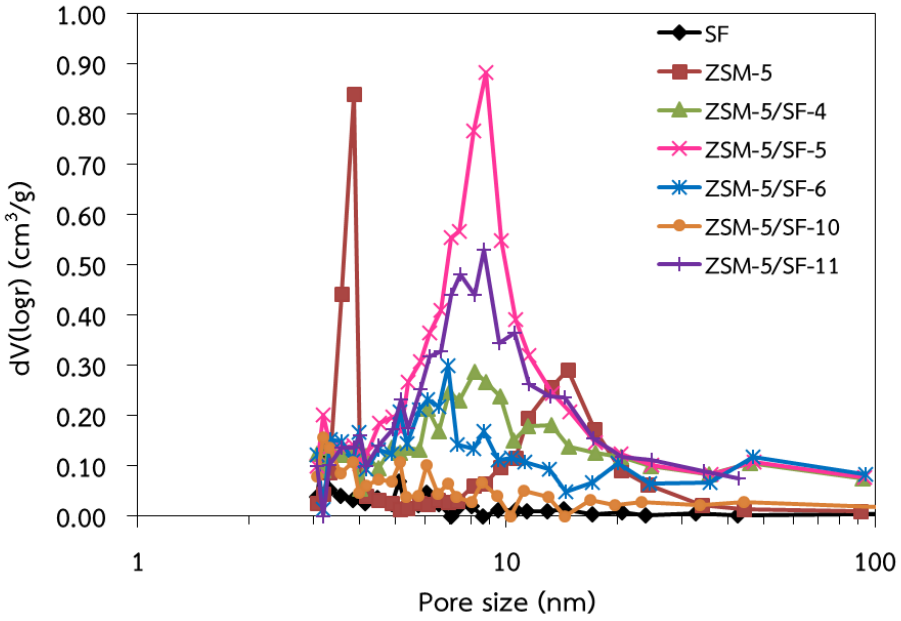

Figure 29 BJH pore size distribution of silica fiber, ZSM-5 and ZSM-5/SF samples

TPD was carried out to evaluate the acidic properties of the catalyst. The NH_3-TPD patterns of the ZSM-5 deposited on silica fiber are shown in Figure 30 and there are three ranges of ammonia desorption: weak, intermediate and strong. If desorption peak area is large then the number of acid sites is high. Several desorption peaks existed in all samples. Normally, strength of solid acid sites within TPD profiles can be classified by the temperature of desorption of NH_3 as weak (120–300 °C), moderate (300–500 °C) and strong (500–650 °C)

From Figure 30, it can be observed that all ZSM-5/SF samples displayed a major desorption peak around 120 °C, an indication of the weak acid sites form surface hydroxyl group from ZSM-5 [73]. The concentration of these sites was considered to be not catalytically important, but it is assumed to effectively influence the proton mobility in zeolites [77]. The second peak in the rank of 300-500 °C corresponds to strong Brønsted acid sites. All ZSM-5/SF samples exhibit peak at 333 °C and this peak is closely related to surface acid properties. The commercial ZSM-5 shows two mains

desorption peak at 147 and 334 °C and these peaks present a higher intensity than that of ZSM-5/SF sample. Compared with commercial ZSM-5, the first and second peak of SF after modified by ZSM-5 shifted to lower temperature due to the combination of low-acidity and acidity property of materials whereas SF sample shows board peak at 250 °C. This implies that the acidity of ZSM-5/SF solids is weaker than conventional ZSM-5, but stronger than SF.

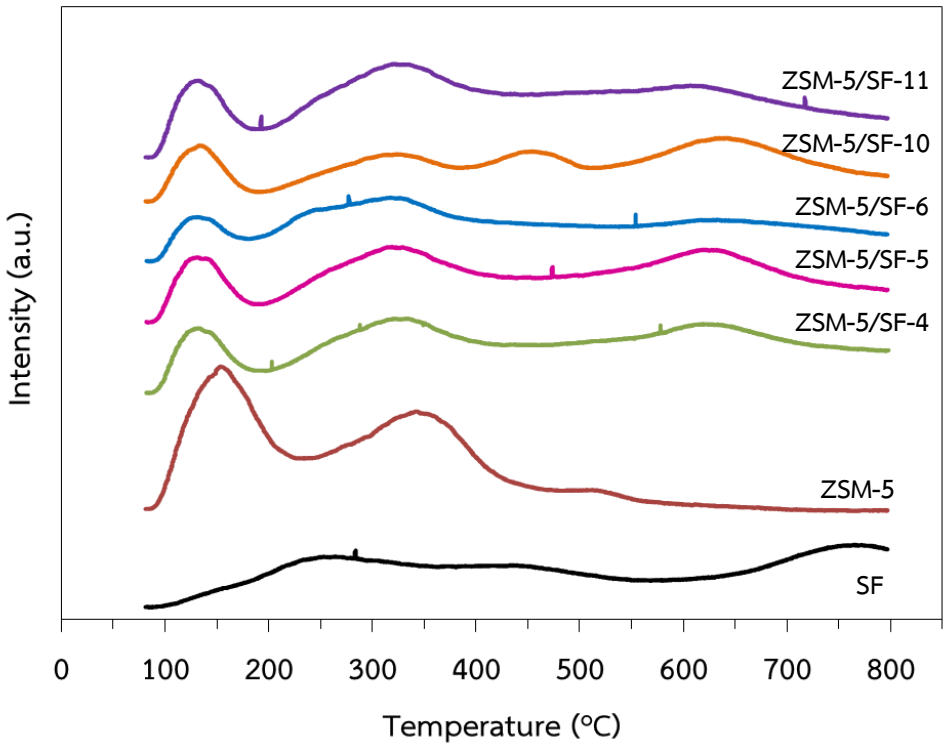

Figure 30 TPD profiles of the SF, ZSM-5 and ZSM-5/SF samples

4.3 Characterization of the Co/ZSM-5/SF catalysts

The XRD patterns of the calcined catalysts with 10 wt% Co revealed peaks attributable to the spinel Co_3O_4 in all samples (Figure 31). The particle size of Co_3O_4 was calculated using the Scherrer's equation and the obtained average Co_3O_4 crystallite sizes are listed in Table 7. The crystallite size of Co_3O_4 increased as the surface area of the support was decreased, and the Co/SF, Co/ZSM-5 and Co/ZSM-5/SF catalysts had a lower BET surface area than the support, which is attributed to a clogging or covering of the support pore by the loaded Co_3O_4. The ZSM-5/SF-10 presented the largest cobalt particle size (19 nm) due to large surface area of support.

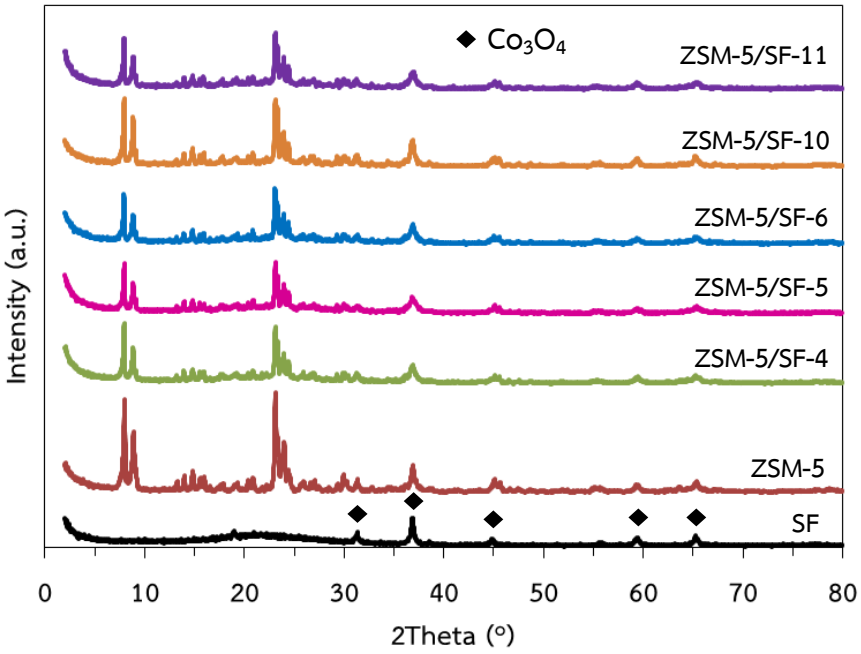

Figure 31 XRD pattern of Co/SF, Co/ZSM-5 and Co/ZSM-5/SF catalysts

Table 7 Specific surface area (S_{BET}), average pore diameter (dp_{av}) and pore volume (V_p) of the Co/ZSM-5/SF catalyst, cobalt content and Co_3O_4 crystallite sizes (d_{Co3O4}) of catalysts

Samples	S_{BET} (m^2/g)	dp_{av} (nm)	V_p (cm^3/g)	Co content[a] (%)	d_{Co3O4}[b] (nm)
Co/SF	15	-	-	12.4	21.5
Co/ZSM-5	339	7.0	0.24	11.0	10.9
Co/ZSM-5/SF-4	236	6.2	0.19	11.9	14.9
Co/ZSM-5/SF-5	223	3.2	0.20	11.7	11.4
Co/ZSM-5/SF-6	235	5.2	0.19	12.8	15.2
Co/ZSM-5/SF-10	191	3.2	0.08	12.9	18.9
Co/ZSM-5/SF-11	241	3.9	0.22	11.7	13.4

[a] Co content was measured by the EDX technique.

[b] The crystallite size of Co_3O_4 was calculated using Scherrer's equation.

The TPR analysis was performed to determine the reducibility of the surface Co_3O_4 species, where the TPR profiles of the supported cobalt oxide particles on the different SF supports revealed two main reduction peaks (Figure 32). These correspond to the CoO (peak I) and Co^0 (peak II) from the reduction of Co_3O_4 in the two steps of

$Co_3O_4 \longrightarrow CoO$ and $CoO \longrightarrow Co^0$. The Co/SF catalyst showed these two peaks at a lower temperature with a shoulder around 253 ℃ and an intense peak II at 282 ℃. The addition of ZSM-5 to the SF did not significantly affect the reducibility, although there was a slight shift to higher temperatures (269–286 °C and 303–328 °C for peak I and peak II, respectively). The ZSM-5 support is known to generate a strong Co-support interaction on the acidic sites of ZSM-5 [41]. Moreover, the intensities of the corresponding peaks in the modified and unmodified support catalysts were distinctly different. Besides a slight difference in peak I, the intensity of peak II decreased after the addition of ZSM-5 to the SF support, indicating that the Co–support interaction increased. The Co/ZSM-5/SF-5 catalyst showed the lowest relative int ensity of peak II, suggesting a lower degree of reduction of CoO to metallic Co with the larger surface area and smaller crystallite size of Co species.

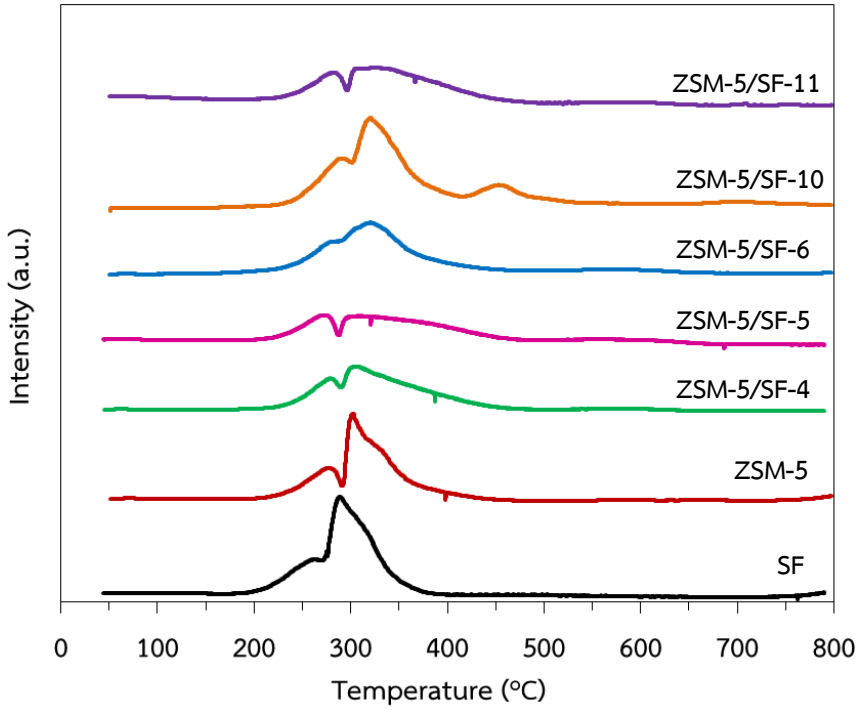

Figure 32 H_2-TPR profiles of the Co/SF, Co/ZSM-5 and Co/ZSM-5/SF catalysts.

The NH_3-TPD patterns of the Co/ZSM-5/SF catalysts showed a two stage desorption of NH_3 (Figure 33). All the catalysts had an almost similar peak in this 300–500 ℃ range. The number of weak and strong acid sites is summarized in Table 8, expressed as mmol NH_3/g of catalysts, where the acid site density was found to be higher on the Co/ZSM-5 catalyst, which is due to it having the lowest SiO_2/Al_2O_3 molar

ratio. From Table 8, the total number of acid sites varies in the order of ZSM-5/SF-11 > ZSM-5/SF-6 > ZSM-5/SF-5 > ZSM-5/SF-4 > ZSM-5/SF-10. The acidity enhanced by decrease of SiO_2/Al_2O_3 ratio. In addition, the variation of acidity can be further related to the hydrocarbon selectivity of Co/ZSM-5/SF catalysts.

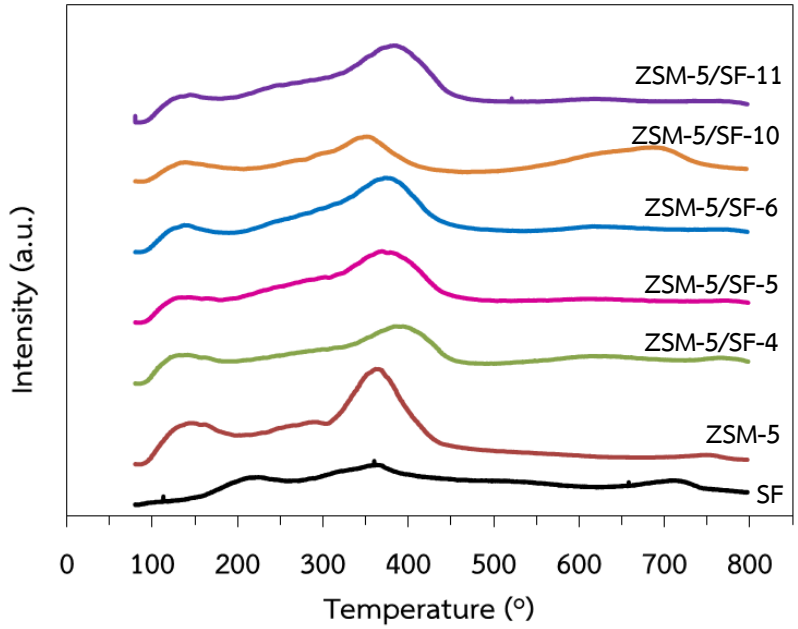

Figure 33 NH_3-TPD profiles of the Co/SF, Co/ZSM-5 and Co/ZSM-5/SF catalysts.

Table 8 Surface acidity of the Co/ZSM-5/SF catalysts, as measured by NH_3-TPD

Samples	SiO_2/Al_2O_3 ratio of support	Acidic sites (mmol NH_3/g)		
		Weak[a]	Strong[b]	Total
Co/SF	-	0.014	0.043	0.057
Co/ZSM-5	83.7	0.145	0.496	0.641
Co/ZSM-5/SF-4	110.6	0.022	0.071	0.093
Co/ZSM-5/SF-5	119.0	0.019	0.090	0.109
Co/ZSM-5/SF-6	96.6	0.016	0.103	0.119
Co/ZSM-5/SF-10	135.7	0.015	0.065	0.080
Co/ZSM-5/SF-11	93.8	0.093	0.103	0.196

Acid sites were categorized as [a]weak ($T_{desorp.}$ < 300 °C) or [b]strong (300 °C < $T_{desorp.}$ < 500 °C).

4.4 Characterization of the composite Co, ZSM-5 and SF catalysts

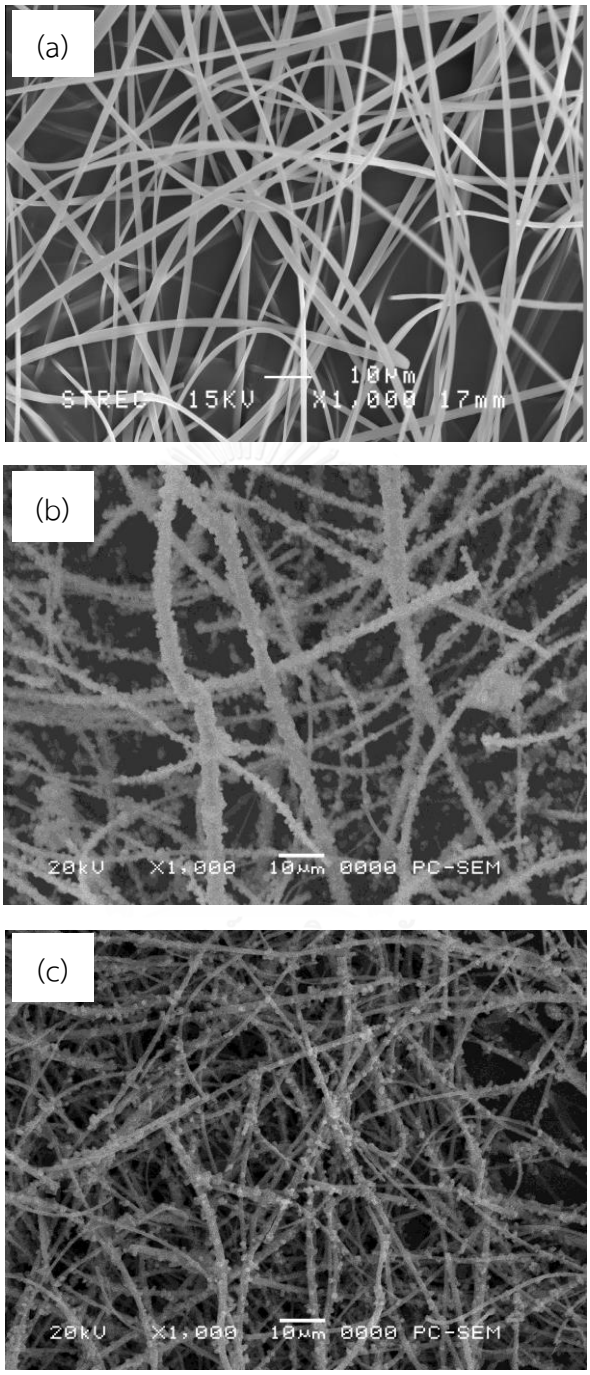

Figure 34 SEM images of the (a) SF, (b) ZSM-5/SF and (c) ZSM-5/Co/SF.

The SEM image of the SF showed a smooth surface morphology, but once hydrothermally treated with the synthesis solution of ZSM-5 the obtained ZSM-5/SF showed a crystal material deposited on the SF surface (Figure 34). The deposition of

the zeolite (ZSM-5) on the Co/SF catalyst resulted in ZSM-5 microparticles being clearly seen to have grown on the surface of the SF (Figure 34c). The XRD patterns of the SF were amorphorous, whilst that for the SF modified by ZSM-5 revealed well crystallized materials (Figure 35).

The textural properties of the BET surface area, pore volume and average pore diameter of the samples are summarized in Table 9. The specific surface area of ZSM-5/SF (324 m^2/g) was markedly (16.2-fold) higher than that of SF, but lower (1.5-fold) than that for ZSM-5. The Co/SF, Co/ZSM-5 and Co/ZSM-5/SF catalysts had a lower BET surface area than the respective support, which is attributed to the clogging or covering of the support pores by the loaded Co_3O_4 particles. Deposition of ZSM-5 onto the Co/SF catalyst increased its specific BET surface area 11.9-fold to 238 m^2/g, which is essentially the same surface area as that for Co/ZSM-5/SF. These results revealed that ZSM-5 can grow on the surface of the SF and Co/SF catalyst and improve their total surface area.

Table 9 Specific surface area (S_{BET}), average pore diameter (dp_{av}) and pore volume (V_p) of the composite cobalt catalyst

Samples	S_{BET} (m^2/g)	dp_{av} (nm)	V_p (cm^3/g)
SF	20	1.6	0.02
ZSM-5	499	3.5	0.40
ZSM-5/SF	324	5.2	0.32
Co/SF	15	1.6	0.05
Co/ZSM-5	339	3.5	0.24
Co/ZSM-5/SF	236	3.1	0.19
ZSM-5/Co/SF	238	4.4	0.29
Co/SF+ZSM-5	260	3.1	0.26

The XRD patterns of the cobalt based catalysts revealed the diffraction peaks of the spinel Co_3O_4 phase at 2θ = 19.0°, 31.3°, 37.0°, 59.5° and 65.4° (Figure 35), which correspond to the (111), (220), (311), (511) and (440) crystal faces, respectively. The crystallite particle sizes of Co_3O_4 in these composite cobalt catalysts are summarized in Table 10. The crystallite sizes of Co_3O_4 varies in the order of Co/SF = Co/SF+ZSM-5 > Co/ZSM-5/SF > Co/ZSM-5 > ZSM-5/Co/SF. The Co/SF had the largest Co_3O_4 particle size at some 2.0- and 2.8-fold larger than in the Co/ZSM-5/SF and Co/ZSM-5 catalysts, respectively. The larger size partially reflects the very low surface area of the SF

support and the small pore size. Furthermore, the interaction between SF and cobalt species has been described as relatively weak, which is considered to be better for cobalt ion reducibility and large cobalt particle size formation [24]. Due to large size of the formed particles, cobalt dispersion is usually much lower in a silica-supported cobalt-based catalyst than that of an alumina-supported cobalt-based catalyst [22]. However, larger Co_3O_4 crystallites were previously detected in catalysts prepared from supports with wider pores. For example, the modification of mesoporous silica by cobalt via aqueous impregnation resulted in small Co_3O_4 crystallites located in the silica pores and the size of these crystallites increased with increasing mesopore diameters [1]. In this study the particle sizes of Co_3O_4 were quite similar for the Co/SF and Co/SF+ZSM-5 samples, but slightly larger in the ZSM-5/Co/SF one. This apparent contradiction likely reflects that the higher calcination temperature (550 °C) in the ZSM-5 deposition step is likely to have resulted in the sintering and agglomeration of the cobalt particles [53].

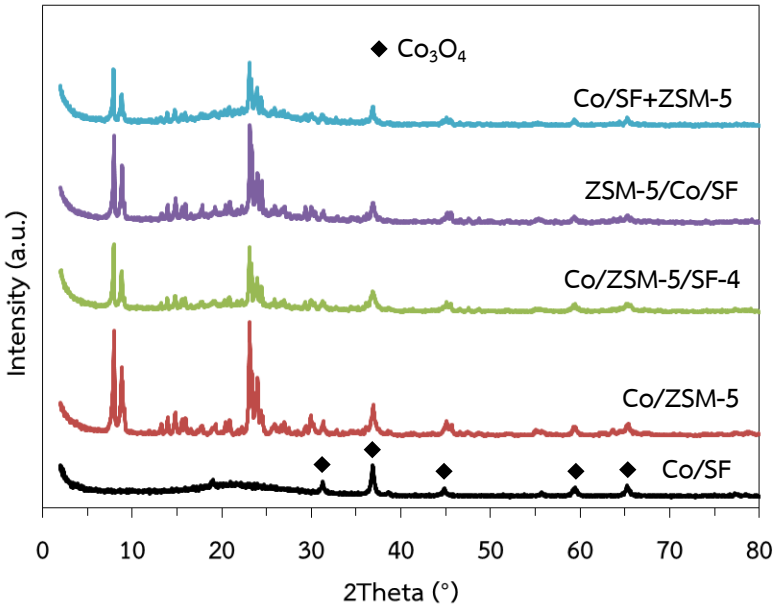

Figure 35 XRD patterns of the composite cobalt catalysts

Table 10 The physico-chemical properties of the composite cobalt catalysts

Catalyst	Co content[a] (%)	Co_2O_3 particle size[b] (nm)	Reduction temperature (°C)	
			Peak I	Peak II
Co/SF	12.4	30.4	253	282
Co/ZSM-5	11.0	10.9	270	306
Co/ZSM-5/SF	11.9	14.9	272	306
ZSM-5/Co/SF	6.4	32.4	315	339
Co/SF+ZSM-5	12.4	30.4	318	343

[a] Co content was measured by the EDX technique.

[b] The crystallite size of Co_3O_4 was calculated using Scherrer's equation.

To determine the reducibility of the surface Co_3O_4 species, H_2-TPR analysis was performed. All the catalysts exhibited two main reduction peaks (Figure 36), which correspond to the reduction of Co_3O_4 in the two steps of: $Co_3O_4 \longrightarrow CoO$ (peak I) and $CoO \longrightarrow Co^0$ (peak II). The reduction behavior of the ZSM-5/Co/SF catalyst was compared with that of the physically mixed Co/SF and ZSM-5 sample (Co/SF+ZSM-5). The H_2-TPR profile of the ZSM-5/Co/SF sample had two peaks at around 315 and 339 °C, consistent with the reduction behavior of the Co/SF catalyst. The H_2-TPR profiles of ZSM-5/Co/SF and Co/SF+ZSM-5 were shifted towards higher temperatures than that in the H_2-TPR profile of the Co/SF catalyst. This indicated that they are less easily reduced than the composite catalyst. These results are likely to be due to the larger cobalt particles and weaker interaction between silica and cobalt particles.

To evaluate the acidic properties of the catalyst, NH_3-TPD was performed and representative patterns of the Co/ZSM-5/SF catalysts are shown in Figure 37, where a two stage desorption of NH_3 was clearly observed. The number of acid sites (as mmol NH_3/g of catalyst), in terms of only weak and strong acidic sites, is shown in Table 11. The composite catalysts showed a similar desorption peak to the Co/ZSM-5 catalyst below 230 °C, as well as a weaker but slightly different peak at over 300 °C (Figure 4.19), indicating that the zeolite hybrid catalysts provided weaker acid sites than Co/ZSM-5 catalyst (Table 11). The composite catalysts also had a lower net ammonia uptake than the Co/ZSM-5 catalyst (Table 11). That the composite catalysts had a slightly lower total number of acid sites is because of their lower ZSM-5 zeolite loading amounts.

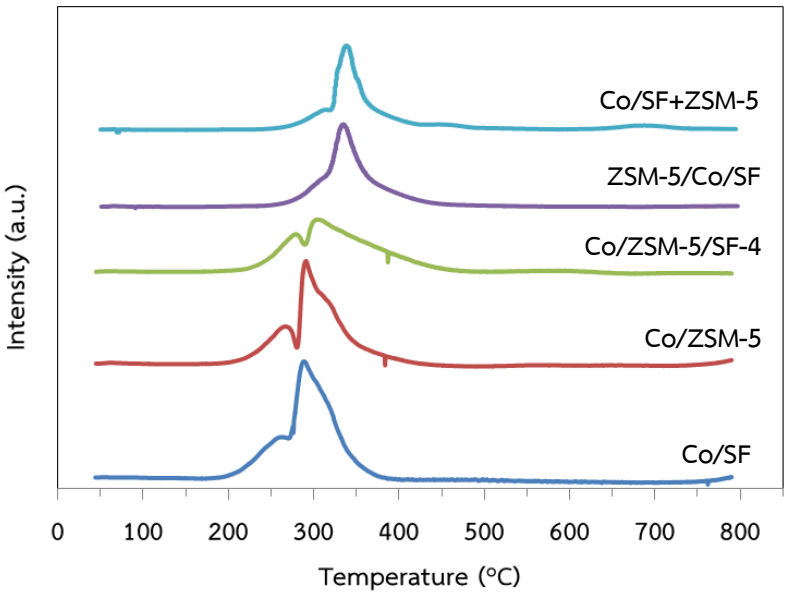

Figure 36 H_2-TPR profiles of the composite cobalt catalysts

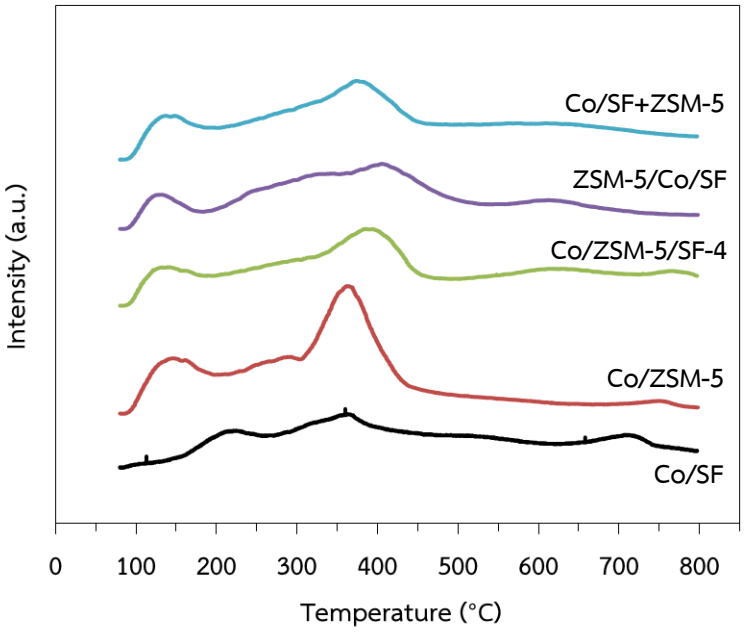

Figure 37 NH_3-TPD profiles of the composite cobalt catalysts

Table 11 Surface acidity of the composite cobalt catalysts, as measured by NH_3-TPD

Sample	Acidic site (mmol NH_3/g)		
	First peak ($T_{desorp.}$ < 300 °C)	Second peak (300 °C < $T_{desorp.}$ < 500 °C)	Total
Co/ZSM-5	0.035	0.094	0.129
Co/ZSM-5/SF	0.022	0.071	0.093
ZSM-5/Co/SF	0.016	0.059	0.075
Co/SF+ZSM-5	0.025	0.067	0.092

4.5 Characterization of the Co/SF catalysts prepared by different methods

The structural and textural properties of the different Co/SF catalysts prepared by the different methods are summarized in Table 12. The Co/SF catalyst prepared by impregnation method had the lowest BET surface area of all the catalysts and was slightly higher (1.04-fold) than the SF support, which is attributed to the Co_3O_4 particles covering the SF surface. The CO/SF catalyst had the lowest surface area because the cobalt species can easily migrate and accumulate during the thermal treatment of the wet sample. For the Co/SF-SEA, Co/SF-DPNa, Co/SF-DPNH and Co/SF-HT catalysts, the BET specific surface area was increased significantly (1.8-, 1.49-, 2.02- and 4.34-fold, respectively) compared to the SF support. That Co/SF-SEA catalyst had high surface areas (up to 37.5 m^2/g) is because the SEA method yields highly dispersed cobalt on the support surface [69]. The increasing of surface area of DP catalysts may be because amount of layered cobalt compounds formed and deposited on support's surface. According to Burattin et al. [56], the surface area of Ni supported on porous Spherosil silicas (S_{BET} = 44 m^2/g) increases with deposition-precipitation time. The new surface areas were developed by their disordered stacking of nickel compound. That the BET surface area of the Co/SF-DPNH catalyst was larger than that of the Co/SF-DPNa catalyst is because sodium acts as a sintering agent even at a very low concentrations [103].

Table 12 Average BET surface area and Co_3O_4 level in the Co/SF catalysts prepared by different methods

Sample	Surface area (m^2/g)	Amount of Co_3O_4 (wt%)
SF	20.8	-
Co/SF	15.0	12.4
Co/SF-SEA	37.5	15.0
Co/SF-DPNa	31.0	9.9
Co/SF-DPNH	42.1	9.7
Co/SF-HT	50.4	8.0

The XRD patterns of the unreduced catalysts all showed diffraction peaks, which indicated the presence of Co_3O_4, and a broad peak at 22.5° that was attributed to amorphous SiO_2 (Figure 38). Much broader XRD peaks were observed in the Co/SF-HT catalyst, which indicated a smaller Co_3O_4 crystallite size and the formation of cobalt silicate. Furthermore, the cobalt loading level was only 8.0 wt% (Table 12), and so the increasing the temperature to 140 °C for 24 h in the synthesis process decreased the amount of cobalt species on the SF surface due to the exothermic nature of the adsorption process [106].

Table 13 Characterization of the Co/SF catalysts prepared by different methods

Samples	Co_3O_4 crystallite diameter (nm)		H_2 Co (nm)	H_2 uptake ($\mu mol_{H2}/g_{cat}$)	Co dispersion[b] (%)
	XRD[a]	TEM			
Co/SF	30	27.6	368.6	2.3	0.3
Co/SF-SEA	9	10.2	95.0	8.9	1.0
Co/SF-DPNa	14	14.8	83.1	10.2	1.2
Co/SF-DPNH	12	11.6	14.8	57.2	6.7
Co/SF-HT	4	3.8	66.3	12.7	1.5

[a] Calculated by Scherrer formula.

[b] Determined by H_2 chemisorption.

The crystallite sizes of Co_3O_4 in the Co/SF catalysts, as calculated from the Co_3O_4 (311) diffraction peak using the Scherrer equation, are summarized in Table 13. The crystallite size of Co_3O_4 in the Co/SF catalysts was the largest, followed by that in the Co/SF-DPNa, Co/SF-DPNH, Co/SF-SEA and Co/SF-HT catalysts at 2.14-, 2.5-, 3.3- and

7.5-fold smaller, respectively. That the Co_3O_4 crystalline size of the Co/SF catalyst was the largest is due to the relatively weak interaction between the $Co^{2+}$and the SF in the impregnation process that allowed their redistribution during the drying and calcination stages to form cobalt oxide aggregates on the support. In addition, the pH of the Co^{2+} precursor solution could affect the size of the obtained cobalt oxide particles on the support [1]. Porous oxides, such as alumina, silica and titania, have different PZC values. At a solution pH higher than the PZC, the surface of the support is negatively charged and the Co^{2+} cations are distributed homogenously. Increasing the pH further can lead to dissolution of the support in the impregnating solution. It has recently been reported that the physical and chemical properties of cobalt species on the silica gel surface were strongly affected by the pH. At pH < 5 the cobalt deposited as a cation and at a pH < 2 the positively charged silica surface dispersed the cobalt and consequently a poor catalytic activity was obtained, whereas at a pH > 5 the cobalt was irreducible due to forming silicates or hydrosilicates [69].

The chemisorption of pure hydrogen on the Co/SF catalysts was compared in Table 13. The Co/SF catalyst showed the lowest of Co dispersion, while SEA and DP method enhanced the dispersion of Co up to 1.7%. This may be because the cobalt species were migrated and accumulated during the thermal treatment when catalysts were prepared by IM method. The Co/SF-SEA and Co/SF-DP catalysts had higher specific surface area and smaller Co_3O_4 particle size than that of Co/SF catalyst; therefore, Co/SF-SEA and Co/SF-DP catalysts showed high the dispersion of catalysts.

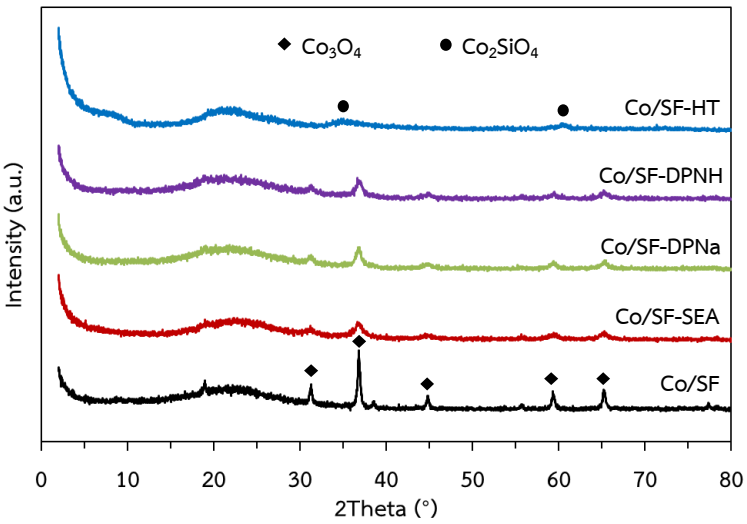

Figure 38 XRD patterns of the Co/SF catalysts prepared by different methods

Figure 40 displayed the TEM images of the calcined catalyst Co/SF, Co/SF-SEA, Co/SF-DPNa, Co/SF-DPNH, and Co/SF-HT respectively. The TEM image of the fresh catalyst reveals cobalt particle decoration of the silica support, and sizes of Co_3O_4 was affected by the preparation method. As compared in Figure 4b and c, when the SEA method was used to prepare supported catalysts, the particle-size was rather smaller with the average sizes 10.2 nm. The average sizes of the Co_3O_4 crystalline measured from TEM images were shown in Table 13. It was clear that the average size of Co_3O_4 crystalline obeyed the series: HT < SEA < DPNH < DPNa << IM, which was in accordance with the results of XRD analysis in Figure 35 and Table 12.

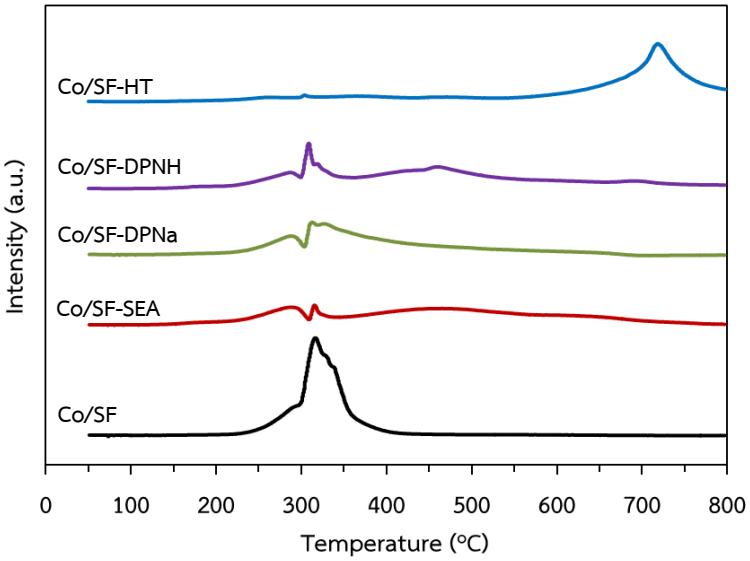

Figure 39 H_2-TPR profiles of the Co/SF catalysts prepared by different methods

The reduction behaviour of the Co/SF catalysts was investigated by H_2-TPR, where catalysts containing Co_3O_4 species present a two step reduction profile of Co_3O_4 to CoO and then to Co^0, and where the intensity of peak I is usually lower than that of peak II when the Co_3O_4 particles are of a small size [8]. For all the Co/SF catalysts produced in this study except for Co/SF-HT these two main reduction peaks were observed as two broad reduction features at 380–530 °C and 580–780 °C that depended on the degree of interaction between the Co species and SF support, as shown in Figure 39. The Co/SF catalyst showed a weak interaction between the cobalt species and the SF support; therefore, cobalt oxide can be easily reduced. The H_2-TPR profile of the Co/SF-HT catalyst, however, did not present any reduction peak below 400 °C, and a broad peak appeared at 660 °C that was assigned to the reduction of cobalt silicate [8, 63]. It was previously reported that the formation of barely reducible

surface and bulk Co silicate species was found in 10 wt% Co/ITQ-2 (a pure silica zeolite) catalysts with a d(Co_3O_4) ≤ 5.9 nm [107]. The TPR profile of Co/SF-SEA catalyst also shows two reduction peaks and a broad peak appeared at 463 °C, suggesting that the presence of degrees of interaction between Co species and the support might be different from that of Co/SF catalyst. SEA technique can be created by the electrostatic adsorption mechanism and synthesized highly dispersed metals on simple supports. Furthermore, the Co/SF-DPNa and Co/SF-DPNH catalysts show the two distinct reduction peaks at much lower temperature at 295 and 309 °C. The peak at 463 °C in Co/SF-DPNH sample corresponds to small crystallite size of cobalt oxide and strongly cobalt–support interaction.

From TEM image of Co/SF-HT catalyst (Figure 40e), the catalyst contained a needle-like phase and rounded cobalt particles are not observed (compare Figures 4.21a and e). In catalyst preparation procedure, the 140 °C hydrothermal treatment in aqueous solution applied before the calcination of catalyst and induced mixed oxide of metal and support formation. Effect of water on silica-supported cobalt catalyst, which may affect the interaction with water, was considered by many researchers [108, 109]. The deactivation of silica-supported cobalt catalysts resulted from cobalt-silica mixed oxide formation which was induced by hydrothermal conditions and presented needle-like morphology; moreover, water is an agent inducing mixed oxide formation [109].

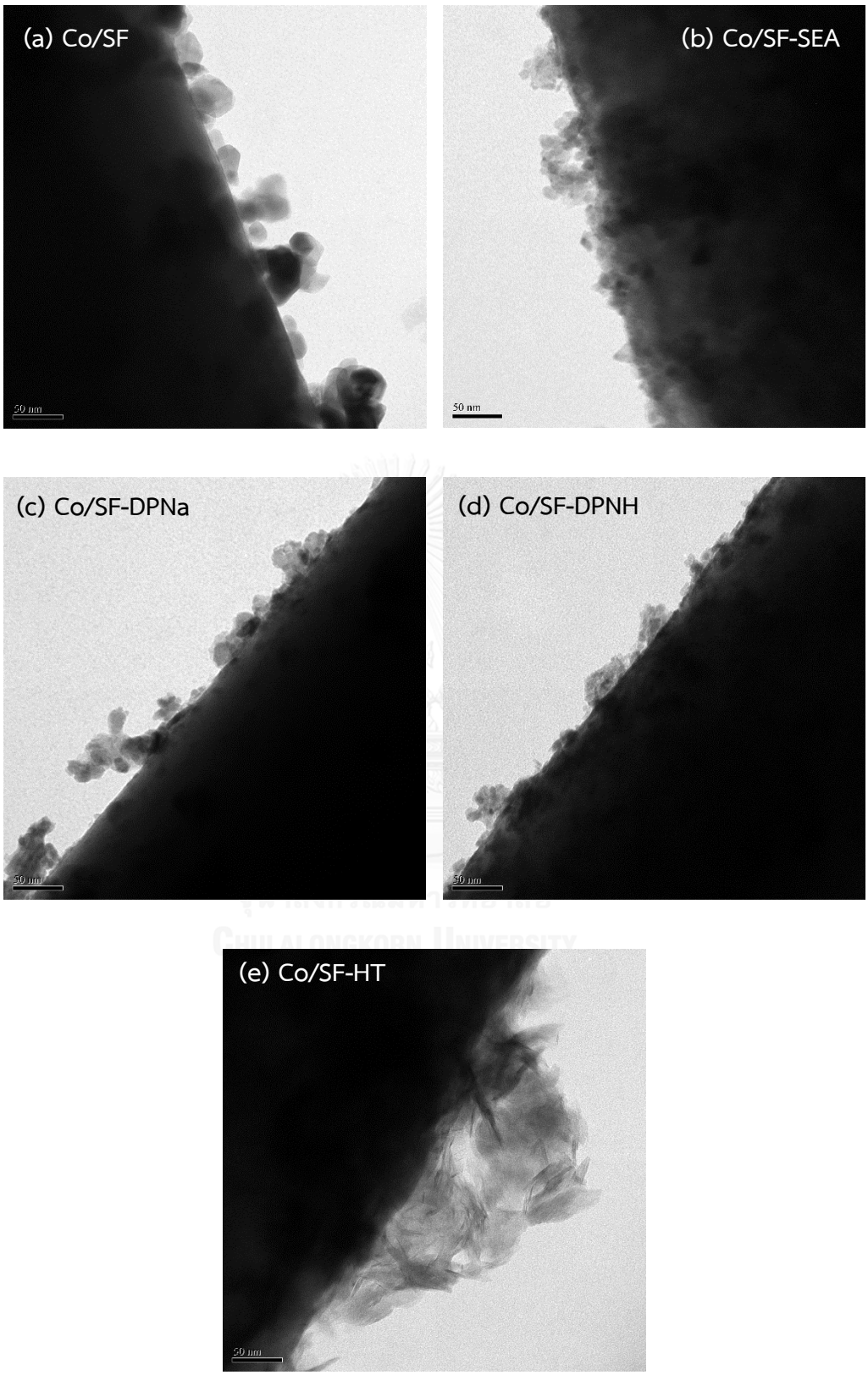

Figure 40 TEM images of the Co/SF catalysts prepared by different methods

4.6 The activity and selectivity of Co-based catalysts

Table 14 FTS reaction performance of the composite cobalt catalysts

Catalysts	CO Conv. (%)	CO_2 selectivity (%)	Hydrocarbon distribution (C mol%)				C_{ole}/C_n [a]	C_{iso}/C_n [b]
			C_1	C_2-C_4	C_5-C_{11}	C_{12}+		
Co/SF	21.9	0.0	13.3	13.2	47.6	25.9	0.19	0.10
Co/SiO_2	91.5	9.0	10.4	7.7	50.2	31.7	0.10	0.16
Co/ZSM-5-com	72.0	1.3	20.3	15.8	58.8	5.1	0.10	1.58
Co/ZSM-5	87.5	3.5	6.7	5.7	62.8	24.8	0.49	0.40
Co/ZSM-5/SF-4	82.6	4.6	10.2	9.4	61.9	18.5	0.45	0.36
Co/ZSM-5/SF-5	88.2	4.2	9.8	9.5	62.1	18.5	0.36	0.26
Co/ZSM-5/SF-6	85.7	3.1	8.7	7.5	66.9	16.9	0.34	0.47
Co/ZSM-5/SF-10	36.6	0.0	16.4	14.4	67.8	1.4	1.55	2.09
Co/ZSM-5/SF-11	89.5	5.0	9.2	7.2	62.5	21.0	0.48	0.40
ZSM-5/Co/SF	44.2	0.6	15.3	10.4	53.7	20.5	0.28	1.28
Co/SF+ZSM-5	24.9	0.0	17.6	11.1	62.0	9.3	0.44	2.12

Reaction conditions: 240 °C, 1.0 MPa, $H_2/CO=2$, time=6 h, W/F=10 g_{cat}·h mol^{-1}

[a] Olefin to n-paraffin ratio with a chain length of 2+

[b] Iso-paraffin to n-paraffin ratio with a chain length of 4+

The catalytic performance of Co-base catalysts was measured at 240°C, 1.0 MPa, 10 g_{cat}·h/mol and H_2/CO = 2. The activity of the catalysts was tested for over 6 h. The catalytic activities, in terms of the CO conversion level and product distribution, are summarized in Table 14. The Co/SF catalyst showed the lowest CO conversion level (21.9%) of all the catalysts. The low surface area of the SF and large particle size of the Co_3O_4 contributed to the low FTS activity. The ZSM-5 modified SF supported Co catalysts all exhibited a higher catalytic activity than that of the Co/SF catalyst with a CO conversion level of more than 80% for all Co/ZSM-5/SF catalysts, except for Co/ZSM-5/SF-10 catalyst. The larger net surface area was responsible for the formation of smaller Co particles on the ZSM-5/SF support, as also seen in the XRD analysis (Table 7; Figure 31).

Figure 41 shows the variation in conversion with time on stream (TOS), activity being expressed in terms of percentage conversion of CO. The CO conversion shows more than 82.6% for all Co supported on ZSM-5 and ZSM-5/SF catalysts. The catalytic activities on the Co/ZSM-5/SF catalyst were stable after 4.5 h of time on stream with

respected to CO conversion implying no cobalt oxidation. Generally, small Co particles (e.g., < 6 nm) are more easily oxidized by water [6, 15]. Azzam et al. [110] reported that ultra-small Co clusters (e.g., 1 nm) supported on KL-zeolite were oxidized in a significant fraction of the Co after exposure to realistic FTS conditions. On the other hand, medium Co clusters (~6 nm) was in a metallic state under realistic FTS conditions and found on cobalt oxide. It is expected that Co/ZSM-5/SF catalysts with larger Co particles (>10 nm) should be more resistant to oxidize by water at higher CO conversion levels.

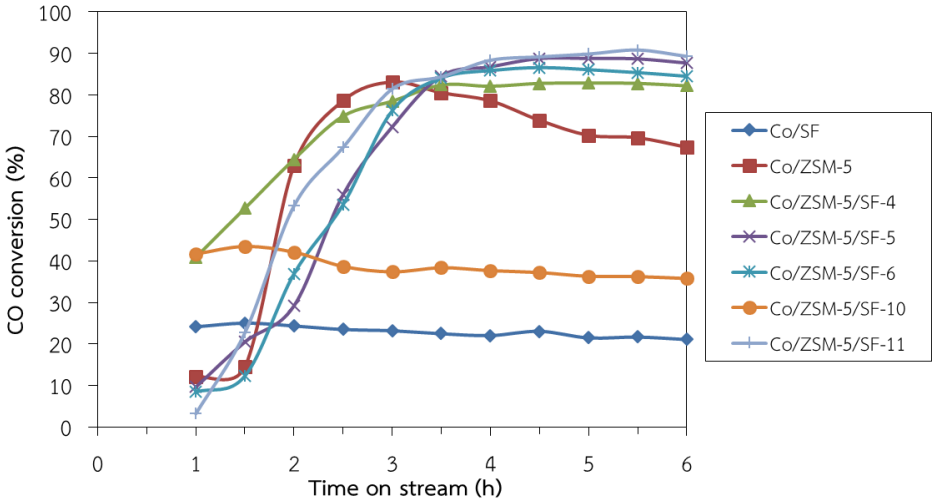

Figure 41 CO conversion of Co/ZSM-5/SF catalysts

The Co/SiO_2 catalysts showed higher conversion levels (91.5%), yields of C_{12+} products, and CO_2 selectivity than the Co/ZSM-5/SF catalysts. SiO_2 is a neutral oxide and there are no strong Brønsted or Lewis acid–base sites on the surface. Normally, hydroxyl layer of pretreatment silica is covered with physically adsorbed water. Under FTS condition, Co/SiO_2 catalysts yielded more water due to highest CO conversion and water then could be adsorbed on the surface of SiO_2 resulting in the increasing activity of WGS reaction. Meanwhile, the catalysts supported by ZSM-5/SF yielded low CO_2 because water molecules, as Lewis base centers, adsorbed on Lewis acid centers of HZSM-5 and suppressed WGS reaction activity [111]. Furthermore, the Co/ZSM-5/SF catalysts showed low values for methane selectivity due to their large average crystallite size of cobalt oxide (~10 nm). It is known that the methane selectivity is depended on the Co particles and pore size of the catalyst. The large Co particles (10-35 nm) give lower methane selectivity than 10% [1, 3]. Bezemer and co-workers [6]

observed that cobalt catalysts with sizes smaller than 5 nm showed high methane selectivity occurred by their low chain growth probabilities.

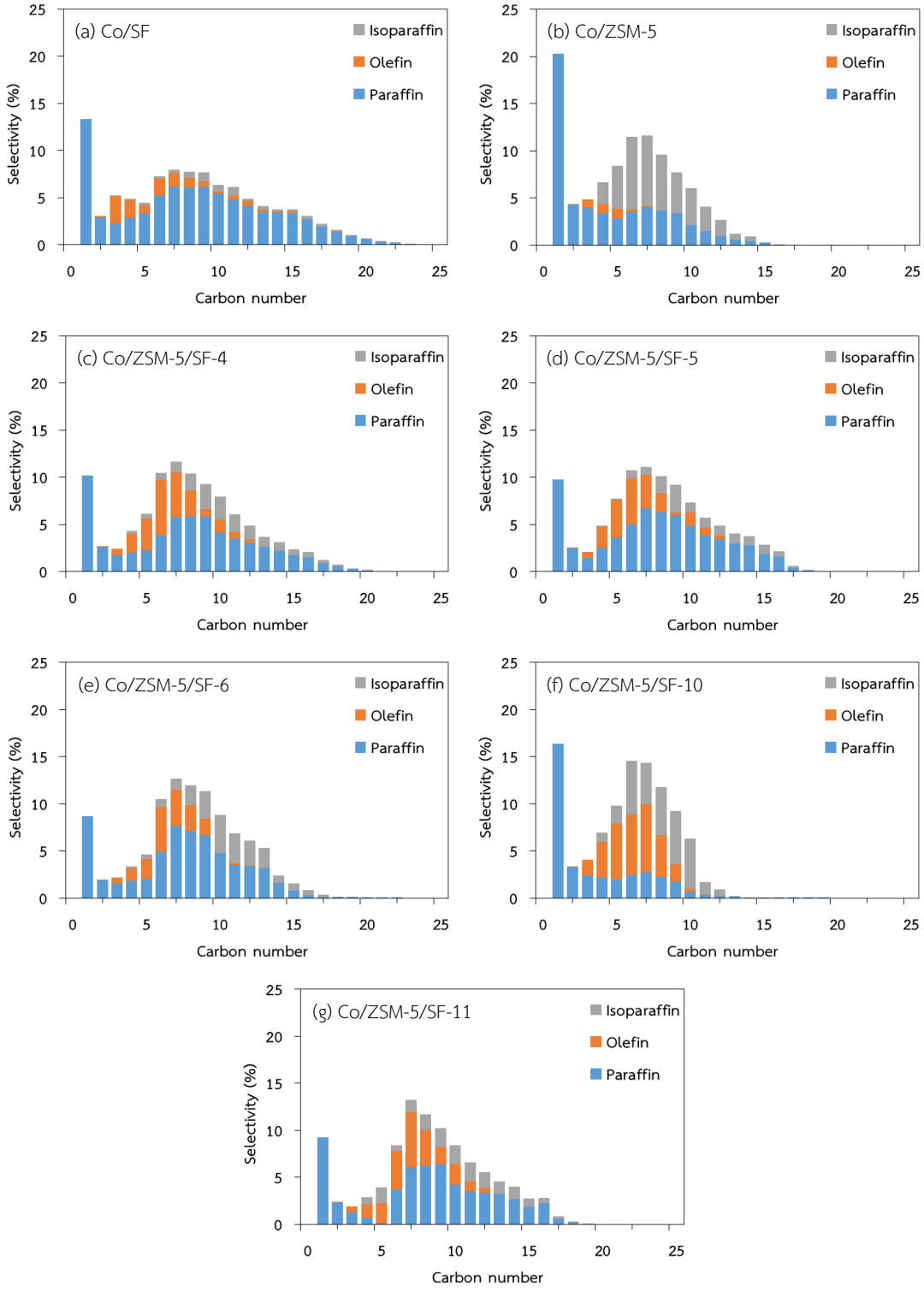

Figure 42 Product distribution over Co/ZSM-5/SF catalysts

A CO conversion of 36.6% was obtained over Co/ZSM-5/SF-10 catalyst with 0% selectivity to CO_2. Co/ZSM-5/SF-10 catalyst shows lower conversion level than that of other Co/ZSM-5/SF catalysts due to the lowest surface area of support. The fraction of CH_4, C_2-C_4 and C_5-C_{11} in hydrocarbon was 16.4, 14.4 and 67.8%, respectively. This catalyst gave a high ratio of olefins and isoparaffin. The use of ZSM-5/SF-10, which presents the largest pore volume with broad pore size distribution and a weaker acidity provided the lowest fraction of n-paraffins. In contrast, ZSM-5/SF-4, 5, 6 and 11 produced heavier products containing more n-paraffins. The chain growth occurred on Co particles, and the resultant primary hydrocarbons then underwent secondary reactions at the accessible zeolite acid sites to produce lighter products with more iso-paraffins. Since most of the Co particles may not be located inside the small zeolite channels, the accessible acid sites mainly include the external acid sites and the internal acid sites close to the pore mouths of the zeolite. The degree of secondary restructuring was the greatest over ZSM-5/SF-10-supported catalyst, indicating that the accessibility of primary FTS products to the internal acid sites is an important factor.

A large proportion of microporosity was present on convectional Co/ZSM-5 catalyst, the diffusion rate of reactants and products became slower in the pores, which resulted in the decrease of the probability of re-adsorption of the reaction intermediates such as one-olefins to form higher hydrocarbons. Especially, a certain amount of acid sites made it possible for the acid catalyzed reaction, such as cracking reaction. Moreover, the slow transportation of products inside the long micropores of zeolites usually caused over-cracking, leading to high selectivity to light hydrocarbons. The large amount of mesoporosity created in intraparticles was beneficial to the diffusion of the reactants and products, especially for the bulky molecules, and thereby improved the accessibility to the acid sites and hindered the over-cracking. Thus, the C_{12+} hydrocarbons over Co/ZSM-5/SF catalysts were higher than that over Co/ZSM-5. However, Co/ZSM-5 catalyst and Co/ ZSM-5/SF catalyst showed the main compound of C_5-C_{11}, as shown in Figure 42.

Co/ZSM-5/SF catalysts showed a low CO_2 selectivity (lower than 5%) with high selectivity toward C_5–C_{11} hydrocarbons product. The enhancement of C_5–C_{11} product selectivity on the Co/ZSM-5/SF catalysts is due to the acid sites on the zeolite support [41, 112]. The ratio of isoparaffins and olefins to normal paraffins were higher in the ZSM-5 modified SF catalysts than in the Co/SF catalyst (Table 14). It is known that the high olefins to normal paraffins is normally observed in zeolite-containing hybrid and core-shell cobalt catalysts [42, 47, 49] due to the hydrogen used in in-situ hydrocracking step is not enough to hydrogenate all olefins to paraffin [42].

FTS performances in term of CO conversion with time on stream over composite catalysts are presented in Figure 43. The Co/SF catalyst showed the lowest CO conversion level (21.9%) among all the catalysts, due to its low surface area and large Co_3O_4 particle size. The physically mixed ZSM-5 with Co/SF catalyst (Co/SF+ZSM-5) gave a relatively similar (1.14-fold higher) CO conversion level as that with the Co/SF catalyst (Table 14), whilst the ZSM-5 zeolite alone did not show any activity for the FTS reaction under this condition. The addition of ZSM-5 to Co/SF by physical mixing did not significantly change the CO_2 and CH_4 selectivity. However, the formation of hydrocarbons boiling above the gasoline range (C_{12+}) was suppressed about 2.8- and 2.2-fold in the Co/SF+ZSM-5 catalyst compared to that with the Co/SF and ZSM/Co/SF catalysts, respectively, while the selectivity for gasoline range products (C_5–C_{11}) was significantly increased by 1.3- and 1.2-fold, respectively.

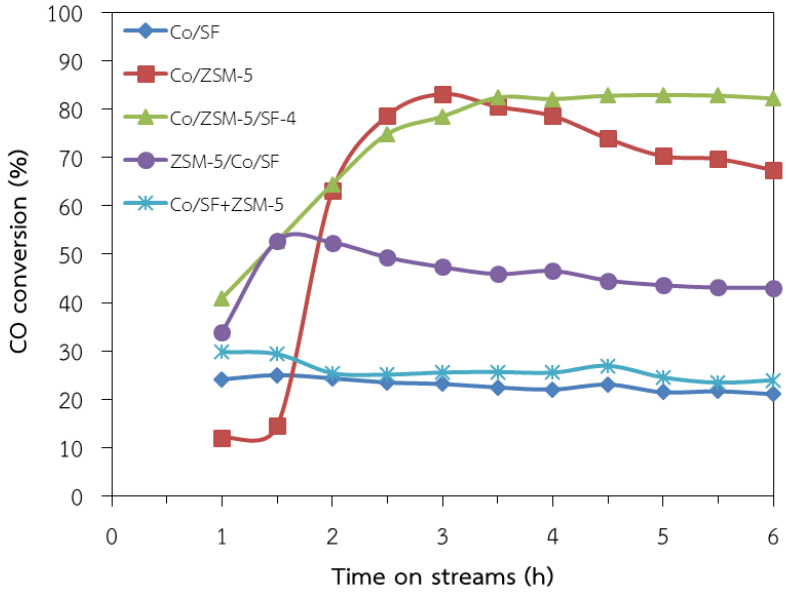

Figure 43 CO conversion of composite Co-base catalysts

The ZSM-5/Co/SF catalyst showed a higher CO conversion value than that of the Co/SF and the Co/SF+ZSM-5 catalysts. This could be attributed to the cracking of the waxy hydrocarbons on the zeolite acid sites, which would otherwise would accumulate on the surface of the FTS catalyst and reduce the number of active sites accessible to the syngas reactant [43]. Furthermore, the ZSM-5/Co/SF catalyst had a slightly higher CH_4 selectivity than the Co/SF and Co/SF+ZSM-5 catalysts, which is attributed to the higher ratio H_2/CO ratio in the core part of the catalyst. The different H_2/CO ratio results from the dissimilar molecular diffusivity values of these two gases

through the zeolite layer and so they would pass through the zeolite shell at different diffusion rates [15] giving a different final partial pressure of H_2 and CO in the core part of the catalyst compared to the outside.

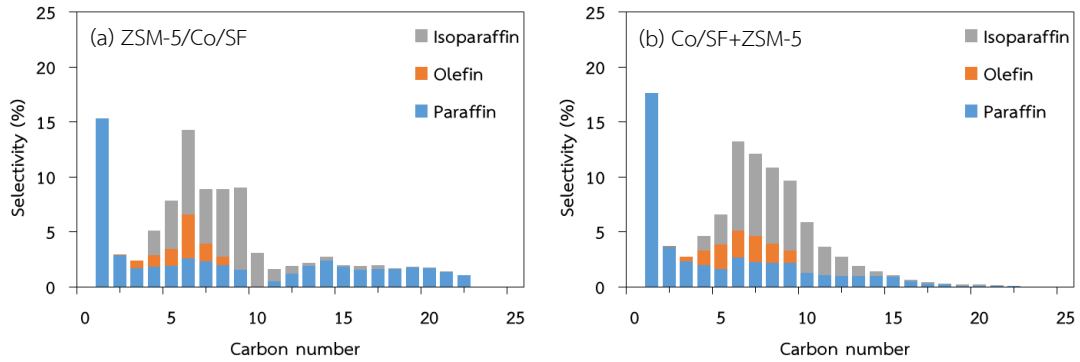

Figure 44 Product distribution over composite catalysts

Figure 44 shows product distribution of FTS reaction over ZSM-5/Co/SF and Co/SF+ZSM-5 catalysts. The ratios of isoparaffin to normal paraffin with the Co/ZSM-5 and Co/ZSM-5/SF catalysts were lower (3.2- to 5.9-fold) than those with the ZSM-5/Co/SF and Co/SF+ZSM-5 catalysts. This reflects that the interaction of the metal particles with the acid zeolite is accompanied by a proton transfer from the Brønsted acid site to the surface of the metal cluster [42], resulting in a decreased number of active sites in the zeolite and the suppression of the cracking and isomerization reactions.

Table 15 FTS performance of the different silica-supported cobalt catalysts

Catalysts	CO conv. (%)	CO_2 selectivity (%)	Hydrocarbon distribution (C mol%)				C_{ole}/C_n [a]	C_{iso}/C_n [b]
			C_1	C_2-C_4	C_5-C_{11}	C_{12+}		
Co/SF	21.9	0.0	13.3	13.2	47.6	25.9	0.19	0.10
Co/SF-SEA	80.4	4.2	8.0	6.9	62.6	22.5	0.17	0.15
Co/SF-DPNa	64.2	1.4	11.0	8.1	55.5	25.4	0.13	0.19
Co/SF-DPNH	65.9	1.6	11.3	8.3	56.6	23.8	0.11	0.10
Co/SF-HT	7.6	0.0	25.5	15.0	56.6	2.9	0.70	0.35

Reaction conditions: 240 °C, 1.0 MPa, H_2/CO=2, time=6 h, W/F=10 g_{cat}·h mol^{-1}

[a] olefin to n-paraffin ratio with chain length 2+

[b] iso-paraffin to n-paraffin ratio with chain length 4+

Table 15 showed FTS reaction performance of the different silica-supported cobalt catalysts. It can be seen that the activity and the selectivity of the catalysts was strongly affected by catalyst preparation method. It has been suggested that the cobalt catalyst activity for FTS was affected by cobalt particle size and reducibility [43, 47, 72]. The CO conversion and product selectivity of catalysts are presented in Table 15. The DPNH technique increased the %CO conversion (from 23.4 to 65.9%) and CH_4 selectivity (from 5.8 to 11.3%), compared to incipient wetness impregnation. Bezemer et al. [113] reported Co/CNF catalysts by a homogeneous deposition–precipitation method with urea decomposition to produce higher CO conversion and higher C_{5+} selectivity in FTS. Thus, improvement of the uniformity of the metal particles on the support leaded to enhancement CO conversion and the FTS selectivity. The Co/SF-DPNa and Co/SF-DPNH catalyst presented very similar in the CO conversion, as shown in Table 15, indicating that the precipitant in catalyst preparation did not promote the active site of Co catalyst. The Co/SF-HT was much less active (CO conversion of 7.6%) than the others. Such a low catalytic activity can be related to the low reducibility of cobalt species in the catalysts, probably in the form of cobalt silicates as discussed before.

The CH_4 selectivity was decreased with increasing cobalt particle size. Comparison between Co/SF and Co/SF-HT catalysts, the Co/SF-HT catalyst provided higher selectivity to methane because for the smaller the cobalt particle size, the stronger the CH_x species (representing carbon intermediates leading to methane) are bonded to the cobalt surface [107]. The lower CH_4 selectivity for the cobalt supported catalyst could be due to the effective participation of olefins in the carbon-carbon chain propagation. Thus, Co/SF catalyst, α-olefins can be re-adsorbed on the catalyst surface and undergo further chain initiation to produce larger hydrocarbons, hydrogenation to produce n-paraffins, or dehydrogenation to produce olefins [15, 107]. From Table 15, Co/SF-DPNa displayed a high C_{12+} selectivity. The difference in selectivity to C_{12+} was obtained by the effect of the cobalt particle size. The larger cobalt particles are more selective for higher molecular weight hydrocarbons in FTS because dissociative adsorption of CO, which leads to the formation of the $–CH_2–$ fragments required for chain growth [4]. Although the cobalt particle size in Co/SF is the largest of the four catalysts, it still presented the lowest activity. It is known that

the catalytic activity could affect the product selectivity of catalyst in FTS, with lower activity leading to lower C_{12+} hydrocarbon selectivity.

CHAPTER V
CONCLUSIONS AND RECOMMENDATIONS

5.1 Conclusions

The silica fibers were successfully synthesized by electrospinning technique and the optimized condition was TCD 15 cm and applied voltage 15 kV to produce continuous and submicron fibers with a diameter of 0.83 μm. The deposition of ZSM-5 on SiO_2-fiber supports was performed by the *in situ* hydrothermal synthesis of ZSM-5 in a solution containing the silica fiber support. The ZSM-5 can deposit on the surface of the SiO_2-fiber and improve their total surface area. A maximum yield of C_5–C_{11} hydrocarbons in the FTS reaction was obtained with the Co/ZSM-5/SF catalysts, which were superior to the Co/SiO_2 and Co/SF catalysts. This is mainly attributed to the formation of the small crystallite size of cobalt oxide and the higher acid site density on the ZSM-5 modified SF support. The modification of SF with ZSM-5 particles during the hydrothermal synthesis enhanced the selectivity to C_5–C_{11} hydrocarbons and increased the product ratio of isoparaffins and olefins to normal paraffins.

The obtained composite catalyst presented a high CO conversion level and selectivity for isoparaffin production. The addition of ZSM-5 to Co/SF by physical mixing did not significantly change the CO_2 and CH_4 selectivity but suppressed C_{12+} hydrocarbons. The C_{iso}/C_n ratios of Co/ZSM-5 and Co/ZSM-5/SF catalysts were lower than those of ZSM-5/Co/SF and Co/SF+ZSM-5 catalysts because the metal particles interact with the acid zeolite resulting in a decreased number of active sites in the zeolite and the suppression of the cracking and isomerization reactions.

The Co/SF catalysts prepared by strong electrostatic adsorption (SEA) and deposition precipitation (DP) methods exhibit much higher catalytic activity than the impregnation of cobalt on silica fiber catalyst for FTS. The preparation method also gave seriously influences the catalytic activity in FTS. The Co/SF catalysts with average cobalt crystallite sizes of 4, 9, 12, 14 and 30 nm can be prepared on silica fiber surfaces. Catalysts with different particle size of Co_3O_4 showed different catalytic activity. The Co/SF catalyst prepared by SEA method (cobalt particle size of 9 nm) exhibits the

highest catalytic activity among the four Co/SF catalysts. The Co/SF with its non-porous support show high selectivity to C_{5+} hydrocarbons and low selectivity to CO_2. The Co/SF-SEA catalyst showed the highest CO_2 and lowest C_{12+} product selectivity due to its smaller cobalt particle size.

5.2 Recommendation

Catalyst deactivation is an important problem in cobalt based Fischer–Tropsch synthesis. There are several causes of catalyst deactivation include poisoning by sulphur and/or nitrogen, oxidation of the active metal, sintering, surface carbon formation, and surface reconstruction. Combined with the relatively high price of cobalt, improved stability of the catalyst will add competitiveness to the technology. The comparison of deactivation of the obtained cobalt supported on ZSM-5/SF catalysts as compared to commercial catalyst will be investigated in future work. Spent catalyst has to be characterized and compared with its activated counterpart. The proposed mechanisms of catalyst deactivation include poisoning, sintering, surface carbon formation, carbidization, cobalt re-oxidation, cobalt–support mixed compound formation, surface reconstruction and mechanical deactivation through attrition. Sintering is the main cause of deactivation and leads to a reduction of the active surface area. The size dependent mobility of the crystals on various supports contributes significantly to the sintering behaviour. The most common techniques for detecting sintering are X-ray diffraction (XRD), transmission electron microscopy (TEM) and H_2 chemisorption. Extended X-ray absorption fine structure (EXAFS) and anomalous small angle X-ray scattering (ASAXS) are gaining importance in crystallite size analysis as synchrotron based techniques with *in situ* capabilities are readily available.

REFERENCES

1. Khodakov, A.Y., W. Chu, and P. Fongarland, *Advances in the Development of Novel Cobalt Fischer–Tropsch Catalysts for Synthesis of Long-Chain Hydrocarbons and Clean Fuels.* Chemical Reviews, 2007. **107**(5): p. 1692-1744.
2. Trépanier, M., A.K. Dalai, and N. Abatzoglou, *Synthesis of CNT-supported cobalt nanoparticle catalysts using a microemulsion technique: Role of nanoparticle size on reducibility, activity and selectivity in Fischer–Tropsch reactions.* Applied Catalysis A: General, 2010. **374**(1–2): p. 79-86.
3. Zhang, Q., J. Kang, and Y. Wang, *Development of Novel Catalysts for Fischer–Tropsch Synthesis: Tuning the Product Selectivity.* ChemCatChem, 2010. **2**(9): p. 1030-1058.
4. Shi, L., et al., *The modification of SiO_2 by various organic groups and its influence on the properties of cobalt-based catalysts for Fischer–Tropsch synthesis.* Fuel Processing Technology, 2010. **91**(4): p. 394-398.
5. Song, D. and J. Li, *Effect of catalyst pore size on the catalytic performance of silica supported cobalt Fischer–Tropsch catalysts.* Journal of Molecular Catalysis A: Chemical, 2006. **247**(1–2): p. 206-212.
6. Bezemer, G.L., et al., *Cobalt Particle Size Effects in the Fischer–Tropsch Reaction Studied with Carbon Nanofiber Supported Catalysts.* Journal of the American Chemical Society, 2006. **128**(12): p. 3956-3964.
7. Tavasoli, A., et al., *Comparing the deactivation behaviour of Co/CNT and Co/γ-Al_2O_3 nano catalysts in Fischer-Tropsch synthesis.* Journal of Natural Gas Chemistry, 2012. **21**(5): p. 605-613.
8. Martínez, A.n., et al., *Fischer–Tropsch synthesis of hydrocarbons over mesoporous Co/SBA-15 catalysts: the influence of metal loading, cobalt precursor, and promoters.* Journal of Catalysis, 2003. **220**(2): p. 486-499.
9. Storsæter, S., et al., *Characterization of alumina-, silica-, and titania-supported cobalt Fischer–Tropsch catalysts.* Journal of Catalysis, 2005. **236**(1): p. 139-152.

10. Wood, D.A., C. Nwaoha, and B.F. Towler, *Gas-to-liquids (GTL): A review of an industry offering several routes for monetizing natural gas.* Journal of Natural Gas Science and Engineering, 2012. **9**(0): p. 196-208.
11. Mendes, D., et al., *The water-gas shift reaction: from conventional catalytic systems to Pd-based membrane reactors—a review.* Asia-Pacific Journal of Chemical Engineering, 2010. **5**(1): p. 111-137.
12. Rauch, R., J. Hrbek, and H. Hofbauer, *Biomass gasification for synthesis gas production and applications of the syngas.* Wiley Interdisciplinary Reviews: Energy and Environment, 2014. **3**(4): p. 343-362.
13. Deutschmann, O., et al., *Heterogeneous Catalysis and Solid Catalysts*, in *Ullmann's Encyclopedia of Industrial Chemistry*. 2000, Wiley-VCH Verlag GmbH & Co. KGaA.
14. Gnanamani, M.K., et al., *Fischer–Tropsch synthesis: Metal–support interfacial contact governs oxygenates selectivity over CeO_2 supported Pt–Co catalysts.* Applied Catalysis A: General, 2011. **393**(1–2): p. 17-23.
15. Borg, Ø., et al., *Fischer–Tropsch synthesis: Cobalt particle size and support effects on intrinsic activity and product distribution.* Journal of Catalysis, 2008. **259**(2): p. 161-164.
16. Huang, X. and C.B. Roberts, *Selective Fischer–Tropsch synthesis over an Al_2O_3 supported cobalt catalyst in supercritical hexane.* Fuel Processing Technology, 2003. **83**(1–3): p. 81-99.
17. Bragança, L.F.F.P.G., et al., *Bimetallic Co-Fe nanocrystals deposited on SBA-15 and HMS mesoporous silicas as catalysts for Fischer–Tropsch synthesis.* Applied Catalysis A: General, 2012. **423–424**(0): p. 146-153.
18. Shimura, K., et al., *Fischer–Tropsch synthesis over TiO_2 supported cobalt catalyst: Effect of TiO_2 crystal phase and metal ion loading.* Applied Catalysis A: General, 2013. **460–461**(0): p. 8-14.
19. Ming, H. and B.G. Baker, *Characterization of cobalt Fischer-Tropsch catalysts I. Unpromoted cobalt-silica gel catalysts.* Applied Catalysis A: General, 1995. **123**(1): p. 23-36.

20. Ernst, B., et al., *Preparation and characterization of Fischer–Tropsch active Co/SiO_2 catalysts.* Applied Catalysis A: General, 1999. **186**(1–2): p. 145-168.
21. Saib, A.M., M. Claeys, and E. van Steen, *Silica supported cobalt Fischer–Tropsch catalysts: effect of pore diameter of support.* Catalysis Today, 2002. **71**(3–4): p. 395-402.
22. Jacobs, G., et al., *Fischer–Tropsch synthesis: support, loading, and promoter effects on the reducibility of cobalt catalysts.* Applied Catalysis A: General, 2002. **233**(1–2): p. 263-281.
23. Bagheri, S., N. Muhd Julkapli, and S. Bee Abd Hamid, *Titanium Dioxide as a Catalyst Support in Heterogeneous Catalysis.* The Scientific World Journal, 2014. **2014**: p. 21.
24. Oh, J.-H., et al., *Slurry-Phase Fischer–Tropsch Synthesis Using Co/γ-Al_2O_3, Co/SiO_2 and Co/TiO_2: Effect of Support on Catalyst Aggregation.* Catalysis Letters, 2009. **130**(3-4): p. 403-409.
25. Enache, D.I., M. Roy-Auberger, and R. Revel, *Differences in the characteristics and catalytic properties of cobalt-based Fischer–Tropsch catalysts supported on zirconia and alumina.* Applied Catalysis A: General, 2004. **268**(1–2): p. 51-60.
26. Bae, J.W., et al., *Effect of support and cobalt precursors on the activity of Co/AlPO4 catalysts in Fischer–Tropsch synthesis.* Journal of Molecular Catalysis A: Chemical, 2009. **311**(1–2): p. 7-16.
27. Bae, J.W., et al., *Enhanced Fischer–Tropsch activity on Co/P–Al_2O_3 catalyst: Effect of phosphorous content.* Catalysis Communications, 2009. **10**(9): p. 1358-1362.
28. Csicsery, S.M., *Shape-selective catalysis in zeolites.* Zeolites, 1984. **4**(3): p. 202-213.
29. Seo, G., et al., *Skeletal isomerization of 1-butene over ferrierite and ZSM-5 zeolites: influence of zeolite acidity.* Catalysis Letters, 1996. **36**(3-4): p. 249-253.

30. Lew, C.M., N. Rajabbeigi, and M. Tsapatsis, *Tin-containing zeolite for the isomerization of cellulosic sugars.* Microporous and Mesoporous Materials, 2012. **153**(0): p. 55-58.

31. Huang, X., et al., *CoZr/H-ZSM-5 hybrid catalysts for synthesis of gasoline-range isoparaffins from syngas.* Applied Catalysis A: General, 2011. **408**(1–2): p. 38-46.

32. Tang, Q., et al., *Preparation of metallic cobalt inside NaY zeolite with high catalytic activity in Fischer–Tropsch synthesis.* Catalysis Communications, 2003. **4**(5): p. 253-258.

33. Martínez, A. and G. Prieto, *The Application of Zeolites and Periodic Mesoporous Silicas in the Catalytic Conversion of Synthesis Gas.* Topics in Catalysis, 2009. **52**(1-2): p. 75-90.

34. Guczi, L. and I. Kiricsi, *Zeolite supported mono- and bimetallic systems: structure and performance as CO hydrogenation catalysts.* Applied Catalysis A: General, 1999. **186**(1–2): p. 375-394.

35. Tang, Q., et al., *Characterizations of Cobalt Oxide Nanoparticles within Faujasite Zeolites and the Formation of Metallic Cobalt.* Chemistry of Materials, 2004. **16**(10): p. 1967-1976.

36. Ravishankar, R., M.M. Li, and A. Borgna, *Novel utilization of MCM-22 molecular sieves as supports of cobalt catalysts in the Fischer–Tropsch synthesis.* Catalysis Today, 2005. **106**(1–4): p. 149-153.

37. Udaya, V., S. Rao, and R.J. Gormley, *Bifunctional catalysis in syngas conversions.* Catalysis Today, 1990. **6**(3): p. 207-234.

38. Botes, F.G. and W. Böhringer, *The addition of HZSM-5 to the Fischer–Tropsch process for improved gasoline production.* Applied Catalysis A: General, 2004. **267**(1–2): p. 217-225.

39. Botes, F.G., *The effect of a higher operating temperature on the Fischer–Tropsch/HZSM-5 bifunctional process.* Applied Catalysis A: General, 2005. **284**(1–2): p. 21-29.

40. Kang, S.-H., et al., *ZSM-5 Supported Cobalt Catalyst for the Direct Production of Gasoline Range Hydrocarbons by Fischer–Tropsch Synthesis.* Catalysis Letters, 2011. **141**(10): p. 1464-1471.

41. Baranak, M., et al., *Low acidity ZSM-5 supported iron catalysts for Fischer–Tropsch synthesis.* Catalysis Today, 2013. **207**(0): p. 57-64.

42. Tsubaki, N., et al., *Three-component hybrid catalyst for direct synthesis of isoparaffin via modified Fischer–Tropsch synthesis.* Catalysis Communications, 2003. **4**(3): p. 108-111.

43. Martínez, A. and C. López, *The influence of ZSM-5 zeolite composition and crystal size on the in situ conversion of Fischer–Tropsch products over hybrid catalysts.* Applied Catalysis A: General, 2005. **294**(2): p. 251-259.

44. Yoneyama, Y., et al., *Direct synthesis of isoparaffin by modified Fischer–Tropsch synthesis using hybrid catalyst of iron catalyst and zeolite.* Catalysis Today, 2005. **104**(1): p. 37-40.

45. Martínez, A., et al., *A detailed study of the activity and deactivation of zeolites in hybrid Co/SiO_2-zeolite Fischer–Tropsch catalysts.* Journal of Catalysis, 2007. **249**(2): p. 162-173.

46. Martínez, A., et al., *Catalytic behavior of hybrid Co/SiO_2-(medium-pore) zeolite catalysts during the one-stage conversion of syngas to gasoline.* Applied Catalysis A: General, 2008. **346**(1–2): p. 117-125.

47. Yang, G., et al., *Preparation, characterization and reaction performance of H-ZSM-5/cobalt/silica capsule catalysts with different sizes for direct synthesis of isoparaffins.* Applied Catalysis A: General, 2007. **329**(0): p. 99-105.

48. Bao, J., et al., *A Core/Shell Catalyst Produces a Spatially Confined Effect and Shape Selectivity in a Consecutive Reaction.* Angewandte Chemie International Edition, 2008. **47**(2): p. 353-356.

49. Li, X., et al., *One-step synthesis of H–β zeolite-enwrapped Co/Al_2O_3 Fischer–Tropsch catalyst with high spatial selectivity.* Journal of Catalysis, 2009. **265**(1): p. 26-34.

50. He, J., et al., *Designing a Capsule Catalyst and Its Application for Direct Synthesis of Middle Isoparaffins.* Langmuir, 2005. **21**(5): p. 1699-1702.

51. He, J., et al., *Multiple-Functional Capsule Catalysts: A Tailor-Made Confined Reaction Environment for the Direct Synthesis of Middle Isoparaffins from Syngas.* Chemistry – A European Journal, 2006. **12**(32): p. 8296-8304.

52. Ling, C.K., N.A. Mohd Zabidi, and C. Mohan, *Synthesis of Cobalt Nanoparticles on Silica Support using Strong Electrostatic Adsorption Method.* Journal Defect and Diffusion Forum, 2011. **312-315**: p. 370-375.

53. Kababji, A.H., B. Joseph, and J.T. Wolan, *Silica-Supported Cobalt Catalysts for Fischer–Tropsch Synthesis: Effects of Calcination Temperature and Support Surface Area on Cobalt Silicate Formation.* Catalysis Letters, 2009. **130**(1-2): p. 72-78.

54. Kalakkad, D.S., et al., *Attrition of precipitated iron Fischer-Tropsch catalysts.* Applied Catalysis A: General, 1995. **133**(2): p. 335-350.

55. Kang, S.C., K.-W. Jun, and Y.-J. Lee, *Effects of the CO/CO_2 Ratio in Synthesis Gas on the Catalytic Behavior in Fischer–Tropsch Synthesis Using K/Fe–Cu–Al Catalysts.* Energy & Fuels, 2013. **27**(11): p. 6377-6387.

56. Burattin, P., M. Che, and C. Louis, *Characterization of the Ni(II) Phase Formed on Silica Upon Deposition–Precipitation.* The Journal of Physical Chemistry B, 1997. **101**(36): p. 7060-7074.

57. Ribeiro, R.U., et al., *Colloidal Co nanoparticles supported on SiO_2: Synthesis, characterization and catalytic properties for steam reforming of ethanol.* Applied Catalysis B: Environmental, 2009. **91**(3–4): p. 670-678.

58. Gual, A., et al., *Colloidal Ru, Co and Fe-nanoparticles. Synthesis and application as nanocatalysts in the Fischer–Tropsch process.* Catalysis Today, 2012. **183**(1): p. 154-171.

59. Santos, G.A., et al., *Sol–gel synthesis of silica–cobalt composites by employing Co_3O_4 colloidal dispersions.* Colloids and Surfaces A: Physicochemical and Engineering Aspects, 2012. **395**(0): p. 217-224.

60. Jiao, L. and J.R. Regalbuto, *The synthesis of highly dispersed noble and base metals on silica via strong electrostatic adsorption: I. Amorphous silica.* Journal of Catalysis, 2008. **260**(2): p. 329-341.

61. Kouachi, K., et al., *Preparation of silica-supported cobalt catalysts from water-in-oil microemulsion for selective hydrogenation of citral.* Journal of Molecular Catalysis A: Chemical, 2009. **308**(1–2): p. 142-149.

62. Tavasoli, A., et al., *Enhancement of ruthenium-promoted Co/CNTs nanocatalyst performance using microemulsion technique.* International Journal of Industrial Chemistry, 2014. **5**(1): p. 1-11.

63. Saib, A.M., et al., *Preparation and characterisation of spherical Co/SiO_2 model catalysts with well-defined nano-sized cobalt crystallites and a comparison of their stability against oxidation with water.* Journal of Catalysis, 2006. **239**(2): p. 326-339.

64. Khassin, A.A., et al., *Metal–support interactions in cobalt-aluminum co-precipitated catalysts: XPS and CO adsorption studies.* Journal of Molecular Catalysis A: Chemical, 2001. **175**(1–2): p. 189-204.

65. Khassin, A.A., et al., *Cobalt-containing catalysts supported by synthetic Zn- and Mg-stevensites and their performance in the Fischer–Tropsch synthesis.* Journal of Molecular Catalysis A: Chemical, 2001. **168**(1–2): p. 209-224.

66. Sun, S. and H. Zeng, *Size-Controlled Synthesis of Magnetite Nanoparticles.* Journal of the American Chemical Society, 2002. **124**(28): p. 8204-8205.

67. Puntes, V., K. Krishnan, and A.P. Alivisatos, *Synthesis of Colloidal Cobalt Nanoparticles with Controlled Size and Shapes.* Topics in Catalysis, 2002. **19**(2): p. 145-148.

68. Li, H. and S. Liao, *Organic colloid method to prepare ultrafine cobalt nanoparticles with the size of 2 nm.* Solid State Communications, 2008. **145**(3): p. 118-121.

69. D'Souza, L., et al., *Preparation of silica- and carbon-supported cobalt by electrostatic adsorption of Co(III) hexaammines.* Journal of Catalysis, 2007. **248**(2): p. 165-174.

70. Eastoe, J. and B. Warne, *Nanoparticle and polymer synthesis in microemulsions.* Current Opinion in Colloid & Interface Science, 1996. **1**(6): p. 800-805.

71. Liu, W., et al., *Hydrothermal microemulsion synthesis of cobalt nanorods and self-assembly into square-shaped nanostructures.* Journal of Crystal Growth, 2005. **284**(3–4): p. 446-452.

72. Sang, S., et al., *Difference of ZSM-5 zeolites synthesized with various templates.* Catalysis Today, 2004. **93–95**(0): p. 729-734.

73. Cundy, C.S. and P.A. Cox, *The hydrothermal synthesis of zeolites: Precursors, intermediates and reaction mechanism.* Microporous and Mesoporous Materials, 2005. **82**(1–2): p. 1-78.

74. Ghobarkar, H., O. Schäf, and P. Knauth, *Zeolite Synthesis by the High-Pressure Hydrothermal Method: Synthesis of Natural 6-Ring Zeolites with Different Void Systems.* Angewandte Chemie International Edition, 2001. **40**(20): p. 3831-3833.

75. Kumar, N., et al., *Effect of synthesis time and mode of stirring on physico-chemical and catalytic properties of ZSM-5 zeolite catalysts.* Applied Catalysis A: General, 2002. **235**(1–2): p. 113-123.

76. Iwasaki, A., et al., *Behavior of the (010) face of silicalite crystal.* Zeolites, 1996. **16**(1): p. 35-41.

77. Armaroli, T., et al., *Effects of crystal size and Si/Al ratio on the surface properties of H-ZSM-5 zeolites.* Applied Catalysis A: General, 2006. **306**(0): p. 78-84.

78. Huang, Z.-M., et al., *A review on polymer nanofibers by electrospinning and their applications in nanocomposites.* Composites Science and Technology, 2003. **63**(15): p. 2223-2253.

79. Ahmed, F.E., B.S. Lalia, and R. Hashaikeh, *A review on electrospinning for membrane fabrication: Challenges and applications.* Desalination, 2015. **356**(0): p. 15-30.

80. Doshi, J. and D.H. Reneker, *Electrospinning process and applications of electrospun fibers.* Journal of Electrostatics, 1995. **35**(2–3): p. 151-160.

81. Thompson, C.J., et al., *Effects of parameters on nanofiber diameter determined from electrospinning model.* Polymer, 2007. **48**(23): p. 6913-6922.

82. Cundy, C.S. and P.A. Cox, *The Hydrothermal Synthesis of Zeolites: History and Development from the Earliest Days to the Present Time.* Chemical Reviews, 2003. **103**(3): p. 663-702.

83. Bhardwaj, N. and S.C. Kundu, *Electrospinning: A fascinating fiber fabrication technique.* Biotechnology Advances, 2010. **28**(3): p. 325-347.

84. Yang, Q., et al., *Influence of solvents on the formation of ultrathin uniform poly(vinyl pyrrolidone) nanofibers with electrospinning.* Journal of Polymer Science Part B: Polymer Physics, 2004. **42**(20): p. 3721-3726.

85. Mit-uppatham, C., M. Nithitanakul, and P. Supaphol, *Ultrafine Electrospun Polyamide-6 Fibers: Effect of Solution Conditions on Morphology and Average Fiber Diameter.* Macromolecular Chemistry and Physics, 2004. **205**(17): p. 2327-2338.

86. Bognitzki, M., et al., *Nanostructured Fibers via Electrospinning.* Advanced Materials, 2001. **13**(1): p. 70-72.

87. Lee, K.H., et al., *Influence of a mixing solvent with tetrahydrofuran and N,N-dimethylformamide on electrospun poly(vinyl chloride) nonwoven mats.* Journal of Polymer Science Part B: Polymer Physics, 2002. **40**(19): p. 2259-2268.

88. Zong, X., et al., *Structure and process relationship of electrospun bioabsorbable nanofiber membranes.* Polymer, 2002. **43**(16): p. 4403-4412.

89. Jarusuwannapoom, T., et al., *Effect of solvents on electro-spinnability of polystyrene solutions and morphological appearance of resulting electrospun polystyrene fibers.* European Polymer Journal, 2005. **41**(3): p. 409-421.

90. Homayoni, H., S.A.H. Ravandi, and M. Valizadeh, *Electrospinning of chitosan nanofibers: Processing optimization.* Carbohydrate Polymers, 2009. **77**(3): p. 656-661.

91. Frenot, A. and I.S. Chronakis, *Polymer nanofibers assembled by electrospinning.* Current Opinion in Colloid & Interface Science, 2003. **8**(1): p. 64-75.

92. Mo, X.M., et al., *Electrospun P(LLA-CL) nanofiber: a biomimetic extracellular matrix for smooth muscle cell and endothelial cell proliferation.* Biomaterials, 2004. **25**(10): p. 1883-1890.

93. Deitzel, J.M., et al., *The effect of processing variables on the morphology of electrospun nanofibers and textiles.* Polymer, 2001. **42**(1): p. 261-272.

94. Megelski, S., et al., *Micro- and Nanostructured Surface Morphology on Electrospun Polymer Fibers.* Macromolecules, 2002. **35**(22): p. 8456-8466.

95. Shin, Y.M., et al., *Experimental characterization of electrospinning: the electrically forced jet and instabilities.* Polymer, 2001. **42**(25): p. 09955-09967.

96. Yuan, X., et al., *Morphology of ultrafine polysulfone fibers prepared by electrospinning.* Polymer International, 2004. **53**(11): p. 1704-1710.

97. Biber, E., et al., *Effects of electrospinning process parameters on nanofibers obtained from Nylon 6 and poly (ethylene-n-butyl acrylate-maleic anhydride) elastomer blends using Johnson SB statistical distribution function.* Applied Physics A, 2010. **99**(2): p. 477-487.

98. Ki, C.S., et al., *Characterization of gelatin nanofiber prepared from gelatin–formic acid solution.* Polymer, 2005. **46**(14): p. 5094-5102.

99. Zuo, W., et al., *Experimental study on relationship between jet instability and formation of beaded fibers during electrospinning.* Polymer Engineering & Science, 2005. **45**(5): p. 704-709.

100. Lee, J.S., et al., *Role of molecular weight of atactic poly(vinyl alcohol) (PVA) in the structure and properties of PVA nanofabric prepared by electrospinning.* Journal of Applied Polymer Science, 2004. **93**(4): p. 1638-1646.

101. Cheng, S., et al., *Preparation of nonwoven polyimide/silica hybrid nanofiberous fabrics by combining electrospinning and controlled in situ sol–gel techniques.* European Polymer Journal, 2009. **45**(10): p. 2767-2778.

102. Lee, S.W., et al., *Preparation of SiO_2/TiO_2 composite fibers by sol–gel reaction and electrospinning.* Materials Letters, 2007. **61**(3): p. 889-893.

103. Zhu, Z., et al., *Highly Active and Stable Co_3O_4/ZSM-5 Catalyst for Propane Oxidation: Effect of the Preparation Method.* ACS Catalysis, 2013. **3**(6): p. 1154-1164.

104. Tavasoli, A., et al., *Cobalt supported on carbon nanotubes — A promising novel Fischer–Tropsch synthesis catalyst.* Fuel Processing Technology, 2008. **89**(5): p. 491-498.

105. Shi, L., et al., *Studies on surface impregnation combustion method to prepare supported Co/SiO_2 catalysts and its application for Fischer–Tropsch synthesis.* Applied Catalysis A: General, 2012. **435–436**(0): p. 217-224.

106. Mondal, P., C. Balomajumder, and B. Mohanty, *A laboratory study for the treatment of arsenic, iron, and manganese bearing ground water using Fe^{3+} impregnated activated carbon: Effects of shaking time, pH and temperature.* Journal of Hazardous Materials, 2007. **144**(1–2): p. 420-426.

107. Prieto, G., et al., *Cobalt particle size effects in Fischer–Tropsch synthesis: structural and in situ spectroscopic characterisation on reverse micelle-synthesised Co/ITQ-2 model catalysts.* Journal of Catalysis, 2009. **266**(1): p. 129-144.

108. Huber, G.W., et al., *Hydrothermal stability of Co/SiO_2 fischer-tropsch synthesis catalysts*, in *Studies in Surface Science and Catalysis*, G.W.R. J.J. Spivey and B.H. Davis, Editors. 2001, Elsevier. p. 423-430.

109. Kiss, G., et al., *Hydrothermal deactivation of silica-supported cobalt catalysts in Fischer–Tropsch synthesis.* Journal of Catalysis, 2003. **217**(1): p. 127-140.

110. Azzam, K., et al., *Effect of Cobalt Particle Size on the Catalyst Intrinsic Activity for Fischer–Tropsch Synthesis.* Catalysis Letters, 2014. **144**(3): p. 389-394.

111. Li, Y., et al., *Gasoline-Range Hydrocarbon Synthesis over Cobalt-Based Fischer–Tropsch Catalysts Supported on SiO_2/HZSM-5.* Energy & Fuels, 2008. **22**(3): p. 1897-1901.

112. Lin, Q., et al., *A Catalyst for One-step Isoparaffin Production via Fischer–Tropsch Synthesis: Growth of a H-Mordenite Shell Encapsulating a Fused Iron Core.* ChemCatChem, 2013. **5**(10): p. 3101-3106.

113. Bezemer, G.L., et al., *Preparation of Fischer–Tropsch cobalt catalysts supported on carbon nanofibers and silica using homogeneous deposition-precipitation.* Journal of Catalysis, 2006. **237**(2): p. 291-302.

APPENDICES

Appendix A

Calculation

1. Calculation for preparation of SF samples

Molar ratio of TEOS/EtOH/H_2O/HCl = 1/2/2/0.01

	MW(g/mol)	Density(g/cm^3)
Silica (SiO_2)	60.09	2.20
EtOH	46.07	0.789
H_2O	18.00	1.00
HCl	36.46	1.18
TEOS (purity 95%)	208.33	0.933

TEOS 1 mol = silica 1 mol

Assume of silica 7.5 g

Therefore,

$$mole\ of\ TEOS = \frac{7.5}{60.09} = 0.1248\ g$$

$$weight\ of\ TEOS = \frac{0.1248 \times 208.33 \times 100}{95} = 27.4\ g$$

$$volume\ of\ TEOS = \frac{weight}{density} = \frac{27.4}{0.933} = 29.3\ ml$$

At TEOS = 0.1248 mol

Thus TEOS:EtOH:H_2O:HCl = 0.1248:0.2494:0.2494:1.2x10^{-3}

$$volume\ of\ reactant = \frac{mol \times MW}{density}$$

Therefore,

$$volume\ of\ EtOH = \frac{0.2494 \times 46.07}{0.789} = 14.56\ ml$$

$$volume\ of\ H_2O = \frac{0.2494 \times 18}{1} = 4.49\ ml$$

$$volume\ of\ HCl = \frac{1.2 \times 10^{-3} \times 36.46}{1.18} = 0.04\ ml$$

2. Calculation for preparation of ZSM-5/SF samples

Molar ratio of TEOS/TPAOH/EtOH/H_2O/HNO_3 = 1/0.24/5/40/0.038

Starting of TEOS = 0.0034 mol

$$mol\ of\ X = Molar\ ratio\ of\ X \times mol\ of\ TEOS$$

$$Amount\ of\ X = \frac{MW \times mol \times 100}{\%Purity}$$

$$Water\ in\ X = \frac{Amount\ of\ X \times (100 - \%Purity)}{100}$$

a) TEOS

Purity 95%, MW = 208.33 g/mol, Molecular formula = $SiC_8H_{20}O_4$ and density = 0.933 g/cm^3

$$Amount\ of\ TEOS = \frac{208.33 \times 0.034 \times 100}{95} = 0.7456\ g$$

$$Water\ in\ TEOS = \frac{0.7456 \times (100 - 95)}{100} = 0.1316\ g$$

b) TPAOH

10% A.R. Grade, MW = 203.36 g/mol and Molecular formula = $C_{12}H_{29}NO$

$$Mol\ of\ TPAOH = 0.0034 \times 0.24 = 0.000816\ mol$$

$$Amount\ of\ TPAOH = \frac{203.36 \times 0.000816 \times 100}{10} = 0.1659\ g$$

$$Water\ in\ TPAOH = \frac{0.1659 \times (100 - 10)}{100} = 1.4935\ g$$

c) EtOH

99.5 wt%, MW = 46.07 g/mol and Molecular formula = C_2H_5OH

$$Mol\ of\ EtOH = 0.0034 \times 5 = 0.7832\ mol$$

$$Amount\ of\ EtOH = \frac{46.07 \times 0.7832 \times 100}{99.5} = 0.7871\ g$$

$$Water\ in\ EtOH = \frac{0.7871 \times (100 - 99.5)}{100} = 0.003936\ g$$

d) Nitric Acid

69 wt% A.R. Grade, MW = 63 g/mol and Molecular formula = HNO_3

$$Mol\ of\ HNO_3 = 0.0034 \times 0.038 = 0.000129\ g$$

$$Amount\ of\ \ HNO_3 = \frac{0.000129 \times 100}{61} = 0.013344\ g$$

$$Water\ in\ \ HNO_3 = \frac{0.013344 \times (100 - 62)}{100} = 0.005204\ g$$

e) H_2O

MW = 18 g/mol and Molecular formula = H_2O

$$Mol\ of\ water = 0.0034 \times 40 = 0.136\ mol$$

$$Amount\ of\ water = \ 18 \times 0.136 = 2.448\ g$$

$$Water\ add = 2.448 - water\ in\ TEOS + TPAOH + EtOH + HNO_3$$

$$Water\ add = 2.448 - (0.1316 + 1.4935 + 0.003936 + 0.005204)$$

$$Water\ add = 0.91204\ g$$

3. Calculation for preparation of cobalt loading

Co (MW = 58.93 g/mol)

$Co(NO_3)_2 \cdot 6H_2O$ (MW = 291.31 g/mol)

10wt% Co/SiO_2: SiO_2 = 90 g and Co = 10 g

At, weight of support = 5 g

$$Co = \frac{10 \times 5}{90} = 0.5556\ g$$

Cobalt nitrate required:

$$Co(NO_3)_2 \cdot 6H_2O = \frac{0.5556 \times 291.31}{58.93} = 2.7463\ g$$

Volume of support = 1 ml/g

Support = 5 g, Volume of water = 5×1 = 5 g

Thus, volume of solution = 5.0 mL

4. FTS reaction

$$\%CO = \frac{\left(\frac{CO}{Ar}\right)_{inlet} - \left(\frac{CO}{Ar}\right)_{outlet}}{\left(\frac{CO}{Ar}\right)_{inlet}} \times 100$$

$$CO_2\ selectivity\ (\%) = \frac{moles\ of\ CO_2\ produced}{moles\ of\ inlet\ CO - moles\ of\ outlet\ CO} \times 100$$

$$CH_4\ selectivity\ (\%) = S_{CH_4}$$
$$= \frac{moles\ of\ CH_4\ produced}{moles\ of\ inlet\ CO - moles\ of\ outlet\ CO - moles\ of\ CO_2 produced} \times 100$$

$$C_x\ selectivity\ (\%, x = 2 - 11) = S_{C_x}$$
$$= \frac{moles\ of\ C_x\ produced}{moles\ of\ inlet\ CO - moles\ of\ outlet\ CO - moles\ of\ CO_2 produced} \times 100$$

$$S_{C_{12+}} = 100 - S_{CH_4} - \sum_{i=2}^{11} S_{C_x}$$

$$C_{ole}/C_n = \frac{moles\ of\ olefin\ produced}{moles\ of\ paraffin\ produced}$$

$$C_{iso}/C_n = \frac{moles\ of\ isoparaffin\ produced}{moles\ of\ paraffin\ produced}$$

Example,

Effluent gas composition

Time on stream(h)		1	2	3	4	5	6
Area	Ar	21479	36129	59682	72017	75485	72495
	CO	135117	136472	136506	137097	137527	137350
	CH_4	10320	24634	50715	67071	73523	74516
	CO_2	1563	4722	10287	67071	12941	12045

Syngas

Syngas	Composition (%)	TCD(Area)
Ar	4.1	12794
CO	32.5	136164
(CO/Ar)	7.9268293	10.642801

Standard gas

Standard gas	Composition (%)	TCD (Area)	FID (Area)
CO	5.03	23320	N/A
CH_4	4.96	18953.667	585436
CO_2	5.12	22478.333	N/A

At 5 h,

$$\%CO = \frac{\left(\frac{136164}{12794}\right) - \left(\frac{137527}{75485}\right)}{\left(\frac{136164}{12794}\right)} \times 100 = 82.9\%$$

$$CO_2\ selectivity\ (\%) = \frac{5.22 \times 10^{-4}}{2.69 \times 10^{-2}} \times 100 = 1.94\%$$

$$CH_4\ selectivity\ (\%) = S_{CH_4} = \frac{1.65 \times 10^{-3}}{(2.69 \times 10^{-2}) - (5.22 \times 10^{-4})} \times 100 = 10.2\%$$

$$C_2\ selectivity\ (\%) = S_{C_2} = \frac{4.38 \times 10^{-4}}{(2.69 \times 10^{-2}) - (5.22 \times 10^{-4})} \times 100 = 2.7\%$$

$$C_3\ selectivity\ (\%) = S_{C_3} = \frac{3.94 \times 10^{-4}}{(2.69 \times 10^{-2}) - (5.22 \times 10^{-4})} \times 100 = 2.4\%$$

$$C_4\ selectivity\ (\%) = S_{C_4} = \frac{6.07 \times 10^{-4}}{(2.69 \times 10^{-2}) - (5.22 \times 10^{-4})} \times 100 = 4.3\%$$

.
.
.

$$C_{11}\ selectivity\ (\%) = S_{C_2} = \frac{9.85 \times 10^{-4}}{(2.69 \times 10^{-2}) - (5.22 \times 10^{-4})} \times 100 = 6.1\%$$

$$C_{12+}\ selectivity\ (\%) = S_{C_{12+}} = 100 - 10.2 - 2.7 - 2.4 - 4.3 - \cdots - 6.1 = 18.5\%$$

Determination of CO conversion and gas product selectivity.

Catalyst name = Co/SF, Flow rate = 19.91 ml/min, T = 17 °C, P = 1015 hPa, Weight of catalyst = 0.503 g, W/F = 10 g·h/mol

Time (h)		1	1.5	2	2.5	3	3.5	4	4.5	5	5.5	6
Area	Ar	21562	21755	21603	21371	21082	20989	20872	21083	20579	20729	20636
	CO	134711	134340	134601	134668	133373	134023	134022	133602	133115	133740	134155
	CH4	6019	6217	6054	5974	6053	5886	6017	5729	5653	5688	5646
	CO2	0	0	0	0	0	0	0	0	0	0	0
CO conversion (%)		24.1	25.0	24.4	23.5	23.2	22.5	22.0	23.1	21.5	21.7	21.1
F (s/10ml)		38.5		38.1		38.5		38.2		37.5		33.5
Gas produced (mol/h)		0.0382		0.0386		0.0382		0.0385		0.0392		0.0439
CH_4 produced		0.0159	0.0164	0.0160	0.0158	0.0160	0.0156	0.0159	0.0152	0.0150	0.0150	0.0149
CO_2 produced		0	0	0	0	0	0	0	0	0	0	0
CH_4 C-mol (mol/g·h)		0.0012		0.0012		0.0012		0.0012		0.0012		0.0013
CO_2 C-mol (mol/g·h)		0		0		0		0		0		0
CO (mol/g·h)		0.0078	0.0081	0.0079	0.0076	0.0075	0.0073	0.0072	0.0075	0.0070	0.0070	0.0068
CH_4 sel (mol%)		15.3		15.4		16.0		16.9		16.6		18.9
CO_2 sel (mol%)		0		0		0		0		0		0
C_{2+} sel (mol%)		84.7		84.6		84.0		83.1		83.4		81.1

Determination of CO conversion and gas product selectivity

Catalyst name = Co/ZSM-5, Flow rate = 19.77 ml/min, T = 14 °C, P = 1018 hPa, Weight of catalyst = 0.506 g, W/F = 10 g·h/mol

Time (h)		1	1.5	2	2.5	3	3.5	4	4.5	5	5.5	6
Area	Ar	14289	14410	28921	43396	52189	48856	47063	41016	37492	37338	35127
	CO	135302	132778	115128	99844	94825	102447	108559	115369	119983	121900	123348
	CH_4	2392	3343	20342	40775	57931	57619	53776	50218	46185	43146	41852
	CO_2	0	0	2626	5768	7381	6380	4996	3785	2956	2549	2393
CO conversion (%)		12.1	14.5	63.1	78.6	83.1	80.5	78.6	73.9	70.3	69.7	67.4
F (s/10ml)		141.7		109.1		92.5		80.0		74.4		73.1
Gas produced (mol/h)		0.0108		0.0141		0.0166		0.0192		0.0207		0.0210
CH_4 produced		0.0063	0.0087	0.0532	0.1067	0.1516	0.1508	0.1407	0.1314	0.1209	0.1129	0.1095
CO_2 produced		0	0	0	0	0	0	0	0	0	0	0
CH_4 C-mol (mol/g•h)		0.0001		0.0015		0.0050		0.0053		0.0049		0.0045
CO_2 C-mol (mol/g•h)		0		0		0		0		0		0
CO (mol/g•h)		0.0039	0.0047	0.0205	0.0256	0.0270	0.0262	0.0255	0.0240	0.0228	0.0227	0.0219
CH_4 sel (mol%)		3.4		7.3		18.8		21.3		21.9		21.0
CO_2 sel (mol%)		0		1		2		2		1		1
C_{2+} sel (mol%)		96.6		92.7		80.8		78.4		77.9		78.8

Determination of CO conversion and gas product selectivity

Catalyst name = Co/ZSM-5/SF-4, Flow rate = 20.55 ml/min, T = 15 °C, P = 1008 hPa, Weight of catalyst = 0.519 g, W/F = 10 g·h/mol

Time (h)		1	1.5	2	2.5	3	3.5	4	4.5	5	5.5	6
Area	Ar	21479	27114	36129	51668	59682	72259	72017	75185	75485	74773	72495
	CO	135117	136429	136472	137942	136506	135412	137097	137337	137527	137070	137350
	CH_4	10320	15572	24634	41910	50715	61119	67071	72524	73523	75456	74516
	CO_2	1563	2730	4722	8519	10287	12103	67071	13161	12941	12420	12045
CO conversion (%)		40.9	52.7	64.5	74.9	78.5	82.4	82.1	82.8	82.9	82.8	82.2
F (s/10ml)		220.1		195.5		197.2		171.5		164.9		150.7
Gas produced (mol/h)		0.0069		0.0077		0.0077		0.0088		0.0092		0.0101
CH_4 produced		0.0270	0.0408	0.0645	0.1097	0.1327	0.1599	0.1755	0.1898	0.1924	0.1975	0.1950
CO_2 produced		0	0	0	0	0	0	0	0	0	0	0
CH_4 C-mol (mol/g•h)		0.0004		0.0010		0.0020		0.0030		0.0034		0.0038
CO_2 C-mol (mol/g•h)		0		0		0		0		0		0
CO (mol/g•h)		0.0133	0.0171	0.0210	0.0243	0.0255	0.0268	0.0267	0.0269	0.0269	0.0269	0.0267
CH_4 sel (mol%)		2.7		4.6		7.8		12.4		12.9		14.4
CO_2 sel (mol%)		0		1		1		10		2		2
C_{2+} sel (mol%)		97.3		95.3		92.1		86.3		86.8		85.3

Determination of CO conversion and gas product selectivity

Catalyst name = Co/ZSM-5/SF-5, Flow rate = 19.66 ml/min, T = 240 °C, P = 1020 hPa, Weight of catalyst = 0.506 g, W/F = 10 g·h/mol

Time (h)		1	1.5	2	2.5	3	3.5	4	4.5	5	5.5	6
Area	Ar	13517	15354	17245	26663	39707	64001	71564	82572	84844	87735	84061
	CO	131389	131266	131321	126248	118218	105697	101685	99862	102167	106511	110978
	CH_4	2065	4534	6973	12931	22680	39449	51863	68317	73901	78863	82042
	CO_2	0	1795	1438	4066	9074	17616	23241	28512	29587	29556	29239
CO conversion (%)		9.6	20.5	29.2	56.0	72.3	84.6	86.8	88.8	88.8	88.7	87.7
F (s/10ml)		282.7		194.9		183.6		178.0		150.2		154.5
Gas produced (mol/h)		0.0055		0.0079		0.0084		0.0087		0.0103		0.0100
CH_4 produced		0.0054	0.0119	0.0182	0.0338	0.0594	0.1032	0.1357	0.1788	0.1934	0.2064	0.2147
CO_2 produced		0	0	0	0	0	0	0	0	0	0	0
CH_4 C-mol (mol/g·h)		0.0001		0.0003		0.0010		0.0023		0.0039		0.0042
CO_2 C-mol (mol/g·h)		0		0		0		0		0		0
CO (mol/g·h)		0.0031	0.0067	0.0095	0.0182	0.0235	0.0275	0.0282	0.0288	0.0289	0.0288	0.0285
CH_4 sel (mol%)		1.9		3.0		4.3		8.5		14.3		15.6
CO_2 sel (mol%)		0		1		1		3		5		5
C_{2+} sel (mol%)		98.1		97.0		95.7		91.2		85.0		83.7

Determination of CO conversion and gas product selectivity

Catalyst name = Co/ZSM-5/SF-6, Flow rate = 19.33 ml/min, T = 240 °C, P = 1029 hPa, Weight of catalyst = 0.490 g, W/F = 10 g·h/mol

Time (h)		1	1.5	2	2.5	3	3.5	4	4.5	5	5.5	6
Area	Ar	13631	14388	19843	26429	47737	66910	73596	77383	76377	74493	72311
	CO	134488	135839	134864	131961	122365	114780	112052	111437	114548	117356	120597
	CH_4	1198	1631	5432	10855	29801	45220	57292	66449	70228	71117	71102
	CO_2	0	0	1219	3075	9487	14270	17276	18817	18735	18214	17291
CO conversion (%)		8.4	12.3	36.9	53.6	76.2	84.1	85.9	86.6	86.1	85.4	84.5
F (s/10ml)		366.6		202.2		170.6		155.3		144.8		137.0
Gas produced (mol/h)		0.0041		0.0075		0.0089		0.0098		0.0105		0.0111
CH_4 produced		0.0031	0.0043	0.0142	0.0284	0.0780	0.1183	0.1499	0.1739	0.1838	0.1861	0.1861
CO_2 produced		0	0	0	0	0	0	0	0	0	0	0
CH_4 C-mol (mol/g•h)		0.0000		0.0002		0.0014		0.0030		0.0039		0.0042
CO_2 C-mol (mol/g•h)		0		0		0		0		0		0
CO (mol/g•h)		0.0027	0.0040	0.0120	0.0174	0.0248	0.0273	0.0279	0.0282	0.0280	0.0277	0.0275
CH_4 sel (mol%)		1.0		1.8		5.8		11.1		14.6		15.9
CO_2 sel (mol%)		0		0		2		3		3		3
C_{2+} sel (mol%)		99.0		98.2		94.1		88.6		84.9		83.6

Determination of CO conversion and gas product selectivity

Catalyst name = Co/ZSM-5/SF-10, Flow rate = 19.23 ml/min, T = 240 °C, P = 1020 hPa, Weight of catalyst = 0.483 g, W/F = 10 g·h/mol

Time (h)		1	1.5	2	2.5	3	3.5	4	4.5	5	5.5	6
Area	Ar	21095	21736	21314	20168	19782	20176	19995	19846	19697	19276	19580
	CO	132440	132254	132833	133160	133384	133884	134206	134169	135090	132358	135430
	CH_4	12079	14371	13641	12512	11955	12260	12397	12274	11748	11484	11689
	CO_2	0	0	0	0	0	0	0	0	0	0	0
CO conversion (%)		41.7	43.5	42.1	38.7	37.4	38.4	37.7	37.2	36.3	36.2	35.8
F (s/10ml)		51.2		48.4		49.7		47.8		46.6		47.7
Gas produced (mol/h)		0.0294		0.0312		0.0304		0.0315		0.0323		0.0316
CH_4 produced		0.0316	0.0376	0.0357	0.0327	0.0313	0.0321	0.0324	0.0321	0.0307	0.0301	0.0306
CO_2 produced		0	0	0	0	0	0	0	0	0	0	0
CH_4 C-mol (mol/g·h)		0.0019		0.0023		0.0020		0.0021		0.0021		0.0020
CO_2 C-mol (mol/g·h)		0		0		0		0		0		0
CO (mol/g·h)		0.0136	0.0141	0.0137	0.0126	0.0122	0.0125	0.0122	0.0121	0.0118	0.0118	0.0116
CH_4 sel (mol%)		14.2		16.8		16.2		17.3		17.4		17.2
CO_2 sel (mol%)		0		0		0		0		0		0
C_{2+} sel (mol%)		85.8		83.2		83.8		82.7		82.6		82.8

Determination of CO conversion and gas product selectivity

Catalyst name = Co/ZSM-5/SF-11, Flow rate = 19.97 ml/min, T = 240 °C, P = 1008 hPa, Weight of catalyst = 0.504 g, W/F = 10 g·h/mol

Time (h)		1	1.5	2	2.5	3	3.5	4	4.5	5	5.5	6
Area	Ar	12913	15901	25398	34212	53455	61012	75742	79781	86425	95718	88507
	CO	134709	132443	127878	160231	106956	102736	95015	93028	94305	94529	101969
	CH_4	1043	3782	14739	17290	39476	46807	56406	64693	73396	74476	78846
	CO_2	0	1927	4738	6219	20140	13994	30456	34366	37425	36845	36279
CO conversion (%)		3.2	22.7	53.3	56.5	81.4	84.4	88.4	89.2	89.9	90.8	89.3
F (s/10ml)		298.5		220.6		187.6		177.2		157.9		162.8
Gas produced (mol/h)		0.0051		0.0069		0.0081		0.0086		0.0096		0.0093
CH_4 produced		0.0027	0.0099	0.0386	0.0452	0.1033	0.1225	0.1476	0.1693	0.1921	0.1949	0.2063
CO_2 produced		0	0	0	0	0	0	0	0	0	0	0
CH_4 C-mol (mol/g·h)		0.0000		0.0005		0.0017		0.0025		0.0037		0.0038
CO_2 C-mol (mol/g·h)		0		0		0		0		0		0
CO (mol/g·h)		0.0010	0.0074	0.0173	0.0184	0.0265	0.0274	0.0287	0.0290	0.0292	0.0295	0.0290
CH_4 sel (mol%)		2.7		3.1		6.4		9.1		13.3		13.9
CO_2 sel (mol%)		0		1		3		4		6		5
C_{2+} sel (mol%)		97.3		96.9		93.4		90.5		86.0		85.4

Determination of CO conversion and gas product selectivity

Catalyst name = ZSM-5/Co/SF, Flow rate = 18.23 ml/min, T = 240 °C, P = 1017 hPa, Weight of catalyst = 0.449 g, W/F = 10 g·h/mol

Time (h)		1	1.5	2	2.5	3	3.5	4	4.5	5	5.5	6
Area	Ar	18645	25648	25561	24230	23395	22820	23059	22373	22024	21375	21925
	CO	131736	129453	130017	131198	131702	131941	131762	132569	132826	130032	133397
	CH_4	8256	19233	20323	19268	18374	17572	17420	17204	16834	15911	16535
	CO_2	0	789	876	821	768	710	699	692	671	658	665
CO conversion (%)		33.9	52.8	52.4	49.4	47.3	45.9	46.6	44.6	43.6	43.1	43.1
F (s/10ml)		64.8		61.1		59.4		58.5		57.0		57.9
Gas produced (mol/h)		0.0228		0.0242		0.0249		0.0253		0.0259		0.0255
CH_4 produced		0.0216	0.0503	0.0532	0.0504	0.0481	0.0460	0.0456	0.0450	0.0441	0.0416	0.0433
CO_2 produced		0	0	0	0	0	0	0	0	0	0	0
CH_4 C-mol (mol/g•h)		0.0011		0.0029		0.0027		0.0026		0.0025		0.0025
CO_2 C-mol (mol/g•h)		0		0		0		0		0		0
CO (mol/g•h)		0.0110	0.0172	0.0170	0.0160	0.0154	0.0149	0.0151	0.0145	0.0142	0.0140	0.0140
CH_4 sel (mol%)		10.0		16.9		17.4		17.1		18.1		17.7
CO_2 sel (mol%)		0		1		1		1		1		1
C_{2+} sel (mol%)		90.0		83.0		82.5		82.8		81.8		82.2

Determination of CO conversion and gas product selectivity

Catalyst name = Co/SF+ZSM-5, Flow rate = 17.23 ml/min, T = 240 °C, P = 1020 hPa, Weight of catalyst = 0.427 g, W/F = 10 g·h/mol

Time (h)		1	1.5	2	2.5	3	3.5	4	4.5	5	5.5	6
Area	Ar	16858	16918	16233	16186	16207	16270	16376	16745	16306	16189	16294
	CO	127356	128596	130247	130404	129814	130146	131245	131643	132408	133329	133333
	CH_4	10311	10617	8505	8253	8383	8210	78815	7653	7549	7506	7355
	CO_2	0	0	0	0	0	0	0	0	0	0	0
CO conversion (%)		29.8	29.4	25.4	25.1	25.6	25.7	25.5	26.9	24.5	23.5	24.0
F (s/10ml)		46.7		46.4		46.2		46.0		44.9		44.1
Gas produced (mol/h)		0.0318		0.0320		0.0322		0.0323		0.0331		0.0337
CH_4 produced		0.0270	0.0278	0.0223	0.0216	0.0219	0.0215	0.2063	0.0200	0.0198	0.0196	0.0192
CO_2 produced		0	0	0	0	0	0	0	0	0	0	0
CH_4 C-mol (mol/g•h)		0.0020		0.0017		0.0017		0.0156		0.0015		0.0015
CO_2 C-mol (mol/g•h)		0		0		0		0		0		0
CO (mol/g•h)		0.0097	0.0095	0.0083	0.0082	0.0083	0.0083	0.0083	0.0088	0.0080	0.0076	0.0078
CH_4 sel (mol%)		20.8		20.2		19.9		188.1		19.2		19.5
CO_2 sel (mol%)		0		0		0		0		0		0
C_{2+} sel (mol%)		79.2		79.8		80.1		-88.1		80.8		80.5

Determination of CO conversion and gas product selectivity

Catalyst name = Co/SF-SEA, Flow rate = 20.59 ml/min, T = 240 °C, P = 1015 hPa, Weight of catalyst = 0.506 g, W/F = 10 g·h/mol

Time (h)		1	1.5	2	2.5	3	3.5	4	4.5	5	5.5	6
Area	Ar	16219	17936	26484	38903	55576	66122	77674	74341	72429	74044	65716
	CO	123623	129132	128280	122942	114497	109942	107574	110171	113080	115098	121359
	CH_4	2816	5531	14005	26785	44632	58464	67939	75471	77811	76455	75202
	CO_2	0	1146	4999	11400	19823	25116	27259	27969	26755	24271	21716
CO conversion (%)		29.2	33.1	55.0	70.6	80.9	84.5	87.1	86.2	85.5	85.6	82.8
F (s/10ml)		230.0		193.7		169.6		151.3		141.3		134.1
Gas produced (mol/h)		0.0064		0.0076		0.0087		0.0097		0.0104		0.0110
CH_4 produced		0.0074	0.0145	0.0366	0.0701	0.1168	0.1530	0.1778	0.1975	0.2036	0.2001	0.1968
CO_2 produced		0	0	0	0	0	0	0	0	0	0	0
CH_4 C-mol (mol/g·h)		0.0001		0.0006		0.0020		0.0034		0.0042		0.0043
CO_2 C-mol (mol/g·h)		0		0		0		0		0		0
CO (mol/g·h)		0.0095	0.0108	0.0179	0.0230	0.0263	0.0275	0.0283	0.0280	0.0278	0.0278	0.0269
CH_4 sel (mol%)		1.0		3.1		7.9		12.6		15.8		16.6
CO_2 sel (mol%)		0		1		3		4		5		4
C_{2+} sel (mol%)		99.0		96.9		91.9		86.8		83.4		82.8

Determination of CO conversion and gas product selectivity

Catalyst name = Co/SF-DPNa, Flow rate = 20.39 ml/min, T = 240 °C, P = 1025 hPa, Weight of catalyst = 0.504 g, W/F = 10 g·h/mol

Time (h)		1	1.5	2	2.5	3	3.5	4	4.5	5	5.5	6
Area	Ar	18064	26034	35683	37740	37333	36533	35112	34531	33693	34616	32470
	CO	137995	140241	140661	139821	139399	138443	136682	133767	130284	128305	127407
	CH_4	4328	11912	21825	24702	25670	25135	24676	24662	24475	24291	24130
	CO_2	1247	2015	3216	3477	3542	2397	3285	3284	3270	3263	3292
CO conversion (%)		29.0	49.9	63.4	65.6	65.3	64.8	63.8	64.0	64.1	65.6	63.5
F (s/10ml)		92.6		87.3		84.9		82.1		78.6		74.9
Gas produced (mol/h)		0.0160		0.0170		0.0175		0.0181		0.0189		0.0198
CH_4 produced		0.0113	0.0312	0.0571	0.0646	0.0672	0.0658	0.0646	0.0645	0.0640	0.0636	0.0631
CO_2 produced		0	0	0	0	0	0	0	0	0	0	0
CH_4 C-mol (mol/g•h)		0.0004		0.0019		0.0023		0.0023		0.0024		0.0025
CO_2 C-mol (mol/g•h)		0		0		0		0		0		0
CO (mol/g•h)		0.0094	0.0162	0.0206	0.0213	0.0212	0.0211	0.0207	0.0208	0.0208	0.0213	0.0206
CH_4 sel (mol%)		3.9		9.5		11.1		11.3		11.7		12.2
CO_2 sel (mol%)		1		1		1		1		1		1
C_{2+} sel (mol%)		96.1		90.4		88.7		88.5		88.2		87.6

Determination of CO conversion and gas product selectivity

Catalyst name = Co/SF-DPNH, Flow rate = 11.87 ml/min, T = 240 °C, P = 1022 hPa, Weight of catalyst = 0.303 g, W/F = 10 g·h/mol

Time (h)		1	1.5	2	2.5	3	3.5	4	4.5	5	5.5	6
Area	Ar	12617	15766	23468	31987	39175	39455	39527	37791	37356	36711	35095
	CO	111175	128884	134188	133906	133962	134345	134170	136087	136685	139072	137993
	CH_4	0	2192	13004	24586	36135	36782	35574	35059	35913	33788	32201
	CO_2	0	0	535	1212	1775	1717	1566	1493	1374	1356	1253
CO conversion (%)		18.2	24.1	46.9	61.1	68.2	68.4	68.5	66.6	66.0	64.8	63.5
F (s/10ml)		170.7		141.8		130.5		129.8		117.6		113.3
Gas produced (mol/h)		0.0090		0.0108		0.0117		0.0118		0.0130		0.0135
CH_4 produced		0.0000	0.0057	0.0340	0.0643	0.0946	0.0963	0.0931	0.0917	0.0940	0.0884	0.0843
CO_2 produced		0	0	0	0	0	0	0	0	0	0	0
CH_4 C-mol (mol/g·h)		0.0000		0.0012		0.0037		0.0036		0.0040		0.0038
CO_2 C-mol (mol/g·h)		0		0		0		0		0		0
CO (mol/g·h)		0.0059	0.0078	0.0152	0.0199	0.0222	0.0222	0.0223	0.0216	0.0215	0.0211	0.0206
CH_4 sel (mol%)		0.0		8.0		16.6		16.4		18.9		18.3
CO_2 sel (mol%)		0		0		1		1		1		1
C_{2+} sel (mol%)		100.0		92.0		83.3		83.5		80.9		81.6

Determination of CO conversion and gas product selectivity

Catalyst name = Co/SF-HT, Flow rate = 12.79 ml/min, T = 240 °C, P = 1018 hPa, Weight of catalyst = 0.325 g, W/F = 10 g·h/mol

Time (h)		1	1.5	2	2.5	3	3.5	4	4.5	5	5.5	6
Area	Ar	13989	13967	13931	13897	14158	13879	13875	14148	13850	13976	14376
	CO	134655	135120	135847	135989	135834	136066	136359	136118	136933	137132	136765
	CH_4	5560	5719	5501	5408	5323	5618	5215	5388	5097	5090	5234
	CO_2	0	0	0	0	0	0	0	0	0	0	0
CO conversion (%)		10.6	10.2	9.4	9.1	10.9	9.0	8.7	10.7	8.2	8.9	11.7
F (s/10ml)		47.0		47.2		46.4		46.4		45.6		46.0
Gas produced (mol/h)		0.0324		0.0323		0.0329		0.0329		0.0334		0.0332
CH_4 produced		0.0146	0.0150	0.0144	0.0142	0.0139	0.0147	0.0136	0.0141	0.0133	0.0133	0.0137
CO_2 produced		0	0	0	0	0	0	0	0	0	0	0
CH_4 C-mol (mol/g·h)		0.0015		0.0014		0.0014		0.0014		0.0014		0.0014
CO_2 C-mol (mol/g·h)		0		0		0		0		0		0
CO (mol/g·h)		0.0034	0.0033	0.0031	0.0030	0.0035	0.0029	0.0028	0.0035	0.0027	0.0029	0.0038
CH_4 sel (mol%)		42.1		46.6		39.8		48.6		51.6		36.9
CO_2 sel (mol%)		0		0		0		0		0		0
C_{2+} sel (mol%)		57.9		53.4		60.2		51.4		48.4		63.1

Appendix B

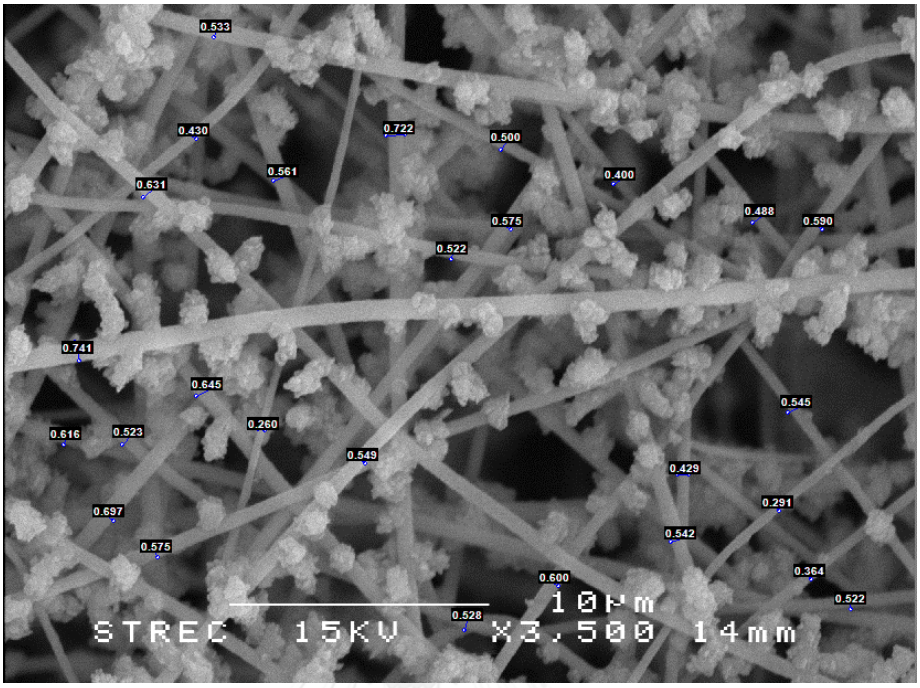

Figure B-1 Determination of fiber diameter by SemAfore program

VITA

Miss Kanthana Klaigaew was born on November 21, 1986 in Prachuabkhirikhan, Thailand. She graduated with Bachelor's degree of science, majoring in Chemistry, Faculty of Science, Thammasat University in 2008. Presence, she has been a graduate student in program of Chemical Technology, Faculty of Science, Chulalongkron University, Bangkok, Thailand since 2009 and finished her study in 2014.

Publication

K. Klaigaew, C. Samart, C. Chaiya, Y. Yoneyama, N. Tsubaki, P. Reubroycharoen, Effect of preparation methods on activation of cobalt catalyst supported on silica fiber for Fischer–Tropsch synthesis, Chemical Engineering Journal. (Published)

K. Klaigaew, P. Wattanapaphawong, N. Khuhaudomlap, N. Hinchiranan, P. Kuchontara, K. Kangwansaichol, P. Reubroycharoen, Liquid phase pyrolysis of Giant Leucaena wood to bio-oil over NiMo/Al2O3 catalyst, Energy Procedia. (Accepted)

Presentation Experience

Poster presentation: Cobalt catalyst supported on ZSM-5 beaded SiO2-fiber for Fischer-Tropsch synthesis 2014. 11th Intl Symposium - PREPA11, 6-10/7/2014, Louvain-la-Neuve, Belgium.

Poster presentation: Effect of preparation methods on activation of cobalt catalyst supported on silica fiber for Fischer-Tropsch synthesis 2014. ISCRE 23 and APCRE 7, 7-10/9/2014, Bangkok, Thailand.

Oral presentation: Fischer-Tropsch synthesis over cobalt catalyst supported on SiO2-fiber modification by ZSM-5 2014. The 4th Asian Conference on Innovative Energy and Environmental Chemical Engineering (ASCON-IEEChE), 9-12/11/2014, Yeosu, South Korea.